

## WAVES IN THE MAGNETIZED SOLAR ATMOSPHERE. II. WAVES FROM LOCALIZED SOURCES IN MAGNETIC FLUX CONCENTRATIONS

T. J. BOGDAN<sup>1</sup>

National Science Foundation, Arlington, VA 22203; and E. O. Hulbert Center for Space Research,  
 Naval Research Laboratory, 4555 Overlook Avenue, SW, Washington, DC 20375

M. CARLSSON V. HANSTEEN, A. McMURRY, AND C. S. ROSENTHAL<sup>2</sup>

Institute of Theoretical Astrophysics, University of Oslo, P.O. Box 1029, Blindern, Oslo, N-0315, Norway

M. JOHNSON, S. PETTY-POWELL, AND E. J. ZITA

Evergreen State College, Olympia, WA 98505

R. F. STEIN

Department of Physics and Astronomy, Michigan State University, East Lansing, MI 48824-1116

S. W. McINTOSH

Laboratory for Astronomy and Solar Physics, NASA Goddard Space Flight Center, Greenbelt, MD 20771;  
 and Universities Space Research Association, CPSS, Seabrook, MD 20770

AND

Å. NORDLUND

Niels Bohr Institute for Astronomy, Physics and Geophysics, Københavns Universitet, Blegdamsvej 17,  
 Copenhagen Ø, DK-2100, Denmark

*Received 2003 March 19; accepted 2003 July 16*

### ABSTRACT

Numerical simulations of wave propagation in a two-dimensional stratified magneto-atmosphere are presented for conditions that are representative of the solar photosphere and chromosphere. Both the emergent magnetic flux and the extent of the wave source are spatially localized at the lower photospheric boundary of the simulation. The calculations show that the coupling between the fast and slow magneto-acoustic-gravity (MAG) waves is confined to thin quasi-one-dimensional atmospheric layers where the sound speed and the Alfvén velocity are comparable in magnitude. Away from this wave conversion zone, which we call the magnetic canopy, the two MAG waves are effectively decoupled because either the magnetic pressure ( $B^2/8\pi$ ) or the plasma pressure ( $p = Nk_B T$ ) dominates over the other. The character of the fluctuations observed in the magneto-atmosphere depend sensitively on the relative location and orientation of the magnetic canopy with respect to the wave source and the observation point. Several distinct wave trains may converge on and simultaneously pass through a given location. Their coherent superposition presents a bewildering variety of Doppler and intensity time series because (1) some waves come directly from the source while others emerge from the magnetic canopy following mode conversion, (2) the propagation directions of the individual wave trains are neither co-aligned with each other nor with the observer's line of sight, and (3) the wave trains may be either fast or slow MAG waves that exhibit different characteristics depending on whether they are observed in high- $\beta$  or low- $\beta$  plasmas ( $\beta \equiv 8\pi p/B^2$ ). Through the analysis of four numerical experiments a coherent and physically intuitive picture emerges of how fast and slow MAG waves interact within two-dimensional magneto-atmospheres.

*Subject headings:* MHD — Sun: chromosphere — Sun: magnetic fields — Sun: oscillations — sunspots

### 1. INTRODUCTION

This is the second in a projected series of papers that explores the basic physics of wave propagation in stratified magneto-atmospheres. In the previous contribution (Rosenthal et al. 2002, hereafter Paper I) we outlined the basic equilibrium configurations and the underlying governing equations that form the basis for this series. We also took special care to define the nomenclature used to describe and identify the various types of waves present in the simulations and in realistic magneto-atmospheres. The essential point to emerge from these discussions is that it makes sense to speak of fast and slow magneto-

acoustic-gravity (MAG) waves within contiguous regions where the plasma  $\beta$ , the ratio of the thermal to the magnetic pressure, viz.,  $8\pi p/B^2$ , is everywhere much greater or much smaller than unity. However, it is not possible to continue such identifications across atmospheric layers where  $\beta \approx 1$ , because of the ubiquitous wave mixing and transformation that occur there. We shall continue the practice established in Paper I of simply referring to this mixing layer as the “magnetic canopy.”

The physical principles that underlie the linear mixing of fast and slow MAG waves have been known for some time (Ferraro & Plumpton 1958). Where the Alfvén velocity and the sound speed are disparate, the two waves are decoupled, with one having a dominant magnetic character, and the other being mostly acoustic in nature. However, when the Alfvén velocity and the sound speed are comparable, the waves become alike, which means that they show both

<sup>1</sup> On leave from the High Altitude Observatory of the National Center for Atmospheric Research through 2003 October 1.

<sup>2</sup> Current address: Soskraenten 58, DK-8260 Viby J, Denmark.

acoustic and magnetic qualities, and this is the cause of the mixing. The waves approach the canopy as separate entities; they become alike inside the canopy and emerge from it as separate waves again, with exchanged identities, i.e., transformed one into the other (Z. E. Musielak 2003, private communication). The essential finding of this investigation is simply that this fundamental concept of wave mixing and transformation remains valid in two-dimensional magnetic field geometries.

In this paper, we focus on the behavior of monochromatic waves emanating from spatially localized ( $\Delta x \approx H_p$ ) and temporally coherent (lifetime  $\gg$  period) sources. The salient property of such wave trains is the complex interference patterns that develop between the different wave types emitted directly by the source and those emerging following transformation at nearby  $\beta \approx 1$  magnetic canopy layers. Waves that arrive at a particular atmospheric location may have left the source region at different times and often take rather distinct routes in transit. This occurs largely on account of the great disparities between the sound speed [ $c \equiv (\gamma p / \rho)^{1/2}$ ] and the Alfvén velocity [ $a \equiv B / (4\pi\rho)^{1/2}$ ]. We select a single driving frequency that is about 10 times larger than the acoustic cutoff frequency of the magneto-atmosphere. Given the preliminary character of our direct numerical simulations of waves in two-dimensional equilibria, we believe there is little justification for treating a realistic stochastic driving process with a broad spectrum of frequencies. Instead, we simply regard the monochromatic driving studied here as being representative in a very qualitative sense of the high-frequency (say  $> 30$  mHz) tail of the solar turbulent spectrum.

The calculations presented and analyzed here also underscore the fundamental role played by the magnetic canopy in shaping the spatial and temporal distribution of oscillatory phenomena in and around magnetic flux concentrations. The critical importance of the magnetic canopy for wave propagation was a central theme of Paper I. It continues to remain so in the present contribution, although new facets of its influence and function will subsequently emerge in what follows.

These numerical simulations are crucial for developing a physical context in which to discuss and interpret waves and oscillations in gravitationally stratified highly conducting astrophysical plasmas. The specific examples studied here pertain to localized sources within magnetic flux concentrations. Parallels may readily be drawn to acoustic sources in the Sun's magnetic network and within isolated magnetic flux tubes, pores, knots, and sunspots. In fact, typical values adopted for the surface gravity, sound speed, and magnetic field strength are chosen to be commensurate with the prevailing solar surface conditions. Similar application to late-type stars and planetary magnetospheres are subject to additional caveats, but a general level of correspondence is essentially retained. We shall comment at length in the concluding section as to how these findings impact the interpretation of oscillation data from sunspots and the network.

On the other hand, no effort will be made to model particular observation sequences or to create synthetic Stokes profiles. Such exercises are premature and distract from the principal effort to fashion a basic physical foundation on which to build our understanding. It is our intent to address these practical and applied issues in forthcoming contributions. The later papers will eventually employ a sophisticated multidimensional radiative transfer calculation in lieu

of the condition of isentropy ( $DS/Dt = \partial S/\partial t + \mathbf{u} \cdot \nabla S = 0$ ). Direct comparisons with data will then be meaningful and informative.

The pressing need for such a basic study of wave propagation in magneto-atmospheres is justified on both observational and theoretical grounds. In the solar atmosphere, for example, the waves and oscillations that one can readily detect have a characteristic wavelengths comparable to the scale of variation of the magnetic field. This basic equality may well be a natural consequence of how the wave sources are influenced by the magnetic field. From a theoretical perspective this congruence of scales is unfortunate, since it renders ineffective several powerful techniques that have been developed to address situations in which the wavelength is much greater (i.e., virial methods and fine-grain averaging) or much smaller (i.e., eikonal and WKB methods) than the spatial scale of the background magnetic field (Barnes 1992; Webb et al. 1993; Čadež & Ballester 1994; Čadež, Oliver, & Ballester 1996; Ruderman, Nakariakov, & Roberts 1998). Under these unfavorable circumstances, one has no other recourse than to develop accurate numerical solutions of the primitive equations, study these solutions with the aim of identifying certain unifying physical principles, and then devise analytic and numerical tools and strategies to bridge the gap between the provenance of the eikonal and effective medium approaches.

Other contributions to the literature have pursued a similar objective. The recent publications by Shibata (1983), Oliver & Ballester (1995), Cargill, Spicer, & Zalesak (1997), Ofman & Davila (1998), Sakai, Igarashi, & Kawata (1998), Ofman, Nakariakov, & DeForest (1999), Terradas, Oliver, & Ballester (1999), Odrščil & Karlický (2000), Ofman, Nakariakov, & Sehgal (2000), Sakai et al. (2000, 2001), Bo & Wang (2001), and Oliver & Ballester (2002) present two-dimensional numerical simulations for a variety of magneto-atmospheres relevant for waves in coronal plumes, oscillations of magnetic prominences, Moreton and/or EIT waves, and general large-scale coronal dynamics. Fully three-dimensional problems are tackled by Wu et al. (2001) and Ofman & Thompson (2002). In large part these studies are motivated by the desire to explain various remarkable observations or to circumscribe the degree to which linear and nonlinear MAG waves are capable of heating the atmosphere and driving sustained mass flows. Within this framework, the simulations are chosen not so much for their pedagogical value as for their ability to mirror the complex reality of the solar atmosphere. There is ample room for both philosophies within this subject.

Related studies that adopt a diverse array of simplifying assumptions are more prevalent, and it is impossible to cite all of them here. The exact multidimensional simulations are essential for delimiting the circumstances under which these idealizations are valid. Some of the more popular approaches employ the magnetic field to reduce the effective spatial dimensionality of the problem (Mariska & Hollweg 1985; Sterling & Hollweg 1988; Kudoh & Shibata 1999; Nakariakov et al. 2000; Saito, Kudoh, & Shibata 2001; Tsiklauri & Nakariakov 2001), take the cold plasma limit  $\beta \rightarrow 0$ , which removes the  $\beta = 1$  magnetic canopy to infinity (Wright 1992; Walker 1998; Vogt 2002), or employ a non-physical gravitational acceleration (Beliën, Poedts, & Goedbloed 1997; Beliën, Martens, & Keppens 1999).

There is also a very well-developed literature on the problem of one-dimensional nonlinear wave propagation in

stratified atmospheres, which altogether neglects the magnetic field (Stein 1968; Einaudi 1969, 1970; Stein & Schwartz 1972, 1973; Cannon 1974; Schwartz & Stein 1975; Bois 1976; Klein, Stein, & Kalkofen 1978; Leibacher, Gouttebroze, & Stein 1982; Pelinovskii & Petrukhnin 1988; Pelinovsky & Petrukhnin 1994; Carlsson & Stein 1992, 1995, 1997, 2002; Schmitz & Fleck 1995; Theurer, Ulmschneider, & Cuntz 1997; Sutmann, Musielak, & Ulmschneider 1998). Two- and three-dimensional extensions of these studies are available, but with few notable exceptions they tend to focus exclusively on the linearized equations (Lamb 1908, 1910; Kato 1966; Cole & Greifinger 1969; Wait 1974; Yih 1974; Hammerton & Crighton 1989; Crighton & Lee-Bapty 1992; Borovikov 1996; Bodo et al. 2000).

In § 2 we provide an overview of the four numerical experiments that are the centerpiece of this paper. Each is represented by a cubic lattice of  $294 \times 500 \times (100\text{--}200)$  entries (i.e., altitude by horizontal distance by time) for every one of the six dependent variables (i.e.,  $\rho$ ,  $p$ ,  $\mathbf{B}$ , and  $\mathbf{u}$ ).<sup>3</sup> The bulk of the paper (§ 3) is devoted to a discussion and a critical analysis of how the MAG waves interact with their environment. This discourse is somewhat lengthy and moderately technical in places, but what gradually emerges from the consideration of these different numerical experiments is a predictive analysis scheme that is applicable to a much richer class of two-dimensional magneto-atmospheres. We believe this system is portable and will therefore prove useful to theorists and observers alike.

The transport and circulation of energy, a critical ingredient for assessing the role of wave heating of stellar atmospheres, is taken up in § 4. These deliberations prove to be largely unsatisfactory because the dominant component of the energy flux does not participate in the transfer of energy over large distances but is instead associated with stationary circulation patterns. There is clear evidence for long-range transport of energy by MAG waves, but it is not possible to quantify in an unambiguous fashion. We argue that a reliable determination of atmospheric heating by MAG waves must be derived from a self-consistent treatment of the wave propagation, mixing, and damping.

In § 5 we show how the analysis system developed in § 3 can be put to practical use by describing the possible behaviors of oscillations in and around the magnetic network and strong magnetic field concentrations, such as sunspots and knots. This exercise is quite instructive for documenting how incongruent the same oscillations may appear from distinct vantage points and in terms of different combinations of physical variables (i.e., Doppler velocity, intensity fluctuations, etc.). A critical summary of our findings and their limitations concludes the paper (§ 6).

## 2. SURVEY OF THE CALCULATIONS

In this paper we shall examine and analyze four different calculations. Several properties are common to all: the magnetic fields are potential and have the same relative distribution of magnetic field along the lower photospheric boundary of the computational domain (Fig. 1), and no field is allowed to thread the two side boundaries. All calculations therefore have *identical* magnetic field line systems.

<sup>3</sup> This works out to some 2.5 Gbytes of information. Fortunately, significant intellectual data compression is possible!

TABLE 1  
ISOTHERMAL ATMOSPHERE PARAMETERS

| Quantity                         | Value   |
|----------------------------------|---|
| Temperature .....                | 5785 K  |
| Density scale height.....        | 158 km  |
| Adiabatic sound speed .....      | $8.49 \text{ km s}^{-1}$                            |
| Ratio of specific heats.....     | 5/3   |
| Acoustic cutoff frequency.....   | 4.28 mHz  |
| Brunt-Väisälä frequency .....    | 4.19 mHz  |
| Gravitational acceleration ..... | $2.74 \times 10^4 \text{ cm s}^{-2}$                |
| Base pressure .....              | $1.13 \times 10^5 \text{ g cm}^{-1} \text{ s}^{-2}$ |
| Base density .....               | $2.60 \times 10^{-7} \text{ g cm}^{-3}$             |

The basic magnetic configuration consists of a large unipolar magnetic flux concentration surrounded on each side by two smaller concentrations of opposite-polarity field. The extent of the dominant flux concentration is approximately 2.0 Mm; the satellites are some 750 km wide. As illustrated by Figure 1, all three concentrations have a roughly Gaussian distribution of normal magnetic field strength. Outside the flux system, the magnetic field runs parallel to the lower (photospheric) boundary.

All four calculations possess identical hydrostatic isothermal atmospheres. The characteristic parameters are the same as those employed in Paper I, and for easy reference they are set out in Table 1. The base of the computational domain is representative of the solar surface. The top of the computational domain is situated at an altitude of 1.26 Mm. Attention is restricted to altitudes below 1.2 Mm in the plots we present to avoid spurious numerical artifacts associated with the upper boundary of the computational domain.

There are 294 computational zones in the vertical direction, yielding a numerical resolution of approximately 4.3 km per zone. There are 500 zones in the horizontal direction with a resolution of 15.8 km per zone (see Table 2). The lateral extent of the computational domain covers just under 8 Mm, or the equivalent of 4–6 granules. We stress that the computations are two-dimensional: there are no

TABLE 2  
NUMERICAL SIMULATION PARAMETERS

| Independent Variable               | Number of Zones/Steps | Extent of Zone/Step    | Range/Duration |
|------------------------------------|-----------------------|------------------------|----------------|
| $x$ -coordinate .....              | 500                   | 15.8 km                | 7.90 Mm        |
| $y$ -coordinate.....               | 1                     | $\infty$               | $\infty$       |
| $z$ -coordinate.....               | 294                   | 4.33 km                | 1.26 Mm        |
| $t$ -coordinate <sup>a</sup> ..... | 100–198               | 1.3 s                  | 130–257 s      |
| Piston period.....                 |                       | 23.8 s                 |                |
| Piston frequency .....             |                       | 42.9 mHz               |                |
| Piston amplitude.....              |                       | $400 \text{ m s}^{-1}$ |                |
| Piston location .....              |                       | 3.55–3.95 Mm           |                |

<sup>a</sup> The time step used within the numerical simulations is set by the Courant condition on the basis of the maximum value of the fast-wave phase speed. It is variable but is considerably less than the uniform sampling cadence of 1.3 s used in all the plots. Spurious reflections from the upper boundary generally limit the useful temporal duration of each of the four simulations. Transverse driving in the weak field has the shortest duration, 130 s, while radial driving in the weak field has the longest duration, 257 s. The simulations with the strong magnetic field lie intermediate between these two extremes, with durations of 192 s (transverse driving) and 209 s (radial driving).

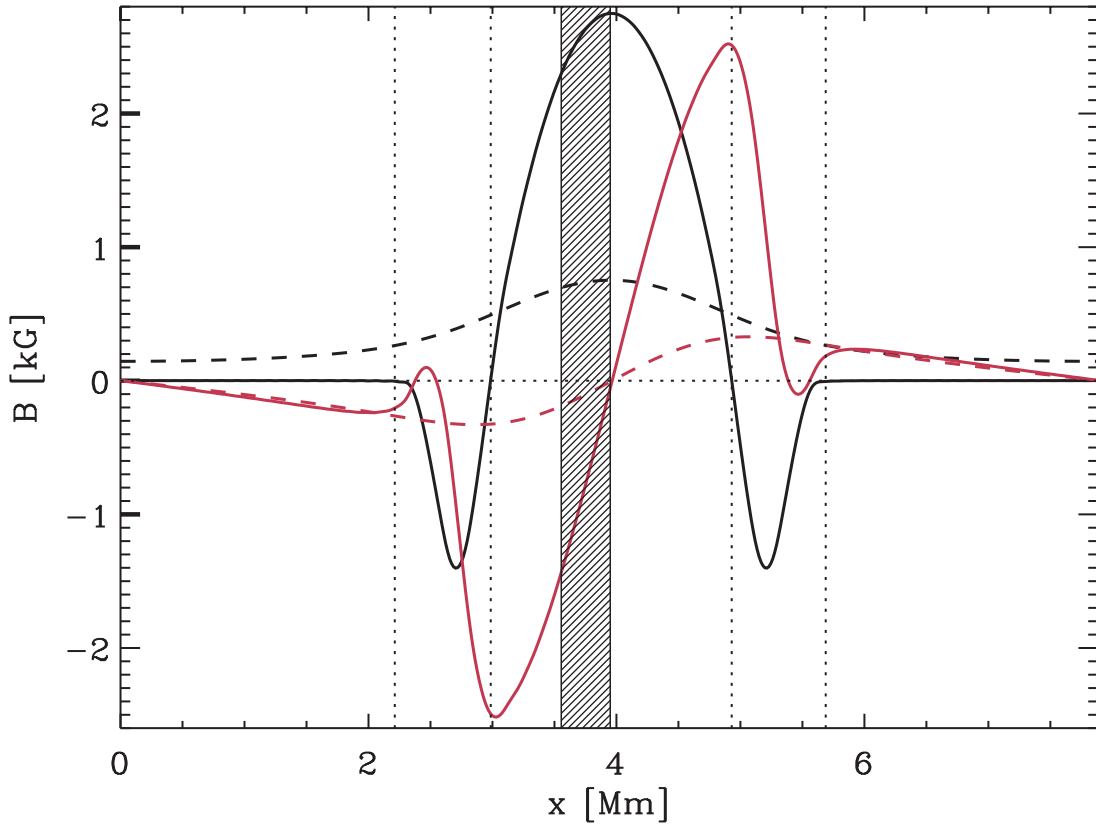


FIG. 1.—Distribution of the initial normal magnetic field,  $B_z$ , across the bottom (black solid line) and the top (black dashed line) of the computational domain. The analogous  $B_x$  curves, deduced from the potential magnetic field extrapolation, are plotted in red. The vertical dotted line segments show the approximate boundaries of the three magnetic flux concentrations: the central flux concentration is about 2 Mm wide, and the satellite reverse-polarity flux concentrations are approximately 750 km in extent. The stippled rectangle indicates the location of the photospheric driving piston. The piston is roughly 400 km across. The magnetic fields plotted here apply to the two *strong-field* calculations (§§ 3.1, 3.4); for the two *weak-field* calculations (§§ 3.2, 3.3) the field strengths are everywhere reduced by a factor of 4 (see also Table 3).

motions or components of the magnetic field in the direction normal to the data presented in the  $x$ - $z$  plots that follow. The critical implication of this restriction is that the intermediate or shear Alfvén wave is completely decoupled from the fast and slow MAG waves and therefore plays no further role in our discussion.

We solve the basic equations of ideal MHD,

$$\frac{\partial \rho}{\partial t} + \nabla \cdot (\rho \mathbf{u}) = 0, \quad (1)$$

$$\frac{\partial S}{\partial t} + \mathbf{u} \cdot \nabla S = 0, \quad (2)$$

$$\frac{\partial \mathbf{B}}{\partial t} - \nabla \times (\mathbf{u} \times \mathbf{B}) = 0, \quad (3)$$

$$\frac{\partial \mathbf{u}}{\partial t} + (\mathbf{u} \cdot \nabla) \mathbf{u} + \frac{1}{\rho} \nabla p = \frac{1}{4\pi\rho} (\nabla \times \mathbf{B}) \times \mathbf{B} - g \hat{\mathbf{z}}, \quad (4)$$

$$e = \frac{1}{\gamma - 1} \frac{p}{\rho}, \quad S = c_v \log(p/\rho^\gamma), \quad (5)$$

where all symbols have their usual interpretation.<sup>4</sup>

<sup>4</sup> This is not the exact set we use in the code, because some viscous dissipation is included in the momentum equation to regularize the computations at the smallest resolved spatial scales. Likewise, an equation for the internal energy is actually employed in place of the specific entropy. These distinctions, however, are unimportant for this discussion.

Periodic boundary conditions are applied on the side walls of the domain. A wave-transmitting boundary condition is enforced at the upper (chromospheric) boundary. In practice, a rather simple-minded procedure is employed to project the motions onto the local Riemann characteristics in the overlying “ghost zones.” The content of the incoming characteristics is set to zero to eliminate unwanted reflections and to suppress spurious wave sources at the upper boundary. The strategy is usually adequate for the low- $\beta$  fast wave. The steepened low- $\beta$  slow waves unfortunately suffer significant reflection from the upper boundary. Efforts are currently underway to remedy this limiting condition. The unavoidable reflection of waves back into the computational domain sets an upper limit on the useful temporal duration of the simulations to something on the order of 10 wave periods or less.

On the lower (photospheric) boundary, the horizontal velocity and the vertical velocity are specified as prescribed functions of time in the underlying ghost zones. The magnetic footpoints are line-tied to the imposed plasma motions. Outside the stippled region shown in Figure 1, this prescription is simply that *both* components of the fluid velocity are zero. Within the 400 km wide stippled region—the position of the localized wave source—the imposed motions are uniform and describe a pure sinusoid in time. The driving frequency is always 42 mHz, or equivalently a period of 23.8059 s. This is the same frequency/period employed in Paper I.

TABLE 3  
SURVEY OF THE FOUR CALCULATIONS

| Driving          | Weak Field                    | Strong Field                |
|------------------|-------------------------------|-----------------------------|
| Radial.....      | § 3.2, Figs. 10–17, 25–29, 31 | § 3.1, Figs. 2–9, 23–27, 30 |
| Transverse ..... | § 3.3, Figs. 18–22, 25–27     | § 3.4, Figs. 23–27          |

We retain this high-frequency (but here localized in space) wave source for two reasons. First, the corresponding wavelength for the low- $\beta$  fast wave just fits into the computational domain.<sup>5</sup> At lower frequencies the wavelength would be larger, so both the upper transmitting boundary condition and our ability to analyze the propagation characteristics in an  $8 \times 1.25$  Mm domain would be severely compromised. The reason is, of course, purely pragmatic. Second, given that the computational domain is necessarily a factor of 10 smaller in extent than one would wish to capture the essential wave dynamics of a sunspot, for example, by employing a period that is too small by the same factor of 10 (i.e., 42 vs. 4.2 mHz), one at least retains a correct relative scaling. In other words, the complex relationships between the morphology of the wave trains and the large-scale magnetic fields present in these simulations mimic those found in sunspots for the 5 minute oscillations. This follows because the characteristic propagation speeds—the sound speed  $c$  and the Alfvén velocity  $a$ —are basically the same for our small magnetic flux sheet and a large sunspot. The isomorphism is imperfect, however, because we cannot rescale the density scale height and the gravitational acceleration in a similar manner. Thus, upward-propagating low- $\beta$  slow (acoustic) waves steepen and shock “sooner” in a sunspot than in the scaled version studied in these calculations. Likewise the interesting dynamics that come into play when the oscillation frequency is close to the acoustic cutoff and Brunt-Väisälä frequencies cannot be addressed in this paper. The second reason is therefore still based in pragmatism, but it attempts to salvage some aspects of the physical problems suggested by solar observations.

It remains, therefore, to describe what allows one to distinguish between the four calculations. The differences are in the overall strength of the magnetic field and in the nature of the wave driving in the stippled region shown in Figure 1. For two of the four calculations, the magnetic field strength is given by the two solid curves plotted in Figure 1. We call these the “strong-field” cases. For the remaining two calcu-

lations, the magnetic field is everywhere *reduced by a factor of 4*. These are the “weak-field” cases. One should keep in mind that the actual magnetic lines of force are identical for the weak- and strong-field cases.<sup>6</sup> What is different is the location and orientation of the  $\beta = 1$  magnetic canopy layer. This distinction has a remarkable and quite profound impact on the wave activity in and about the magnetic flux concentration.

For two of the calculations, the horizontal velocity is also set to zero inside the stippled region, and the vertical velocity varies sinusoidally with a given amplitude. In other words, the photosphere moves up and down like a classical piston. The waves are thus generated by “radial driving.” For the remaining two calculations, the prescriptions for the vertical and horizontal velocities are exchanged, so the waves are generated by “transverse driving” at the photosphere. This is basically equivalent to shaking the embedded magnetic field lines back and forth at the photospheric boundary. Real solar wave sources are likely to present some superposition of radial and transverse driving motions. The two extreme conditions selected here bracket the actual possibilities.

Each of the four calculations corresponds to a unique combination of choices for the magnetic field strength and what might be termed the “polarization” (radial or transverse driving) of the wave source. The full matrix of possibilities is presented in Table 3.

### 3. ANALYSIS OF THE CALCULATIONS

In this section we embark on a general discussion of the wave generation, propagation, transformation, and interference manifest in each of the four representative calculations. We first take up a strong-field case, in which the low- $\beta$  plasma extends down to the lower (photospheric) boundary within the interior of the dominant flux concentration. This squeezes the high- $\beta$  plasma into the lower left and right corners of the computational domain. An important consequence of this separation is that most magnetic lines of force originating in the dominant flux concentration do *not* thread the  $\beta = 1$  magnetic canopy; *none* of the magnetic field lines connected to the wave source intersect the canopy. The important conclusion is that waves guided along the magnetic field from the source have no opportunity to interact with the magnetic canopy and transform into other waveforms.

We then turn to the two weak-field cases. In these examples, the magnetic canopy runs across the entire lateral

<sup>5</sup> This is particularly evident from a subsequent examination of Figs. 4, 6, and 7.

<sup>6</sup> A point that we repeatedly emphasize throughout the discussion.

TABLE 4  
MAGNETO-ATMOSPHERIC-GRAVITY WAVES

| Plasma              | Fast Wave   | Intermediate Wave <sup>a</sup>                          | Slow Wave  |
|---------------------|---|---|--|
| High- $\beta$ ..... | Acoustic-gravity wave, phase speed: $c$ , quasi-longitudinal <sup>b</sup> | Alfvén wave, phase speed: $a$ , transverse <sup>c</sup> | Guided along $\mathbf{B}$ , phase speed: $a$ , transverse <sup>c</sup>   |
| Low- $\beta$ .....  | Magneto-sonic wave, phase speed: $a$ , quasi-longitudinal <sup>b</sup>    | Alfvén wave, phase speed: $a$ , transverse <sup>c</sup> | Guided along $\mathbf{B}$ , phase speed: $c$ , longitudinal <sup>d</sup> |

<sup>a</sup> Alfvén waves are not considered in our two-dimensional simulations.

<sup>b</sup> The wavevector,  $\mathbf{k} \equiv \nabla\phi$ , where  $\phi(\mathbf{x}, t)$  is the phase of the wave, is fairly well (but not perfectly) aligned with the plasma velocity  $\mathbf{u}$ . The deviation between  $\mathbf{k}$  and  $\mathbf{u}$  generally depends on the angle between  $\mathbf{k}$  and  $\mathbf{B}$ .

<sup>c</sup> Also incompressible, i.e.,  $\nabla \cdot \mathbf{u} \approx 0$ .

<sup>d</sup> Also irrotational, i.e.,  $\nabla \times \mathbf{u} \approx 0$ .

extent of the computational domain. It dips within the dominant magnetic flux concentration, but it rarely falls below an altitude of 450 km. Most magnetic lines of force that emanate from the dominant flux concentration must intersect the magnetic canopy. On the other hand, the field lines emerging from the satellite reverse-polarity concentrations do not reach the mode-mixing zone but instead return to the photosphere in the flanks of the dominant-polarity region. Unlike the strong-field examples, the wave source is magnetically well connected to the canopy.

The subsequent discussions make frequent use of the characteristic properties of fast and slow MAG waves in high- and low- $\beta$  plasmas. A short resumé of their attributes are set out in Table 4 to aid the reader in following the deductive reasoning and mode identifications.

### 3.1. Strong-Field and Radial Driving

#### 3.1.1. Low- $\beta$ Slow Waves

The oscillating piston generates both fast and slow waves. We begin by examining the slow waves. In the low- $\beta$  plasma the slow MAG wave is an acoustic disturbance channeled along the magnetic field lines. The principal fluctuations associated with this disturbance are plasma motions aligned with the prevailing magnetic field, and alternating compression and rarefaction zones caused by the divergence of the fluid velocity. Since our simulation employs an adiabatic energy equation, the compressions and rarefactions are

essentially identical when viewed as density, pressure (i.e., internal energy density,  $e$ ), or temperature fluctuations.

In Figure 2 we provide a color rendering of the component of the fluid velocity parallel to the instantaneous magnetic field,  $u_{\parallel}(x, z)$ , at a time  $t = 58.5$  s from the start of the simulation. Because the piston period is 23.8 s, just over two and a half cycles of the driver have elapsed. This is clearly reflected in the two slabs of descending material (*red*) sandwiched between the three layers of upward-moving fluid (*yellow*).

The linear low- $\beta$  slow wave propagates at the adiabatic sound speed  $c(x, z, t = 0) \equiv c_0 = 8.49 \text{ km s}^{-1}$ . Accordingly, in Figure 2 we measure  $u_{\parallel}$  in units of  $c_0$ . As it progresses upward into regions of decreasing density, the velocity amplitude should increase in proportion to the inverse square root of the density. This well-known scaling is a consequence of one definition of the wave energy density,

$$E_{\text{wave}} = \frac{1}{2} \rho_0 |\mathbf{u}|^2 + \frac{1}{2\gamma p_0} |\Delta p|^2 + \frac{1}{2} \rho_0 \frac{N_0^2}{\omega^2} |\hat{\mathbf{z}} \cdot \mathbf{u}|^2 + \frac{1}{4\pi} |\Delta \mathbf{B}|^2, \quad (6)$$

where  $N$  is the Brunt-Väisälä frequency,

$$N^2 = \frac{g}{H_\rho} - \frac{g^2}{c^2}, \quad (7)$$

and  $H_\rho$  is the density scale height (here 158 km). The four

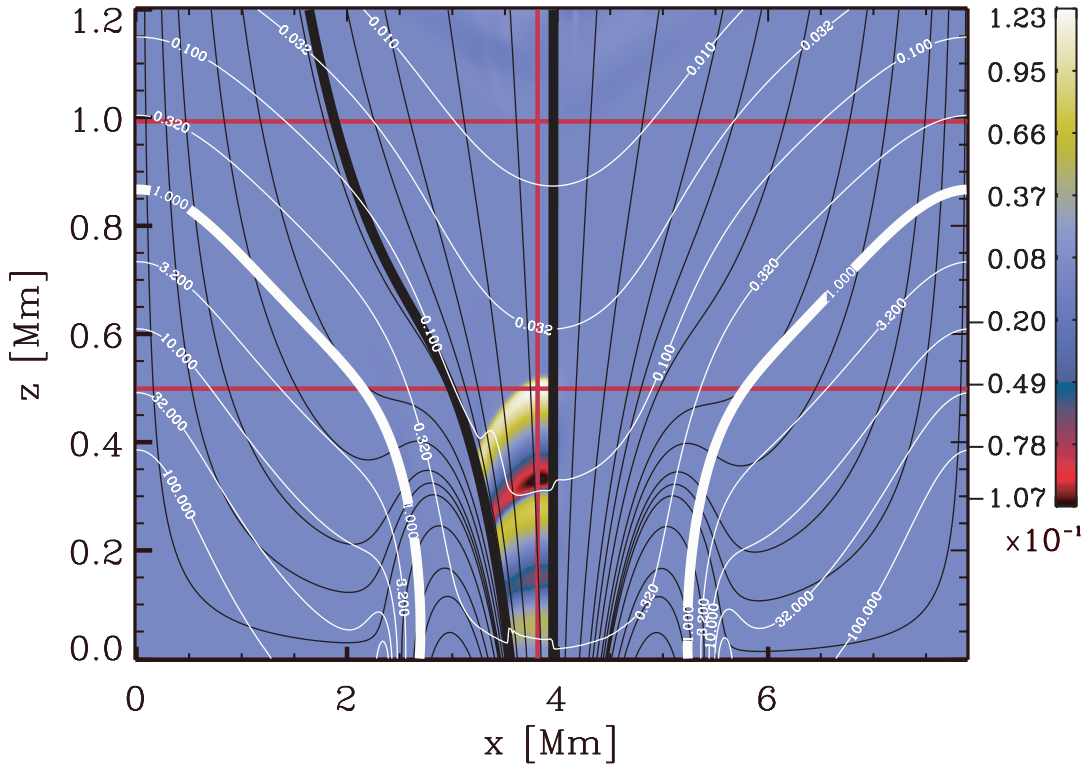


FIG. 2.—Rendering of  $u_{\parallel}(x, z)/c_0$  at an elapsed time of  $t = 58.5$  s, for radial driving in the strongly magnetized atmosphere (§ 3.1). The thin black lines represent random magnetic field lines: the two thick black lines are the field lines that attach to the edges of the driving piston. The thin white lines are iso-plasma  $\beta$ -contours, labeled by their appropriate value. The thick white lines mark the location of the  $\beta = 1$  magnetic canopy. The red lines locate two fiducial altitudes (499 and 993 km) and a lateral location (3.81 Mm) that figure in the subsequent analysis and later figures. This image shows the low- $\beta$  slow MAG wave. It is collimated by the magnetic field and is confined to the flux that connects back directly to the photospheric driving piston. There is some modest wave steepening occurring above  $z = 300$  km, but the Mach numbers of the upward- and downward-flowing material do not exceed 0.123 and 0.107, respectively, at this epoch. The peak Mach number imparted to the fluid by the driving piston is 0.047.

contributions to the energy density are the kinetic, the internal (thermal), the buoyancy (gravitational potential), and the magnetic components. The operator  $\Delta$  is defined by

$$\Delta f(x, z, t) \equiv f(x, z, t) - f(x, z, t = 0) \\ \equiv f(x, z, t) - f_0(x, z), \quad (8)$$

and  $f$  denotes any of the dependent variables (i.e.,  $\rho$ ,  $p$ ,  $\mathbf{u}$ , and  $\mathbf{B}$ ). In ideal linear MHD, the wave energy density is related to the wave energy flux through a canonical conservation law,

$$\frac{\partial E_{\text{wave}}}{\partial t} + \nabla \cdot \mathbf{F}_{\text{wave}} = 0, \quad (9)$$

where

$$\mathbf{F}_{\text{wave}} \equiv \Delta p \mathbf{u} + \frac{1}{4\pi} (\mathbf{B}_0 \cdot \Delta \mathbf{B}) \mathbf{u} - \frac{1}{4\pi} (\mathbf{u} \cdot \Delta \mathbf{B}) \mathbf{B}_0. \quad (10)$$

The last two terms are simply the Poynting flux. Other combinations of  $(E_{\text{wave}}, \mathbf{F}_{\text{wave}})$  consistent with equation (9) are in fact readily derived. Therein lies a particularly sticky point, to which we shall subsequently return in § 4.

At the atmospheric base, the driving piston imparts a 400 m s<sup>-1</sup> peak-to-peak velocity to the fluid (a Mach number of  $u/c_0 = 0.047$ ). There are approximately eight density scale heights in the domain, so if  $E_{\text{wave}}$  remained strictly constant with altitude, then velocity amplitudes on the order of 21 km s<sup>-1</sup> would be anticipated by an altitude of  $z = 1.2$  Mm. In other words, the motions associated with the slow wave would attain values comparable to the sound speed by an altitude of 960 km. In practice, nonlinear effects come into play before either of these critical altitudes is reached.

The waveform is continually distorted by the  $\mathbf{u} \cdot \nabla \mathbf{u}$  term in the momentum equation. Its principal function is to cause the portion of the wave train profile with a fluid velocity  $u$  to advance at the speed  $u + c$ . In this fashion, the disturbances associated with the faster motions of the driving piston eventually overtake the slower propagating disturbances. The initial sinusoid is thus distorted into an N-wave (Earnshaw 1860; Courant & Friedrichs 1948; Westervelt 1950; Blackstock 1962; Naugol'nykh 1971; Whitham 1974; Anile et al. 1993). In a stratified atmosphere, both the nonlinear advection and the density falloff with height act in concert to steepen and distort the wave profile (Einaudi 1970; Anile, Mulone, & Pluchino 1980). The formation of a shock discontinuity occurs when adjacent characteristics eventually intersect. For an adiabatic simple wave in an isothermal atmosphere, formulae for shock formation heights have been given by Stein & Schwartz (1972) and Anile et al. (1980). When viscous dissipation is present, strict discontinuities are not attained, but rather a sharp but continuous transition forms. As Fay (1931) remarked, "Since the effect of viscosity is to attenuate the higher frequency components more than the lower, there is always a waveform having the harmonic components in a stable relation such that the decrease in relative magnitude of any component due to viscosity is compensated by the relative increase due to non-linearity" (Rankine 1870; Rayleigh 1910; Fay 1931; Blackstock 1965; Hammerton & Crighton 1989).

This evolutionary scenario is basically corroborated by the results of the numerical simulation displayed in Figures 2–4. With Figure 3 we provide a color rendering of the fractional density fluctuations,  $\Delta\rho(x, z)/\rho_0(z)$ , at a later elapsed time  $t = 123.5$  s. This plot encompasses a restricted region

of the computational domain; it also conveys a realistic aspect ratio between the vertical and horizontal scales. As expected, the slow waves are still well contained within the magnetic flux that is directly connected to the piston.<sup>7</sup> Very slight extensions of the wave fronts beyond this flux bundle are visible. In this regard it is interesting to observe the continuations of the  $\beta$ -contours to the right of the vertical bounding magnetic field line (at  $x \approx 3.96$  Mm). Beyond this boundary, the contours no longer simply follow the density fluctuations (compare the  $\beta = 0.01$  and 0.032 contours), as they are forced to do throughout the interior of the piston-connected magnetic flux.<sup>8</sup> From this we may surmise that sensible magnetic field fluctuations are present beyond the boundary of the flux bundle. Some weak boundary coupling into the fast wave is present here.

In Figure 4, we focus on the wave steepening and distortion that is taking place along the vertical red line ( $x = 3.81$  Mm) prominently marked on Figures 2 and 3. It would of course be preferable to view this evolution along a fixed magnetic field line. This would entail interpolating the  $x$ - $z$  grid onto an  $A$ - $z$  grid, where  $A$  is the vector potential. Since the piston driving is uniform and the magnetic field is mostly vertical over the piston, there is only a minor disadvantage in simply looking along a line of constant  $x$  instead of a line of constant  $A$ . We shall thus pursue this path of least resistance.

The basic format of Figure 4 is similar in many respects to that of Figures 2 and 3, except that the elapsed time now runs along the abscissa. The contours of constant plasma  $\beta$  move up and down in altitude with the passage of the compressions and rarefactions, but we have not plotted the magnetic field lines. Fractional density fluctuations are again displayed in this figure. The distortion of the symmetric sinusoidal waveform (below  $z = 200$  km, say) into the N-wave is easy to see. The first slow-wave compression and rarefaction are particularly instructive. The solid black line provides a reference for upward propagation at  $c_0 = 8.49$  km s<sup>-1</sup>. Note how the upward-propagating compression pulls away from the linear wave trajectory, while the rarefaction slowly falls behind this pace. The thin red lines are close to the linear portion of the waveform and therefore nicely parallel the heavy black line. In the corner above the heavy dot-dashed black line, the upward-propagating slow waves suffer fairly regular modulation in both space and time. In this corner, slow waves that have reflected from the upper boundary of the computational domain ( $z = 1.26$  Mm) interfere with the main wave train.

Figure 5 presents these same data in a different format. The continuous curves plotted in this figure show the instantaneous state of the atmosphere at  $x = 3.81$  Mm for the time  $t = 123.5$  s, that is to say, the profiles along the vertical red line marked in Figure 4. One now sees better the steepening through the transformation from a sinusoid below  $z = 150$  km to an N-wave profile above 300 km.<sup>9</sup> The density contrast and the parallel Mach number (Fig. 5, *solid black curve*

<sup>7</sup> The magnetic field lines that bound the piston-connected magnetic flux are shown as thick black lines in Figs. 2, 3, and subsequent figures.

<sup>8</sup> Within the piston-connected flux bundle, there are essentially no magnetic field fluctuations associated with the slow wave. The fluctuations in  $\beta$  therefore derive entirely from the variations in the fluid pressure, which are in turn directly tied to the density through the condition of isentropy and the caloric relation.

<sup>9</sup> Recall that the ambient density scale height is 158 km.



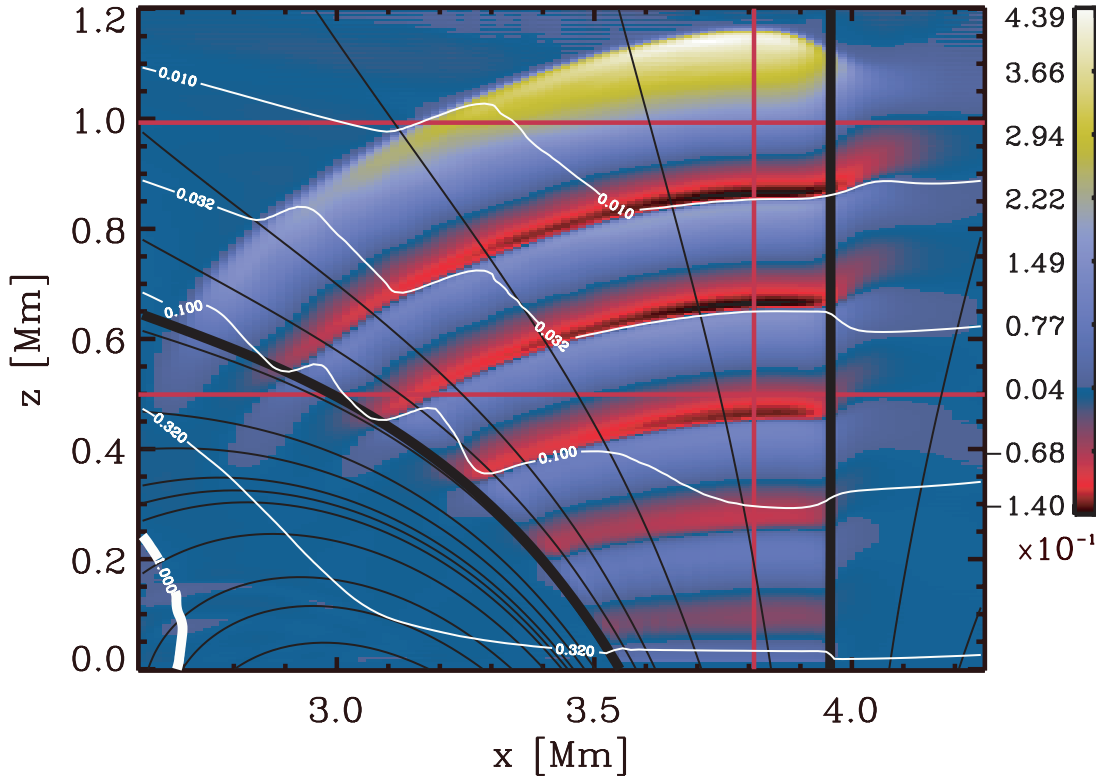


FIG. 3.—Relative density fluctuations  $\Delta\rho(x, z)/\rho_0(z)$  at an elapsed time of  $t = 123.5$  s. Black, white, and red lines serve the same functions as in Fig. 2. Only a small portion of the computational domain is shown. It is selected to realistically portray the correct spatial aspect ratio. The fortuitous break in the color table around 0.004 allows one to discern the weakest density fluctuations that extend beyond the magnetic flux connected directly to the driving piston. This snapshot again shows only the low- $\beta$  slow MAG wave, and relative to the view presented in Fig. 2 the nonlinear distortion of the wave fronts is well developed. The iso- $\beta$  contours display a sequence of steps as a consequence of the density enhancements and depletions present in the wave train. Even at this rather advanced and quite nonlinear stage, one sees that the slow wave is basically confined to the piston-connected magnetic flux.

on bottom) saturate at rather modest values because of the viscosity present in the simulation. With only 294 computational zones in the vertical direction, the spatial extent of the N-wave front is bounded from below by 3–5 zones, or 10–20 km. This limits the continued growth of the compression ratio across these sharp transitions. The point is further illustrated by the two curved dashed lines that outline the envelope of the parallel Mach number in the lower panel. The upper line is fitted by  $u_{\parallel}/c \sim \rho_0^{-2/7}$  and the lower by  $u_{\parallel}/c \sim -\rho_0^{-2/5}$ . Both fall decidedly short of the the  $u_{\parallel}/c \propto \rho_0^{-1/2}$  scaling expected for an ideal linear wave.

From the Rankine-Hugoniot relations one has

$$\frac{\rho_+}{\rho_-} = \frac{(\gamma + 1)M^2}{(\gamma - 1)M^2 + 2}, \quad (11)$$

where the subscripts distinguish quantities upstream (+) and downstream (−) from the shock,

$$M \equiv \frac{U - u_+}{c_+}, \quad (12)$$

is the shock Mach number, and  $U$  is the shock speed in the fixed frame of the atmosphere. Using the data provided in Table 1 and the information presented in Figure 5, we may assign shock Mach numbers of 1.24 and 1.26 to the two strongest shocks on the basis of the observed compression ratios. Note that this is consistent with  $U \approx c_0$  because of the infall of material into the shock ( $u_+ < 0$ ) from the rarefaction of the previous cycle.

The instantaneous profiles (reckoned at  $t = 123.5$  s) are surrounded by a swarm of small dots. These dots show all values of  $\Delta\rho(x, z, t)/\rho_0(z)$  (Fig. 5, *top*),  $u_{\parallel}(x, z, t)/c(x, z, t)$  (*bottom*; black dots), and  $u_{\perp}(x, z, t)/c(x, z, t)$  (*bottom*; red dots) recorded at  $x = 3.81$  Mm. In all, 160 values are present at each altitude with uniform sampling ( $\Delta t = 1.3$  s) over 209 s. This display effectively delineates the amplitude envelope of the wave train.

With the density fluctuations, one finds a prominent asymmetry between the maximal positive and negative density fluctuation excursions. The asymmetry may be characterized by a “zero offset,”  $\delta(z)$ , defined as the arithmetic mean of the maximum and minimum values of  $\Delta\rho/\rho_0$  recorded at each altitude. The variation with altitude of this quantity is provided by the overplotted solid red curve of Figure 5 (*top*). While these data show a fair amount of scatter, which results from the coarse time sampling and the restricted duration of the simulation, a clear trend with altitude is nevertheless present.

For the most part, it is reasonable to associate the zero offset,  $\delta(z)$ , with the longtime average of  $\Delta\rho(z, t)/\rho_0(z)$ . The association clearly goes awry near the base of the atmosphere, where the piston intrudes into the computational domain, and also above an altitude of approximately 800 km. This latter discrepancy occurs because the initial compressive pulse propagates into a quiescent atmosphere, whereas the subsequent compressions overrun the rarefactions associated with the second half of the previous oscillation cycle. The first pulse is therefore capable of attaining



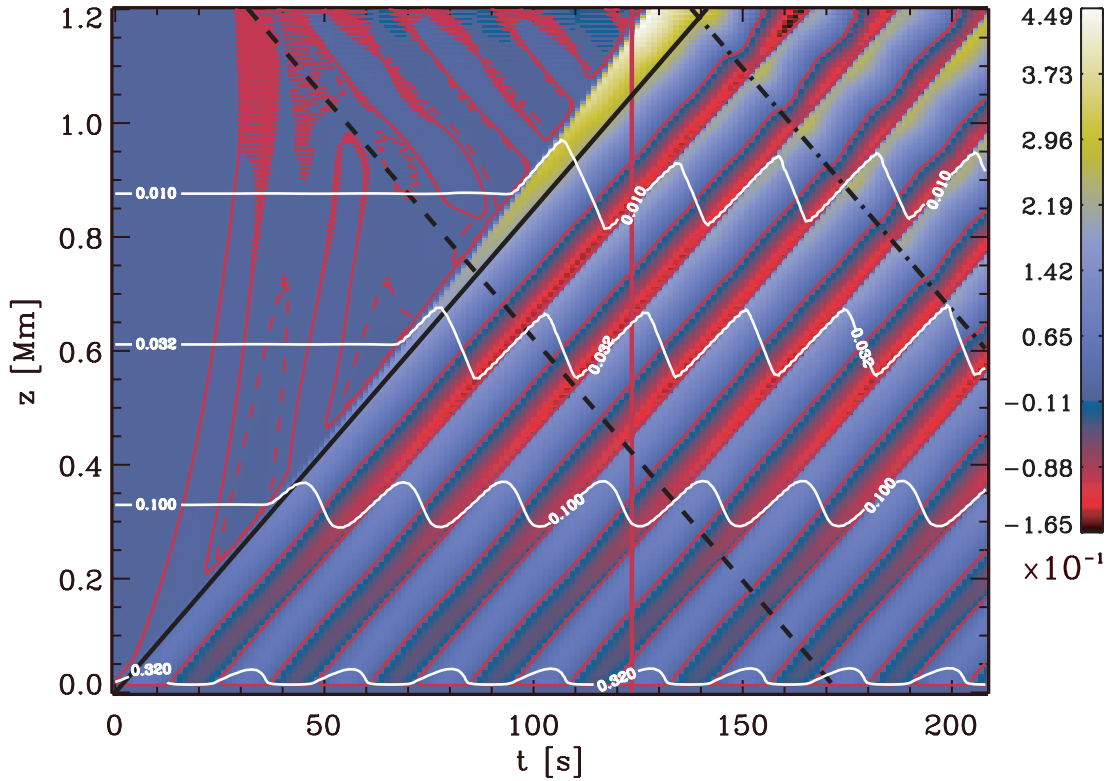


FIG. 4.—Altitude vs. time slice of the fractional density fluctuations  $\Delta\rho(z, t)/\rho_0(z)$  as recorded at  $x = 3.81$  Mm (Figs. 2 and 3; vertical red line). The thin white lines are contours of constant values of the plasma  $\beta$ , and they are observed to periodically move up and down in altitude with the passage of the compressions and rarefactions of the slow wave. The solid black line that passes through the origin gives the trajectory of a linear acoustic wave launched at  $t = 0$  that travels vertically at the sound speed  $c_0 = 8.49$  km s $^{-1}$ . The two broken black lines do the same for downward-propagating waves launched from the upper boundary of the computational domain ( $z = 1.26$  Mm) at two different times. The steepening of the first slow wave is illustrated both by the evolution of the density profile across the front from sinusoidal to linear and by the tendency for the compressed N-wave front to propagate faster than  $c_0$ , while the rarefacted rear travels more slowly. Some slow waves are reflected back into the domain and produce the weak modulation in the corner above and to the right of the dot-dashed line. Two additional red contours are overplotted (at  $\pm 10^{-3}$ ) to bring out the weakest density fluctuations that outrun the slow-wave train. These structures are due to the low- $\beta$  fast MAG wave.

larger density enhancements and flow Mach numbers than the subsequent N-waves. This is evident from Figure 4. One might remedy this problem by discarding the excessive values associated with the first pulse, but the crudeness of the ensuing analysis does not justify such efforts. In the estimates that follow we will be content to avoid regions where the association is clearly unreliable.

With the exception of a slight deficit aloft, between the altitudes of 370 and 570 km, this association implies a general increase of the atmospheric density above the piston. This may be interpreted as a lifting of the atmosphere because of momentum transfer between the wave train and the fluid. One commonly attributes this to a “pressure gradient” associated with the waves (Gail, Cuntz, & Ulmschneider 1990; Litwin & Rosner 1998). Conservation of mass requires a region where the density is depleted just adjacent to the piston. The zero offset fails to capture this nuance. This effect is well known in the one-dimensional hydrodynamic simulations, in which it is convenient to think in terms of the elevation of curves of constant column mass. The net elevation of the atmosphere found here is on the order of 5% of the density scale height, consistent with a zero offset of  $\Delta\rho/\rho_0$  of the same basic order of magnitude. One may also infer that the *actual* vertical excursions of a given atmospheric layer are an order of magnitude larger

than the *average* elevation gain of some 8–10 km. More vigorous piston motions would of course lead to a larger effect.

### 3.1.2. Low- $\beta$ Fast Waves

The piston also emits fast MAG waves, and hints of their presence have already surfaced in the last two figures (i.e., Figs. 4 and 5). They experience a wholly different fate than their slow counterparts. The fast wave is not confined to the magnetic flux slab connected to the driving piston, nor does it steepen and suffer appreciable dissipation. This wave train is also created deep within the low- $\beta$  interior of the dominant magnetic flux concentration. However, as it is able to propagate across the magnetic field lines, it does eventually encounter the  $\beta = 1$  magnetic canopy.

Figures 6 and 7 provide two snapshots of the fast-wave evolution. In both figures we show the component of the fluid velocity perpendicular to the magnetic field,  $u_\perp(x, z, t)$ , divided by the constant sound speed ( $c_0 = 8.49$  km s $^{-1}$ ). It is worth noting that the fast wave has motions along and perpendicular to the magnetic field, as well as density enhancements and rarefactions. We choose to view this wave in  $u_\perp$  because the slow wave does not contribute to this motion and is thus effectively screened out from these two figures. This is critical since the driving piston creates more slow waves than fast waves. The component of the

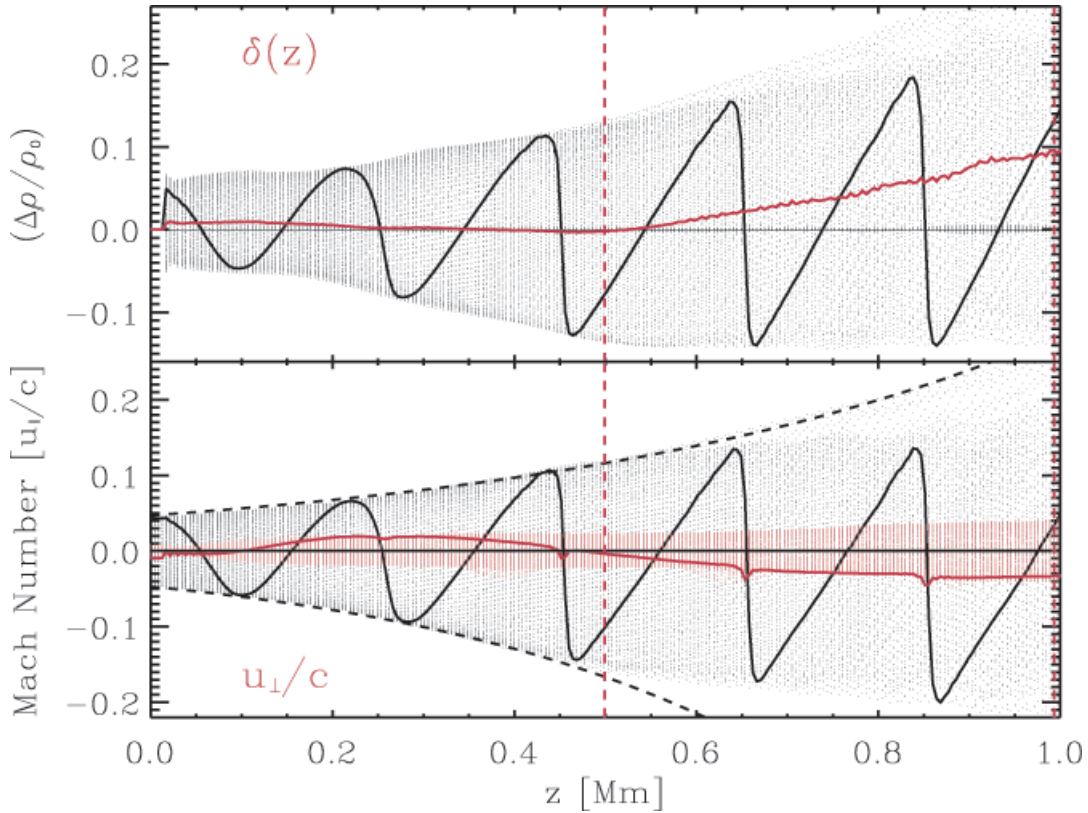


FIG. 5.—Fractional density fluctuations  $\Delta\rho(z, t)/\rho_0(z)$  (top) and the Mach numbers (bottom), recorded at the point  $x = 3.81$  Mm within the driving piston. The solid curves show these quantities at an elapsed time of  $t = 123.5$  s, that is, the same time shown in Fig. 3 and indicated by the vertical red line in Fig. 4. Values at 160 successive time steps separated by 1.3 s are plotted with individual dots. *Bottom*: Motions aligned with the magnetic field  $[u_{\parallel}(z, t)/c(z, t)]$  are in black, and those perpendicular to the field  $[u_{\perp}(z, t)/c(z, t)]$  are in red. *Top*: Fractional density offset,  $\delta(z)$  (solid red curve), defined in the text. The black dashed curves are empirical fits to the envelope of the parallel Mach number data points. The lower curve has an  $e$ -folding length of 395 km ( $2.5 H_p$ ), and the upper curve has 553 km ( $3.5 H_p$ ). This perspective is complementary to Fig. 4. It shows that the magnetic field-aligned motions mirror the density fluctuations, but it also reveals the presence of small-amplitude transverse waves with a very much larger vertical wavelength. These fluctuations signal the presence of the low- $\beta$  fast MAG wave.

vorticity in the  $y$ -direction would also show the fast wave and filter out the slow wave.

Figure 6 corresponds to an elapsed time of 27.3 s, that is, just after one period, while Figure 7 is obtained after  $t = 58.5$  s, or at the same instant  $u_{\parallel}$  is depicted in Figure 2 (i.e., just after two and a half cycles). The characteristic shape of the fast-wave train is a nested sequence of inverted “teardrops.” The compression phase of the piston produces a positive  $u_x$  (negative  $u_{\perp}$ ), and the rarefaction induces the opposite sense of displacement. The linear fast wave may travel as fast as  $[c^2(x, z, t) + a^2(x, z, t)]^{1/2}$ , depending on its direction of propagation. While the sound speed is essentially constant throughout the computational domain, the Alfvén velocity increases rapidly with altitude. In fact, the  $\beta$ -contours are essentially contours of constant Alfvén velocity.<sup>10</sup> Thus, the apex of the wave front accelerates out through the top of the computational domain, leaving the legs of the front to gradually make their way laterally toward the magnetic canopy. The acceleration of the leading edge of the front relative to the trailing portion inhibits the steepening of the wave profile. Likewise, the two-dimensional expansion across the magnetic lines of force

also acts to spread the energy over a larger area. Both effects prevent the associated Mach numbers from exceeding a few parts per hundred.

In Figure 7 we observe over two complete cycles of the fast-wave train. The leading edge of the first complete oscillation has exited through the top of the domain, leaving legs of the teardrop on both sides (*dark blue leading gold*). The very apex of the second oscillation (*red horseshoe*) lies just above the top of the plot; the corresponding rarefaction is the gold horseshoe below. A careful comparison of Figure 7 with Figure 2 shows that the leading edges of the compressive slow N-waves bleed through as the two thin curved striations within the piston-connected flux bundle.<sup>11</sup> Returning to Figure 5 (*bottom*), we observe the variations of  $u_{\perp}/c$  along the red vertical line ( $x = 3.81$  Mm) overplotted on Figures 6 and 7, displayed as the red dots. The amplitude envelope of the transverse Mach number increases rather modestly by a factor of 3–4 over the first megameter of altitude. The large vertical wavelength of the low- $\beta$  fast wave is also clearly documented by the overplotted instantaneous profile ( $t = 123.5$  s).

<sup>11</sup> See also the small “spikes” on the instantaneous  $u_{\perp}/c$  curve displayed in Fig. 5 (*bottom*) that are coincident with the zero crossings of  $u_{\parallel}/c$  in the N-wave fronts.

<sup>10</sup> Viz.,  $\beta = 8\pi p/B^2 = (2/\gamma)(c^2/a^2)$ .

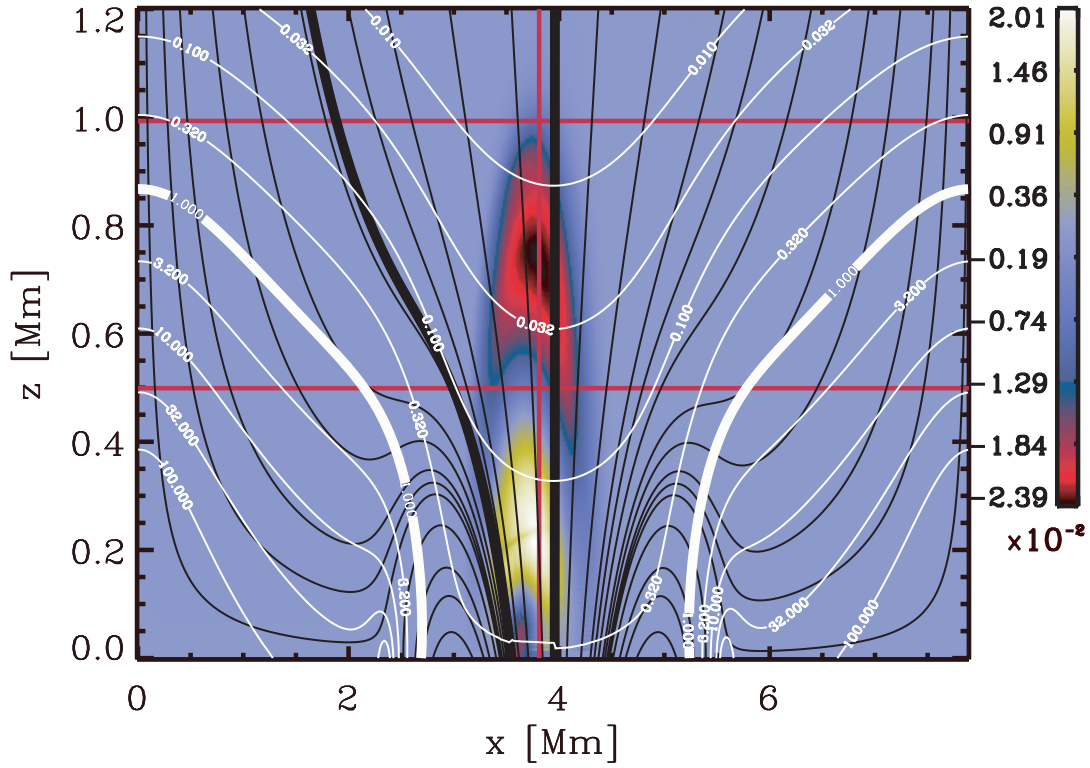


FIG. 6.—Rendering of  $u_{\perp}(x, z)/c_0$  at an elapsed time of  $t = 27.3$  s, for radial driving in the strongly magnetized atmosphere (§ 3.1). Red, white, and black lines serve the same function as in Figs. 2 and 3. The area depicted is the same as in Fig. 2 but at an earlier epoch. This shows just over one cycle of the low- $\beta$  fast wave. The outer horseshoe portion of the wave represents motion of the material to the right with a peak Mach number of 0.0239; the inner yellow teardrop indicates material moving to the left. Note that the shape of the fast wave is not confined to the piston-connected magnetic flux. A faint thin dark blemish within the yellow teardrop identifies the first slow-wave front.

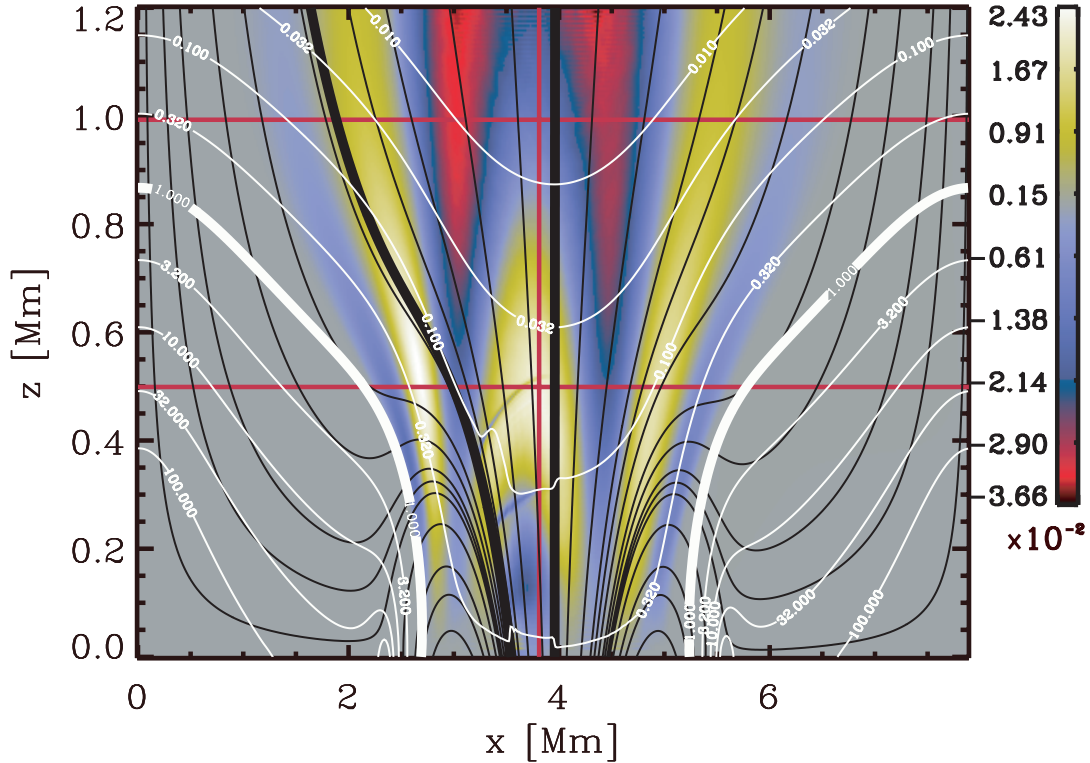


FIG. 7.—Identical to Fig. 6 *except* obtained at a later elapsed time,  $t = 58.5$  s. The time is the same as that used in Fig. 2, where the other orthogonal velocity component,  $u_{\parallel}/c_0$ , is displayed. A comparison of this snapshot with Fig. 2 emphasizes the distinct character and propagation speeds of the low- $\beta$  fast and slow waves. Only the thin legs of the horseshoe and the teardrop of Fig. 6 remain within the computational domain on the far left and right. The concave-outward shape of the legs is a consequence of the greater Alfvén velocity aloft. The fast wave has just reached the low canopy on the left.

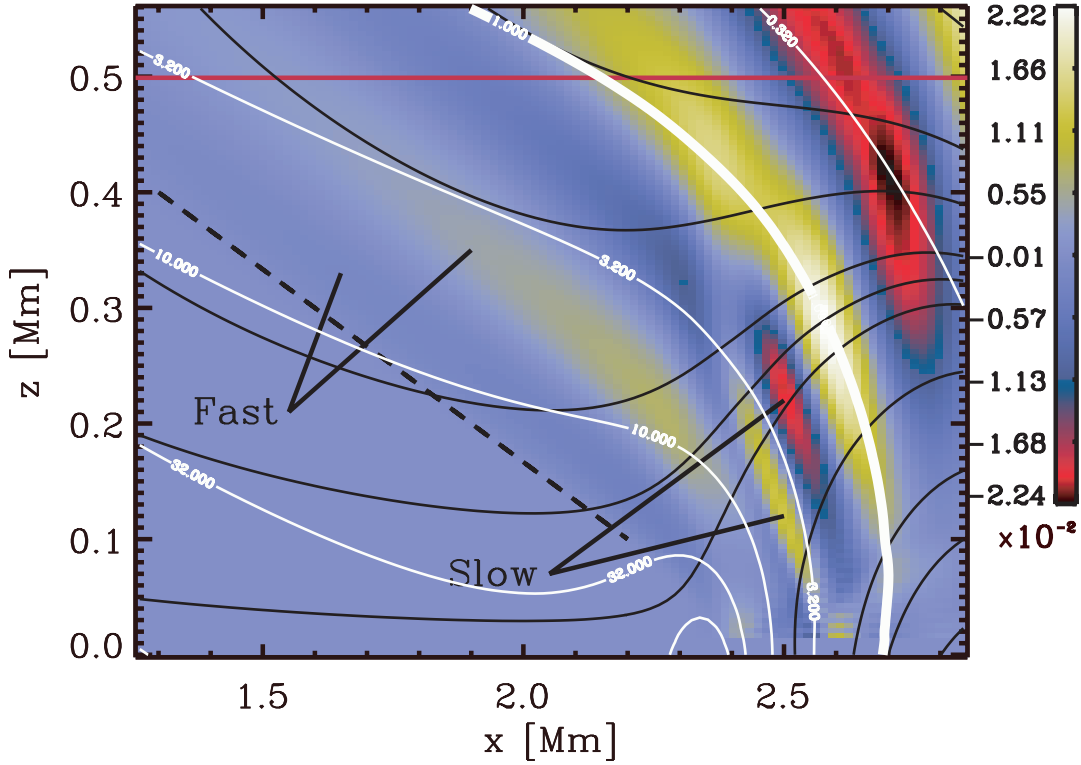


FIG. 8.—Enlargement of a region to the left of the main flux concentration of Fig. 7, but at a later time,  $t = 97.5$  s. This snapshot again shows  $u_{\perp}(x, z)/c_0$ . The first oscillation has completely passed through the canopy and has been converted into both the fast and slow high- $\beta$  waves. The faint leading edge of the transmitted fast-wave train is coincident with the dashed line. The slow waves emerge preferentially where the magnetic field is perpendicular to the canopy. They have a smaller wavelength and are channeled downward along the magnetic field.

The variation of the fast-wave speed with position causes the teardrop legs to bend and take on the same basic shape and orientation of the magnetic canopy (Flå et al. 1984) as they approach from above on the low- $\beta$  side. Thus the wavevectors of the incident fast-wave train are nearly co-aligned with  $\nabla\beta$  in the mode conversion zone. In principle, the incident low- $\beta$  fast wave can convert to transmitted and reflected slow and fast waves along the canopy. In practice, only the transmitted wave channels are favored; few if any reflected waves are visible. Figure 8 shows details of the mode conversion process. In this plot we focus on the motions perpendicular to the magnetic field ( $u_{\perp}/c_0$ ), since they permit one to distinguish *both* the fast and slow waves in the high- $\beta$  region.<sup>12</sup>

From Figure 8 we see that the first cycle of the impinging low- $\beta$  fast wave has been completely transmitted across the magnetic canopy. The transmitted fast wave in fact appears along the entire length of the canopy. It is easy to identify along the upper portion of the magnetic canopy. This is because of the fortuitous alignment of the wave fronts and the prevailing magnetic field: the full fluid displacement is thus captured by  $u_{\perp}$ . Elsewhere along the transmitted fast-wave front the motions remain aligned with the wavevector, while the magnetic field takes on orientations that are less favorable for this motion in  $u_{\perp}$ . The transmitted fast waves are therefore more difficult to discern in these locations.

<sup>12</sup> Recall that the high- $\beta$  fast wave is basically a compressive longitudinal (i.e., motions aligned with the local wavevector) acoustic-gravity wave. The magnetic field runs mostly parallel to the canopy in Fig. 8 (top). Thus, the fast wave longitudinal motions are captured by the perpendicular Mach number.

Another source of confusion and obscuration is waves subsequently reflected from the lower boundary of the computational domain. In Figure 8 they are confined to the lower right corner of the plot, but at the later time shown in Figure 9, they occupy a more substantial fraction of the quiet Sun surrounding the sunspot.

The transmitted slow wave, on the other hand, is found only in a restricted portion of the magnetic canopy. Below  $z \approx 400$  km the magnetic field tends to run parallel to  $\nabla\beta$  through the canopy. Elsewhere the opposing configuration prevails. Since the slow wave is guided along the magnetic field lines, it may escape from the mode conversion region into the high- $\beta$  plasma only where a quasi-parallel orientation is present. Where the field lines run along the magnetic canopy, slow waves are retained within the mode conversion zone and are unable to disentangle themselves from the fast wave. For this reason, the transmitted slow waves emerge from the magnetic canopy only between the altitudes of 100 and 400 km.<sup>13</sup>

Figure 9 shows this same region at a later time. Here one can see the full development of the transmitted high- $\beta$  slow-wave train. It is worth pointing out that the magnetic field guides these waves into regions of progressively higher density and lower Alfvén velocity; therefore, the wavelength decreases downward along the field lines. Viscous dissipation ultimately takes over when the wavelength decreases

<sup>13</sup> In Figs. 8 and 9 the emergent high- $\beta$  slow waves extend down to the photosphere. They propagate to the atmospheric base after their creation at higher altitudes along the field lines rooted in the satellite reverse-polarity magnetic flux concentration.



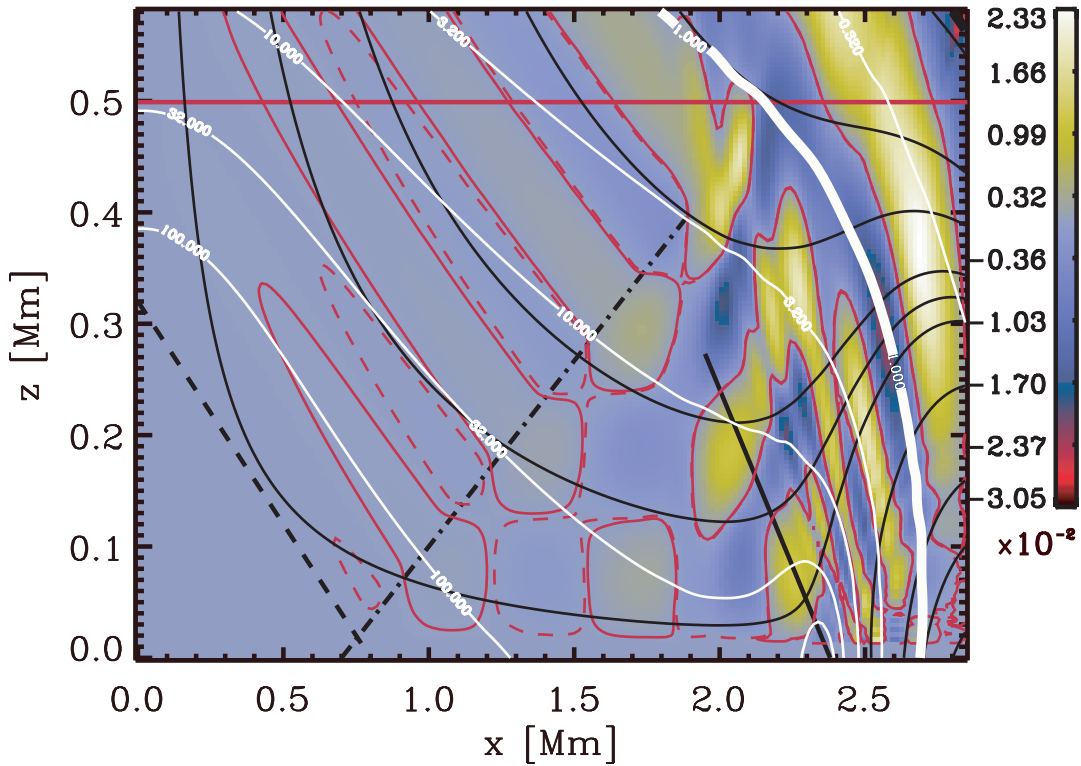


FIG. 9.—Continuation in time of the mode conversion displayed in Fig. 8. The elapsed time is  $t = 158.6$  s, and here the slow-wave train is well developed between the canopy and the solid line segment. The wavelength decreases as the slow wave progresses into regions with larger  $\beta$  (smaller Alfvén velocity). The leading edge of the transmitted high- $\beta$  fast wave is again marked by the dashed line. The wave amplitude, hence the visibility, goes down as it travels into denser fluid and spreads over a larger area. The fast wave reflects from the rigid photosphere and interferes with the incoming fast waves to generate the checkerboard pattern below and to the right of the dot-dashed line. To bring out these weak fast-wave features, two red contour levels at  $10^{-4}$  (solid line) and  $-10^{-4}$  (dashed line) have been added. The slow waves also reflect from the photosphere, producing the fine-scale wiggles near the footpoints of the slow-wave train. The menagerie of waves traveling through this image underscores the potential for complex interference patterns to develop on the high- $\beta$  side of the magnetic canopy.

below a critical value. In the present case, of course, numerical dissipation sets in sooner. A final remark about Figure 9 concerns the wave reflection and transformation from the lower boundary. As the fast wave impinges on the lower boundary of the domain, it may reflect back as both slow and fast waves. Different channels are favored, depending on the field orientation and the ratio of gas to magnetic pressure. The specular reflection of the fast-wave fronts from the rigid photosphere is most obvious in the checkerboard interference pattern they create with the incident high- $\beta$  fast waves. A mixture of reflected waves is also created within the closed-field region from the interaction of the high- $\beta$  slow waves with the magnetic line-tied photosphere. They are barely perceptible as the fine-scale wiggles that modulate the low-lying extensions of the low- $\beta$  slow-wave fronts. These reflected slow waves propagate upward and back toward the magnetic canopy along the field lines.<sup>14</sup>

### 3.2. Weak-Field and Radial Driving

In this section we now consider a second, slightly different, calculation. We retain all the conditions of the first simulation analyzed in § 3.1 (or equivalently Figs. 2–9), *except* that the magnetic field strength is everywhere *reduced* by a factor of 4. Figure 10 is now obtained in place of Figure 2.

<sup>14</sup> Given the somewhat artificial nature of this process and setting issues of magnetic field line tying aside, we do not pursue this further in this paper. For an amplification on this point, see Bogdan et al. (2002).

Note that the structure of the magnetic field is left entirely unchanged by a uniform weakening of the field. The shape of the iso- $\beta$  contours is *also* unchanged; however, the labels attached to the contours are reassigned to reflect the decrease in the magnetic pressure. In particular, the heavy  $\beta = 1$  magnetic canopy contour no longer threads the lower boundary, but instead it separates the domain into two simply connected regions.

#### 3.2.1. High- $\beta$ Fast Waves

The driving piston is now situated in a high- $\beta$  region; consequently, the compressions and rarefactions it creates couple most efficiently to the high- $\beta$  fast wave. This MAG wave was previously encountered in Figures 8 and 9, where it was generated by mode conversion across the magnetic canopy. In Figures 10, 11, and 12 it is produced directly by the driver. In a stratified atmosphere, this fast wave is essentially an acoustic-gravity wave since the magnetic field is of little consequence in high- $\beta$  regions. As our driving frequency is a factor of 10 larger than the Brunt-Väisälä and the acoustic cutoff frequencies, the “acoustic” character dominates and we have a longitudinal—motion aligned with the normal to the wave front (i.e., the wavevector)—compressive wave.<sup>15</sup>

<sup>15</sup> For frequencies below the Brunt-Väisälä frequency, the internal gravity wave character would apply. However, even in a high- $\beta$  plasma, the magnetic field can become important for gravity waves with short horizontal wavelengths.

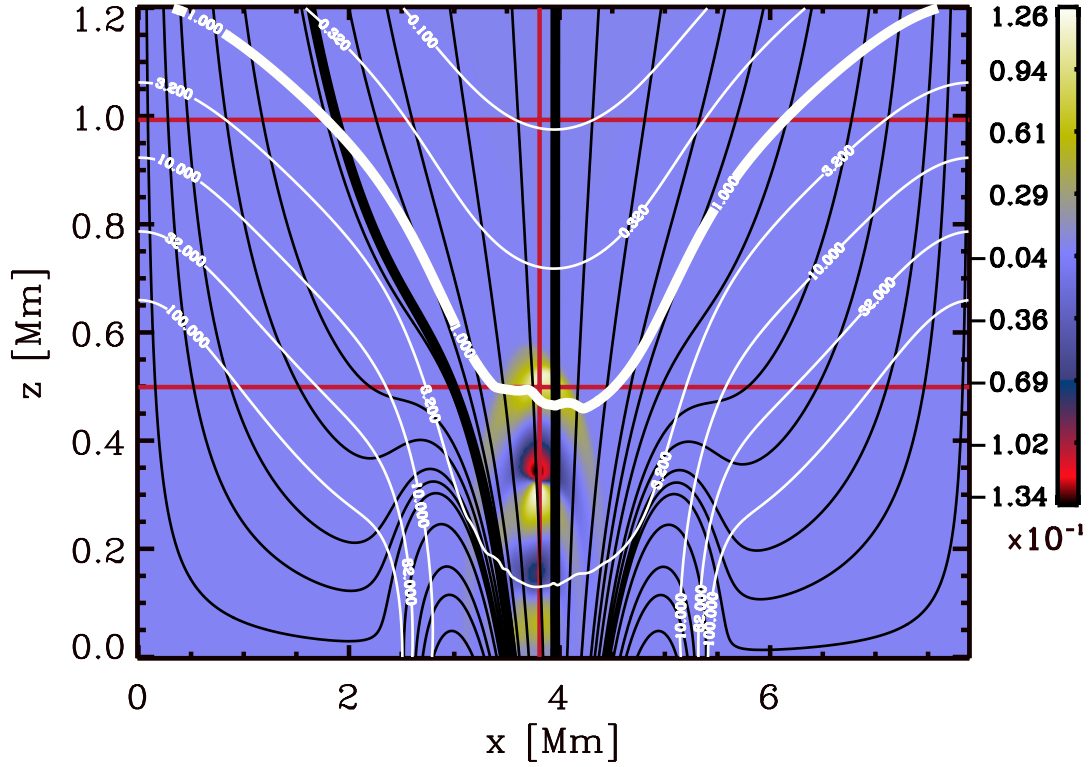


FIG. 10.—Rendering of  $u_{\parallel}(x, z)/c_0$  at an elapsed time of  $t = 58.5$  s, for radial driving in the weakly magnetized atmosphere (§ 3.2). The format is similar to Figs. 2, 6, and 7 and corresponds to the *same* elapsed time as Figs. 2 and 7. The  $\beta = 1$  magnetic canopy does not intersect the photosphere, but the selected magnetic lines of force (*thin black lines*) have the same shape and distribution as in the strongly magnetized atmosphere. We see here a nested sequence of horseshoes provided by the high- $\beta$  fast MAG wave. The legs of the horseshoes persist all the way down to the photosphere but are significantly weakened relative to the apex because of an unfavorable orientation of the fluid displacement relative to the magnetic field.

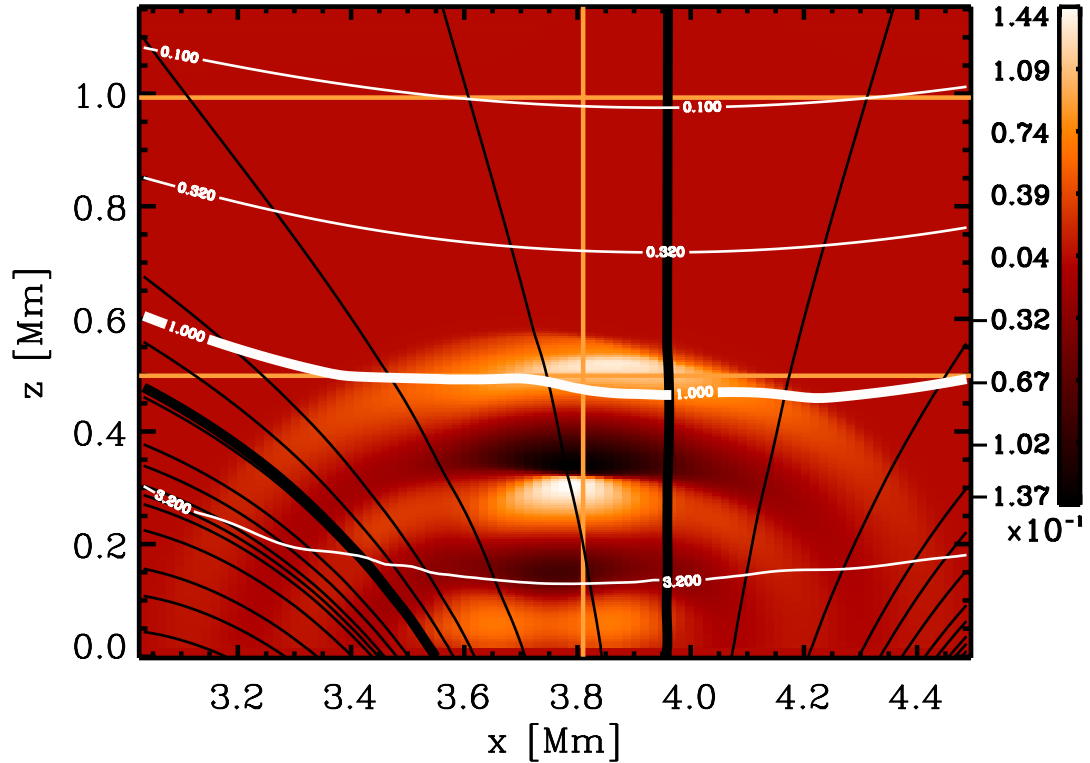


FIG. 11.—Fractional density fluctuations,  $\Delta\rho(x, z)/\rho_0(z)$ , corresponding to the field-aligned velocity image of Fig. 10. Only a portion of the computational domain is displayed to present a realistic aspect ratio. Here we see that the wave fronts are actually nested ellipses, not horseshoes. Iso- $\beta$  contours are still in white, and selected magnetic field lines are overplotted in black. The uniformity of the wave fronts is more evident here. Unlike in Fig. 3, where the magnetic field is strong, the fast waves generated by the piston propagate away in all directions and are unaffected by the field.



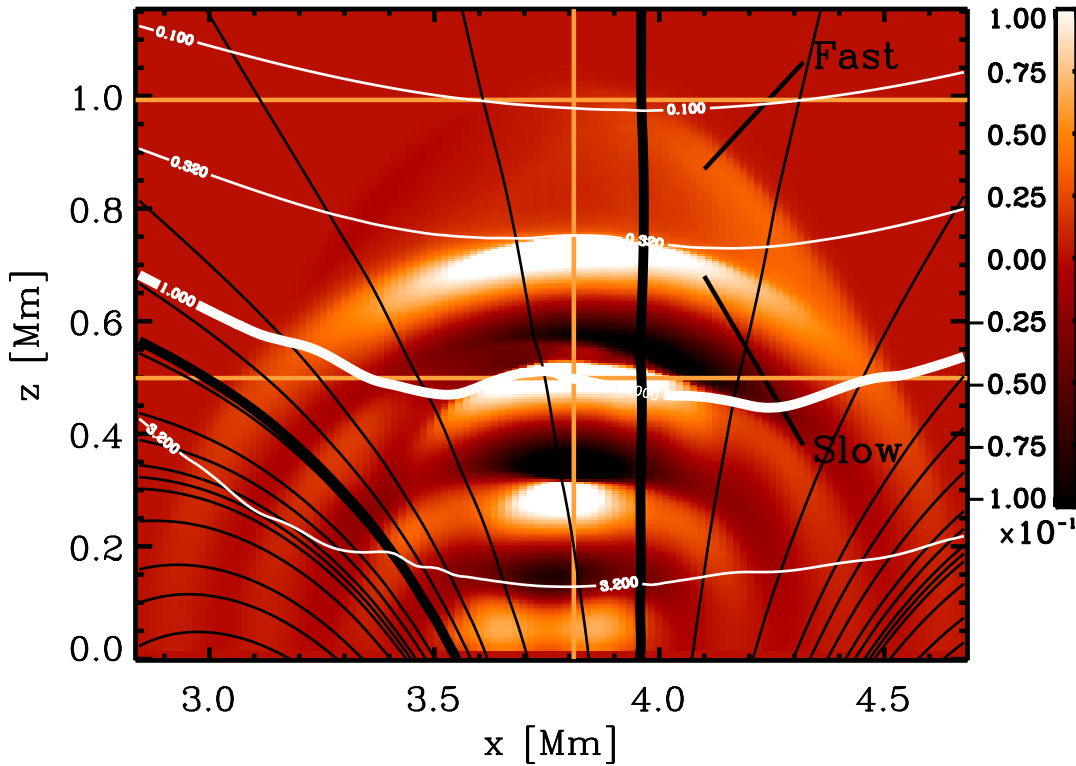


FIG. 12.—Continuation of Fig. 11 at  $t = 81.9$  s. The field of view is enlarged relative to the previous figure, and it no longer provides a realistic aspect ratio. The high- $\beta$  fast-wave train is converted into both fast and slow waves as it passes upward and through the magnetic canopy. To bring out the weak density fluctuations of the fast wave, the color table has been truncated at  $\pm 0.1$ , saturating the peak slow-wave values ( $+0.165$  and  $-0.138$ ). Note that the fast-wave front is asymmetric about its apex (density enhancements are on the right, and depletions are on the left), while the slow-wave fronts are symmetric.

With Figure 10 we display  $u_{\parallel}(x, z, t)/c_0$  at an elapsed time of  $t = 58.5$  s. The obvious differences with Figure 2 are (1) that the wave fronts extend beyond the magnetic flux directly connected to the driving piston, (2) the shape of the fronts, and (3) the variation of  $u_{\parallel}$  along the fronts. Some of these distinctions are physically based, while others occur because motions aligned with the magnetic field are not the optimal diagnostic for a wave that is basically insensitive to the field.

Figure 11 presents a different view at the same elapsed time. It shows the density fluctuations  $\Delta\rho/\rho_0$  in a restricted portion of the domain. As with Figure 3, the horizontal-to-vertical aspect ratio is realistic for this figure (although the two figures depict different regions). The nested wave fronts confirm that the fast wave propagates more or less isotropically away from the piston. Along a given front, the density fluctuations increase with altitude. This is again indicative of the constancy of the (linear) wave energy density<sup>16</sup>  $E_{\text{wave}}$  (eq. [6]) and the nonlinear steepening of the waves. While the latter operates along the entire front, the former is more pronounced just over the driving piston.

Closer inspection of this figure, however, reveals certain obvious anisotropies that are worth a few comments. Specifically, one notes that the most pronounced density enhancements and depletions occur in a somewhat restricted region intercepted by the fiducial  $x = 3.81$  Mm line. The extent of the largest density enhancements and

depletions is noticeably smaller than the lateral extent of the piston, and further, these regions have a tendency to drift gradually to the right with increasing altitude. A related feature is the slight indentation of the wave front at the apex of the orange-white density enhancement zones. This occurs below the magnetic canopy, before the wave conversion comes into play.

The physical explanation of these odd behaviors traces back to the driving piston: as the piston moves up into the atmosphere, flows in the positive (*right*) and negative (*left*)  $x$ -direction are created at the sharp edges of the piston. The material is not only lifted up by the piston but is also moved sideways and out of the way of the impermeable face of the advancing piston. On the following downstroke, there is a sideways inflow of material, reversing the sense of the  $u_x$  component. The net effect is rather like having a small virtual *transverse* piston operating at each edge of the single mechanical piston. These pistons are  $180^\circ$  out of phase and thus act as an extended dipole source of waves. The peak-to-peak  $u_x/c_0$  levels associated with each of the components of the dipole is approximately 0.03 at the edges of the main piston. This is not inconsequential when compared with the 0.047 value for the imposed  $u_z/c_0$  at the piston face. The slight anisotropies of the wave fronts visible in Figure 11 are thus created by the additional low- $\beta$  fast-wave sources at the piston edges.<sup>17</sup>

<sup>16</sup> The internal energy, the adiabatic condition, and the isothermal stratification all combine to yield  $\Delta p \sim \Delta\rho \sim (p_0)^{1/2} \sim (\rho_0)^{1/2}$ . Thus,  $\Delta\rho/\rho_0 \propto \rho_0^{-1/2}$ .

<sup>17</sup> In the strong-field calculation, the magnetic field is so stiff that it effectively inhibits any inflow or outflow at the edges of the piston. The virtual transverse piston sources do not operate when the piston is situated in a low- $\beta$  plasma.

A number of studies treat the multidimensional propagation of acoustic-gravity waves in an unmagnetized isothermal atmosphere, for example, Kato (1966) and Bodo et al. (2000). Their findings are all directly applicable to the high- $\beta$  region, where the magnetic field has no dynamic influence. However, the new aspect presented by the magnetosphere is the eventual interaction of the expanding fast-wave fronts with the  $\beta = 1$  magnetic canopy. This occurs first directly over the right edge of the piston. In Figure 11, the leading edge of the wave train has just crossed and has slightly distorted the magnetic canopy.

Figure 12 shows the density fluctuations at a later time ( $t = 81.9$  s). One sees that the transmitted fluctuations consist of both slow and fast waves. The low- $\beta$  slow waves have been discussed in § 3.1.1. They are compressive acoustic waves aligned with and guided along the magnetic field. A rather seamless transition between the incident high- $\beta$  fast wave and the transmitted low- $\beta$  slow wave results from the good alignment between  $\mathbf{B}$  and  $\nabla\beta$  along the bottom of the canopy.

The transmitted fast-wave front lies above the slow wave. In density it is asymmetric about its apex: density enhancements appear along the right half of the front and depletions appear on the left. As seen in motions perpendicular to the magnetic field,  $u_{\perp}(x, z, t)/c_0$ , the whole front moves to the right or to the left in unison (Fig. 13). The subsequent behavior of the low- $\beta$  fast wave after it has been launched from the magnetic canopy follows the outline of § 3.1.2, and those remarks apply here without modification.

What is novel about the present situation is that the fast waves accelerate past and continually overrun the steady upward march of the slow waves. A very interesting interference pattern develops in space and time. This pattern, indeed its very existence, depends critically on the independent variable in question. For example, a comparison of Figures 12 and 13 shows that there is no interference in motions transverse to the magnetic field since the transmitted low- $\beta$  slow wave cannot contribute. In density fluctuations and in motion parallel to the magnetic field, the interference is present to varying degrees.

Figure 14 presents a plot of altitude versus time for density fluctuations at  $x = 3.81$  Mm. The format is entirely analogous to that used in Figure 4 for the strong-field simulation. The low- $\beta$  fast wave emerges smoothly from the magnetic canopy and accelerates away from the transmitted low- $\beta$  slow wave, which follows the linear sonic trajectory. A detailed comparison of Figures 4 and 14, on the other hand, shows that the low- $\beta$  slow waves reach the top of the plots (both at an altitude of 1.2 Mm) at the same time, independent of the field strength and the presence of the magnetic canopy! From this, one gathers that there is little phase delay in the conversion of a high- $\beta$  fast wave to a low- $\beta$  slow wave across the canopy.

The complementary display (see Fig. 5) is here provided by Figure 15. Below the canopy there is qualitative agreement between the strong- and weak-field cases in both density and in field-aligned motions. The principal cause of the similarity is the serendipitous alignment between the

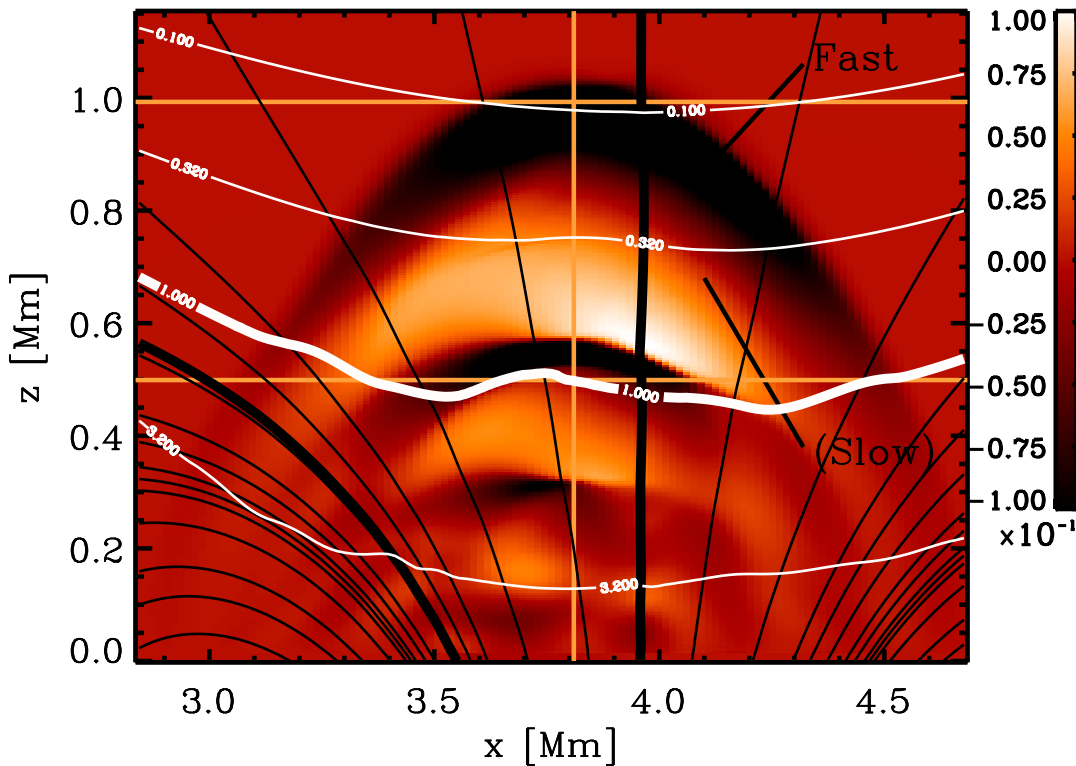


FIG. 13.—Identical to Fig. 12, except presenting  $u_{\perp}(x, z)/c_0$ . The scale is again truncated at intermediate values, but here it is done to bring out the extensions of the fronts across the magnetic canopy and back into the high- $\beta$  plasma. The low- $\beta$  slow wave is essentially absent from this image. It is only indirectly visible in the deformation of the  $\beta = 0.32$  contour. The “fast” and “slow” labels are in the same positions as in Fig. 12; however, parentheses have been placed around the “slow” label, since there is no signature of the slow wave in this image. In the neighborhood of the magnetic field line that connects to the left side of the photospheric piston there are additional closely packed wave fronts due to high- $\beta$  slow waves created by horizontal motions confined to the left edge of the piston.

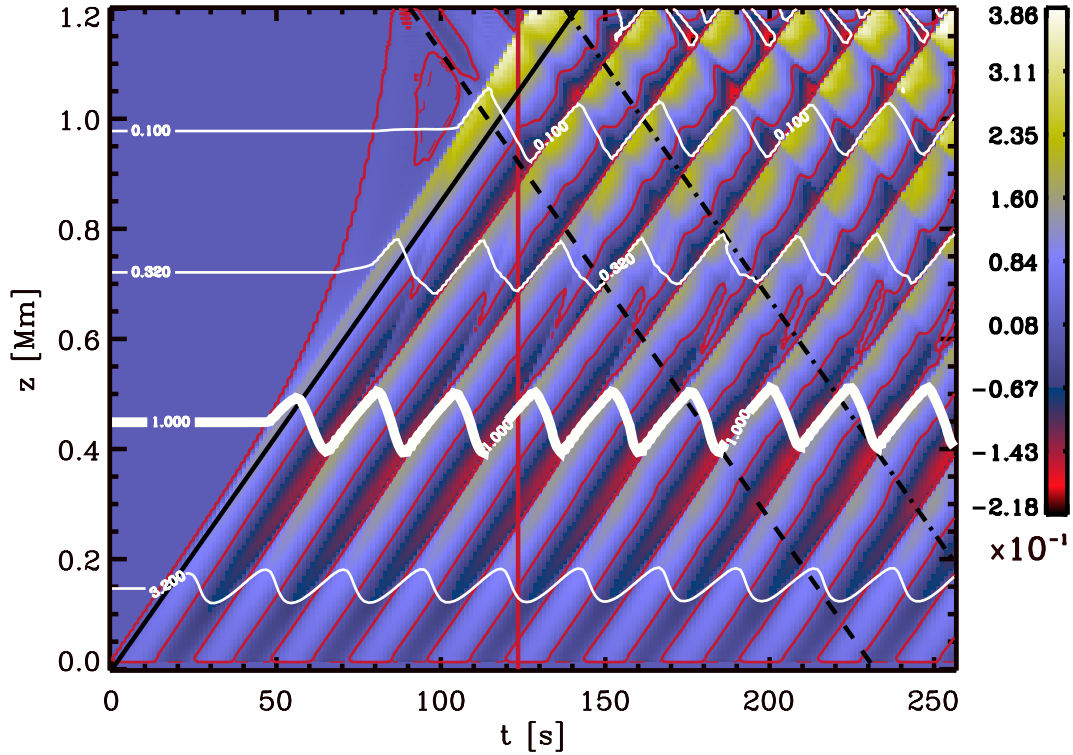


FIG. 14.—Altitude vs. time plot of the density fluctuations  $\Delta\rho(z, t)/\rho_0(z)$  at  $x = 3.81$  Mm in a format analogous to that of Fig. 4, *except* for the numerical simulation of radial driving in a *weak* magnetic field (§ 3.2). The black lines are sonic trajectories (using  $c_0 = 8.49$  km s<sup>-1</sup>) for direct (*solid line*) and reflected (*broken line*) waves. The white lines show the altitude variations of selected iso- $\beta$  surfaces with time. Two thin red contour lines corresponding to  $\Delta\rho(z, t)/\rho_0(z)$  of  $\pm 0.01$  (*solid line*: positive sign; *broken line*: negative sign) are added to bring out the fast wave. The fast-wave fronts curve up from the canopy because of the rapid increase of the Alfvén velocity with altitude. Fast and slow waves reflect back into the computational domain from the upper boundary and produce a regular interference pattern to the right of the broken black lines.

wavevector and the magnetic field lines. The envelopes for the parallel Mach number (*heavy dashed black lines in lower panel*) are  $u_{\parallel}/c \sim \rho_0^{-1/2}$  and  $u_{\parallel}/c \sim -\rho_0^{-3/5}$ . The growth is faster in the first 300 km of the atmosphere than that found in Figure 5 for the strong-field simulations.<sup>18</sup> Above this altitude the amplitudes level off as the fast wave senses the magnetic canopy. The steepening of the waveform continues through the mode conversion zone.

Above the magnetic canopy, the continuation of the N-wave has suffered a modest decrease in amplitude, consistent with the transfer of energy to the low- $\beta$  fast waves. The transmitted fast wave can just be discerned in the instantaneous density profile presented in Figure 15 (*top*). This is best achieved by correlating the slight density anomalies with the pronounced downturn in the  $u_{\perp}/c$  profile shown in Figure 15 (*bottom*). Figure 15 (*bottom*) indicates a phase flip occurs between  $u_{\parallel}$  and  $u_{\perp}$  as the wave train enters the  $\beta \approx 1$  mixing zone. Above (and after) this flip, which in effect signifies the birth of the fast wave, the two motions decouple and go their separate ways in the overlying low- $\beta$  plasma. Although the fast and slow waves decouple as they emerge from the canopy, they carry definite phase relations imprinted by their joint creation from the incoming high- $\beta$  fast wave. Spatial interference patterns thus develop above the canopy. For example, one observes a periodic modula-

tion of the envelope of the fractional density fluctuations in Figure 15 (*top*).

One additional curiosity worth comment concerns the odd behavior of the perpendicular Mach number in Figure 13 (*bottom left*). The wave fronts nearly double in number in crossing the thick magnetic line of force that marks the left edge of the piston. The increase in the number of wave fronts in  $u_{\perp}/c_0$  does not have any counterpart in the density fluctuations. Although there are distortions in the positions of the compression and rarefaction zones, the correct number of zones for an elapsed time of  $t = 81.9$  s is in place in Figure 12.

The only means available to generate additional wave fronts is to create an additional wave variety. The high- $\beta$  slow wave is the only option. Since it propagates at the Alfvén velocity, its superposition on the high- $\beta$  fast waves naturally leads to doubling the visible wave fronts. Transverse high- $\beta$  slow waves contribute to  $u_{\perp}$  but *not* to  $\Delta\rho$ , and this nicely avoids the creation of unwanted additional wave fronts in the density fluctuations. The source of the high- $\beta$  slow waves is the virtual transverse piston (with fluctuating  $u_x$ ) located at the left edge of the mechanical piston. The  $u_x$  motions drag the magnetic field lines back and forth, launching the transverse magnetic waves. These waves are guided along the magnetic field lines; therefore, the spatial localization of these disturbances along the flux affected by the left edge of the piston caps a satisfying explanation of all the outstanding features present in Figures 11–13.

<sup>18</sup> The likely cause is some additional constructive interference from the two virtual-piston wave sources on each edge of the main mechanical piston.

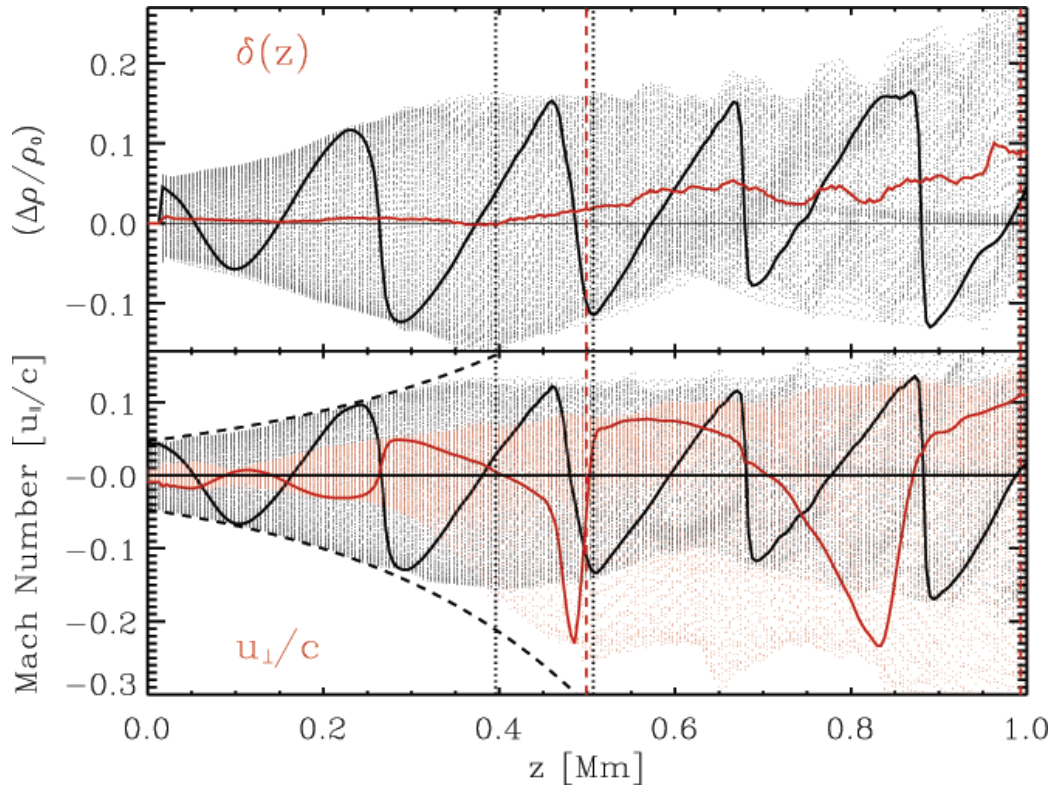


FIG. 15.—Fluctuations at the  $x = 3.81$  Mm location for radial driving in a weakly magnetized atmosphere (§ 3.2), presented in the same format as Fig. 5. The solid curves again pertain to the fixed time of  $t = 123.5$  s. Two vertical black dotted lines mark the greatest altitude excursions of the  $\beta = 1$  magnetic canopy. The transformation of the perpendicular Mach number through the mode conversion zone shows a  $180^\circ$  phase shift relative to the smooth continuation of the parallel Mach number. The envelope of the parallel Mach number can be fitted with simple exponentials with characteristic  $e$ -folding lengths of 316 km ( $2 H_\rho$ ) on the positive side and 263 km [ $(5/3) H_\rho$ ] on the negative side.

### 3.2.2. More Mode Conversion

The apex of the transmitted low- $\beta$  fast waves accelerates upward and passes out of the field of view as time progresses beyond the snapshot presented in Figure 13. As we noted previously, the wave front develops a teardrop shape and the legs are refracted around and advance on the magnetic canopy *from above*. One expects a basic replay of the sequence of events described in § 3.1.2: the legs of the fast-wave fronts sweep around and impinge with their wavevectors aligned with the normal to the magnetic canopy.

Figures 16 and 17 document this second mode conversion episode. In Figure 16 we show the velocity perpendicular to the magnetic field at the same time ( $t = 123.5$  s) and in the same format as Figure 3. The anticipated change in orientation of the broad, low- $\beta$ , fast-wave fronts is quite evident, especially in the upper left corner of the plot. As the fronts cross the magnetic canopy, they weaken dramatically in strength, and they also appear to terminate or even break into distinct substructures. The process is difficult to follow in this figure but is better seen in Figure 17, where we overplot additional contours to bring out the weak features.

Figure 17 shows an enlarged field of view at a much later time ( $t = 156$  s). It is now apparent that the region below the magnetic canopy is subjected to rather complex interference phenomena. One identifies the high- $\beta$  fast-wave fronts created directly by the piston passing through the same variety of MAG waves generated by the mode conversion at the magnetic canopy. The latter, of course, trace their origin to the incident low- $\beta$  fast waves. Although these two fast-wave

trains interfere at the same place and time, it is fascinating to ponder the potential implications of the very different routes they each took in arriving at this point. The direct fast-wave train also impinges on the magnetic canopy (*from below*) and must likewise undergo mode conversion by transmission and reflection. The significant disparity in the strengths of the direct and converted waves, however, makes it quite difficult to observe.

### 3.3. Weak-Field and Transverse Driving

As the transverse shaking of magnetic flux concentrations is often invoked as a means for conveying energy into the solar atmosphere, we shall now look at the third of our four numerical simulations, wherein the driving piston oscillates in the  $x$ -direction instead of the  $z$ -direction. To maintain as much uniformity as possible, we keep the transverse motions sinusoidal in time with a period of 23.8 s and retain a peak amplitude of  $u_x = 400$  m s $^{-1}$ . All other attributes remain precisely as in § 3.2.

#### 3.3.1. High- $\beta$ Slow Wave

The transverse motions of the piston are ideal for launching high- $\beta$  slow waves. This MAG wave has a quasi-Alfvénic character: the principal motions are transverse to the magnetic field, with little in the way of noticeable density fluctuations or field-aligned displacements. The magnetic tension associated with the deformation of the magnetic fields lines is the basic restoring force, so the linear version



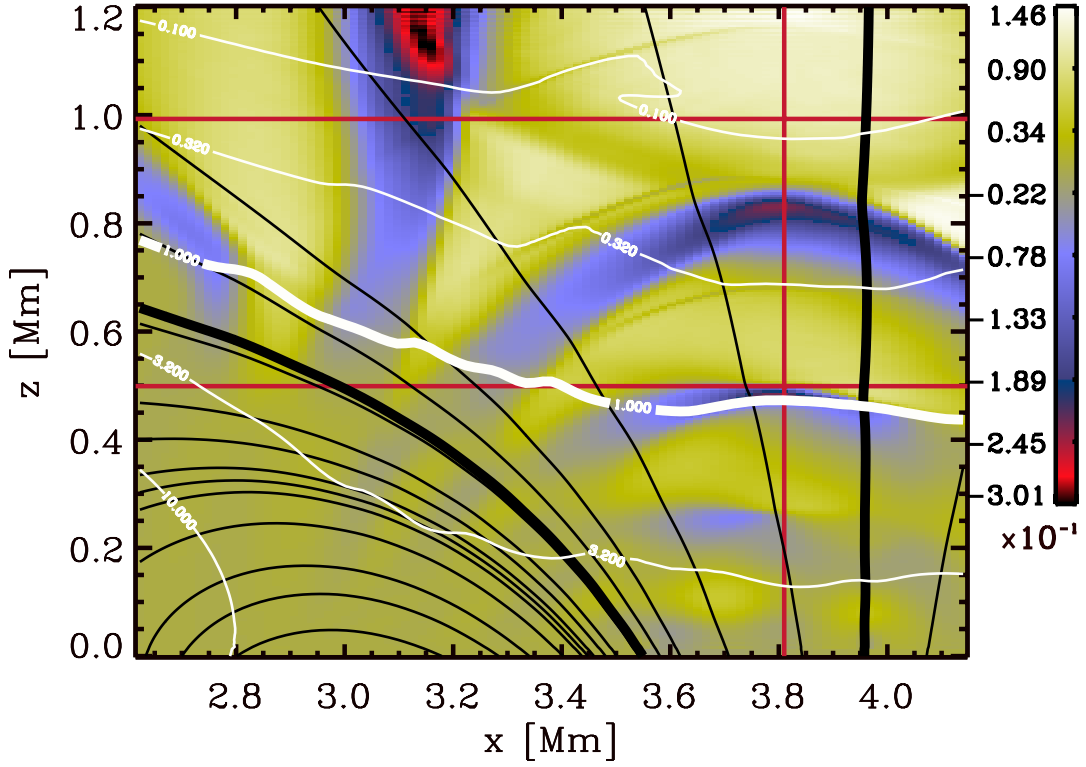


FIG. 16.—Enlargement of  $u_{\perp}(x, z)/c(x, z)$  at an elapsed time of  $t = 123.5$  s, for radial driving in a weakly magnetized atmosphere (§ 3.2). The spatial aspect ratio is accurate for this image, which is largely dominated by the fast MAG wave. In the low- $\beta$  region one notes how the wave fronts appear to sweep in a counterclockwise sense about a pivot point in the general vicinity of  $x = 3.1$  Mm and  $z = 400$  km. The large concave-upward structure in yellow, lying just below the reference  $z = 993$  km altitude, is a wave front reflected back from the upper boundary of the simulation (at  $z = 1.26$  Mm).

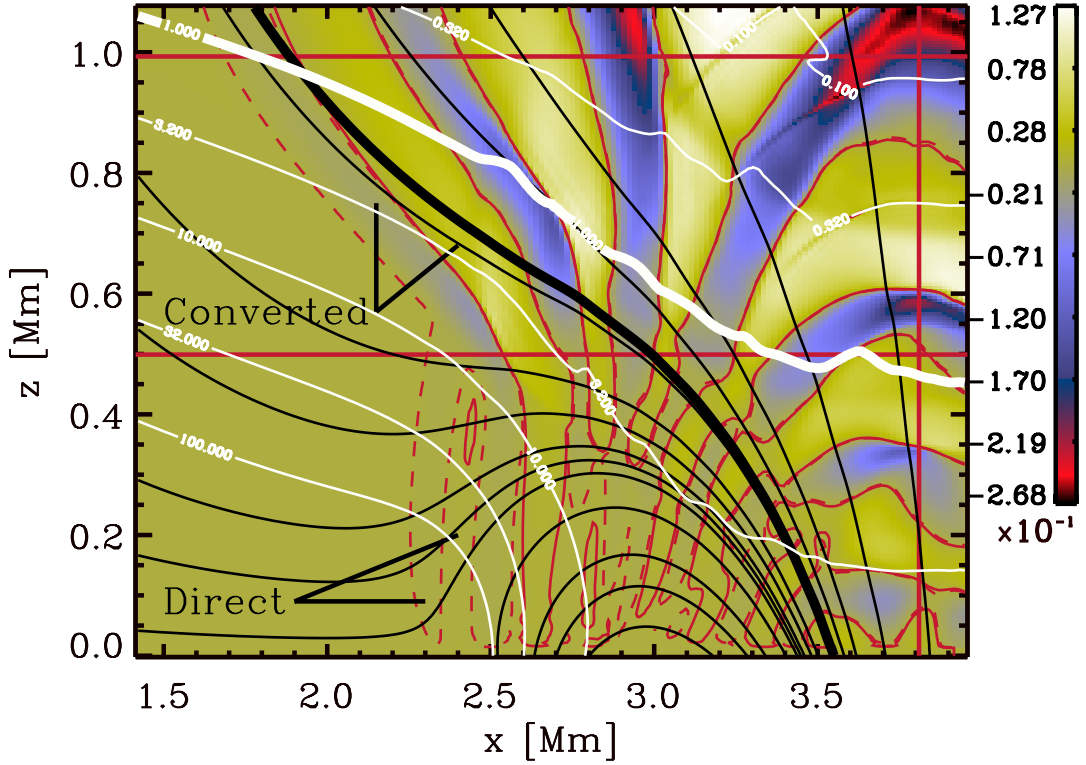


FIG. 17.—Further development of the counterclockwise rotation of the low- $\beta$  fast-wave fronts of Fig. 16 as recorded in  $u_{\perp}(x, z)/c(x, z)$ , at the elapsed time  $t = 156$  s. Two additional red contours at  $\pm 0.001$  bring out the weak high- $\beta$  fast wave, which travels parallel to the photospheric boundary. This wave train comes directly from the driving piston and has not yet interacted with the magnetic canopy. The direct fast-wave fronts merge and interfere with the low- $\beta$  fast wave in a transition layer bounded by the canopy (from above) and the magnetic field line connected to the left side of the piston (from below).

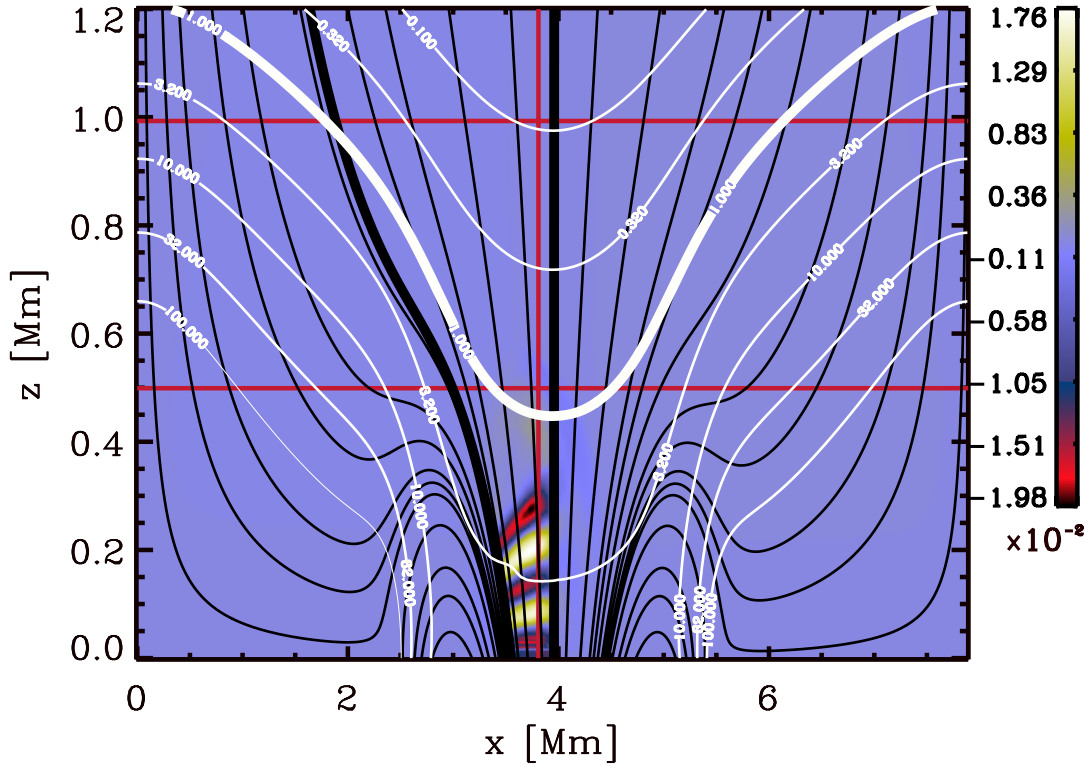


FIG. 18.—Rendering of  $u_{\perp}(x, z)/c_0$  at an elapsed time  $t = 58.5$  s, for *transverse* driving in a weakly magnetized atmosphere (§ 3.3). The format is identical to that previously employed in Figs. 2, 6, 7, and 10. One sees principally the high- $\beta$  slow wave with transverse oscillations to the right (*red*; positive  $u_{\perp}$  and negative  $u_{\perp}$ ) and left (*yellow*). This wave train is confined to the piston-connected magnetic flux and propagates along the field at the Alfvén velocity. A faint halo of color surrounding the slow-wave train is produced by fast MAG waves that are also emitted by the oscillating piston.

of this wave is guided along the magnetic field lines at the local Alfvén velocity.<sup>19</sup>

Figure 18 shows the motions perpendicular to the magnetic field ( $u_{\perp}$ ) in a format analogous to Figures 2 and 7. The elapsed time is again 58.5 s, so we see two layers of motion to the left (*yellow*) sandwiched between three zones of fluid moving to the right (*red*). The slow wave is confined to the magnetic flux that connects directly to the driving piston at the photosphere. One may also discern the slight increase of the wavelength with altitude. This is consistent with the increase of the Alfvén velocity in the direction of the magnetic canopy. The variation of the Alfvén velocity across the magnetic lines of force connected to the driving piston causes the right side of the wave front to outrun the left side. Given sufficient distance this would lead to phase mixing, but in the present example the magnetic canopy is encountered well before this phenomenon becomes a relevant factor.

Closer inspection of this figure reveals a diffuse faint yellow region around the intersection of the magnetic canopy with the  $x = 3.81$  Mm marker. A similar area of blue lies to the right of the piston-connected magnetic flux. These two structures are signatures of high- $\beta$  fast waves that are generated near the right edge of the piston. The lateral motion of the piston creates alternate compressions and rarefactions as its right and left edges move and interact with the ambient

plasma. This creates two localized sources for fast waves on either side of the piston. The sources are of course  $180^\circ$  out of phase (when the right edge compresses, the left rarefies, etc.), so the transverse piston is a dipole source of fast waves, in addition to a monopole source of slow waves.<sup>20</sup>

Further consideration of this figure suggests an unanticipated puzzle with regard to the wave amplitude. Transverse motions of  $400 \text{ m s}^{-1}$  at the driving piston would yield an expected Mach number of 0.047, but the peak-to-peak velocity of the slow-wave train is too small by a factor of  $\frac{1}{3}$ . A detailed investigation of the region around the driving piston shows the existence of a thin numerical boundary layer, approximately 5–7 zones in extent (i.e., 20–30 km), where the transverse velocity amplitude drops exponentially from  $400 \text{ m s}^{-1}$  to approximately  $125 \text{ m s}^{-1}$ , accompanied by zone-to-zone oscillations in sign. This is a purely numerical artifact somewhat akin to a thin viscous boundary layer. The numerical “clutch” between the piston and the neighboring magnetized plasma is in some sense only partially engaged. The slip between the driver and the atmosphere is not a serious problem because our interest is in the behavior of the waves *after* they are launched into the magneto-atmosphere. When we compare the four numerical simulations (§ 4), we shall be able to compensate for this effect by simply scaling the wave amplitudes up by a factor of  $\approx 3$  for the transverse piston examples.

<sup>19</sup> This MAG wave was previously encountered in § 3.1.2 and Figs. 8 and 9. There it was produced through mode transformation at the magnetic canopy.

<sup>20</sup> When it is embedded in a high- $\beta$  region. The opposite association of a generated wave with the multipole order of the source occurs when the transverse piston is in a low- $\beta$  region!



### 3.3.2. Even More Mode Conversions

The upward-propagating high- $\beta$  slow wave is guided along the magnetic lines of force directly into the overlying  $\beta \approx 1$  layer. From this interaction, transmitted fast and slow waves emerge and propagate into the overlying low- $\beta$  atmosphere. The process is illustrated in Figures 19 and 20. These two figures follow the realistic aspect ratio format of Figures 3, 11, and 16.

In Figure 19 we display the transverse velocity  $u_{\perp}$  at  $t = 123.5$  s. There is a smooth transition from the high- $\beta$  slow wave to the low- $\beta$  fast wave, accompanied by a rapid increase in wavelength and propagation speed in passing across the magnetic canopy. The wave train arrives at the canopy dominated by transverse motions and exits with the same basic character.

Figure 20 shows the field-aligned motions  $u_{\parallel}$  in the same format. Below the magnetic canopy, the slow-wave train is delineated by both field-aligned and transverse motions. Where the  $\beta$  is greatest, the transverse motions enjoy their greatest domination over the field-aligned motions. Over most of the region, the  $\beta$ -values are fairly moderate; therefore, the limiting  $\beta \rightarrow \infty$  behavior of the slow wave, i.e., purely transverse oscillations, is not quite in force. Above the magnetic canopy the two orthogonal velocities go their separate ways as they decouple and propagate away as distinct wave modes.

A fascinating consequence of mode coupling across the magnetic canopy in this particular simulation is the phenomenon of wave front splitting. Below the reference altitude of  $z = 499$  km and the solid black magnetic field line marking the left edge of the piston-connected flux, one

observes that the  $u_{\perp}$  and  $u_{\parallel}$  wave fronts are virtually identical. Within the piston-connected flux, the correspondence is qualitatively the same *below* the magnetic canopy, but the congruence vanishes above the canopy.

Another means to view the mode conversion across the canopy is to consider the fluctuations along the reference location  $x = 3.81$  Mm within the dominant magnetic flux concentration. Figures 21 and 22 provide these data in the usual formats employed for the previous two simulations. To maintain a thread of uniformity with the previous plots of this type, we focus on the relative density fluctuations in Figure 21. Density is not a particularly useful diagnostic for the present simulation: the high- $\beta$  slow wave only modulates the specific volume of the plasma because  $\beta$  is not large, and thermodynamic fluctuations are not the strong suit of the low- $\beta$  fast wave. The two additional red contour lines at the  $\pm 0.0005$  level are critical to bring out the necessary details.

First, the most prominent density fluctuations actually reside *above* the magnetic canopy in the guise of the transmitted low- $\beta$  slow waves. A naive set of observations of intensity (i.e., density) fluctuations would necessarily give the impression of waves spontaneously emanating upward from the  $z \approx 400$  km altitude, with no visible link to photospheric activity!<sup>21</sup> The slanting black lines mark several

<sup>21</sup> To be precise, temperature rather than density fluctuations are the best proxy for intensity fluctuations. However, in the present circumstances, in which the entropy of the displaced fluid element remains constant, density and temperature fluctuations are equivalent.

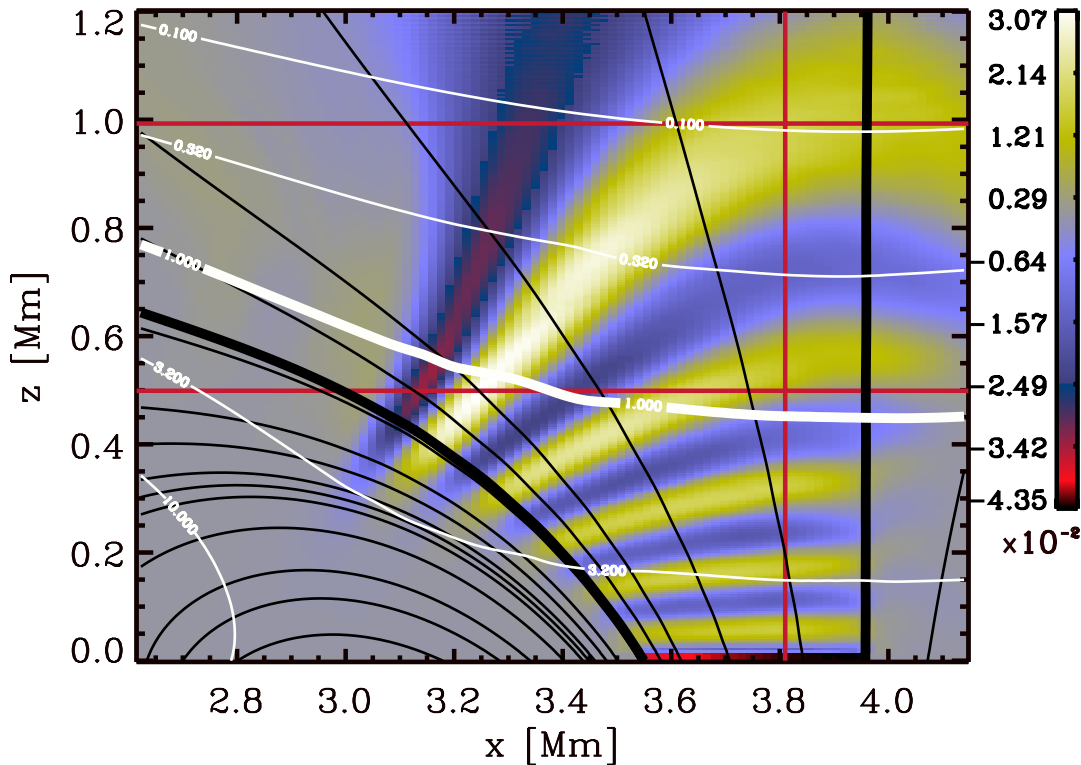


FIG. 19.—Enlargement of a portion of Fig. 18 at  $t = 123.5$  s. The format and aspect ratio are identical to that employed in Fig. 16. We see a smooth transition across the canopy from the high- $\beta$  slow wave to the low- $\beta$  fast wave, followed by the counterclockwise rotation of the transmitted fast-wave fronts as previously observed in Figs. 16 and 17.

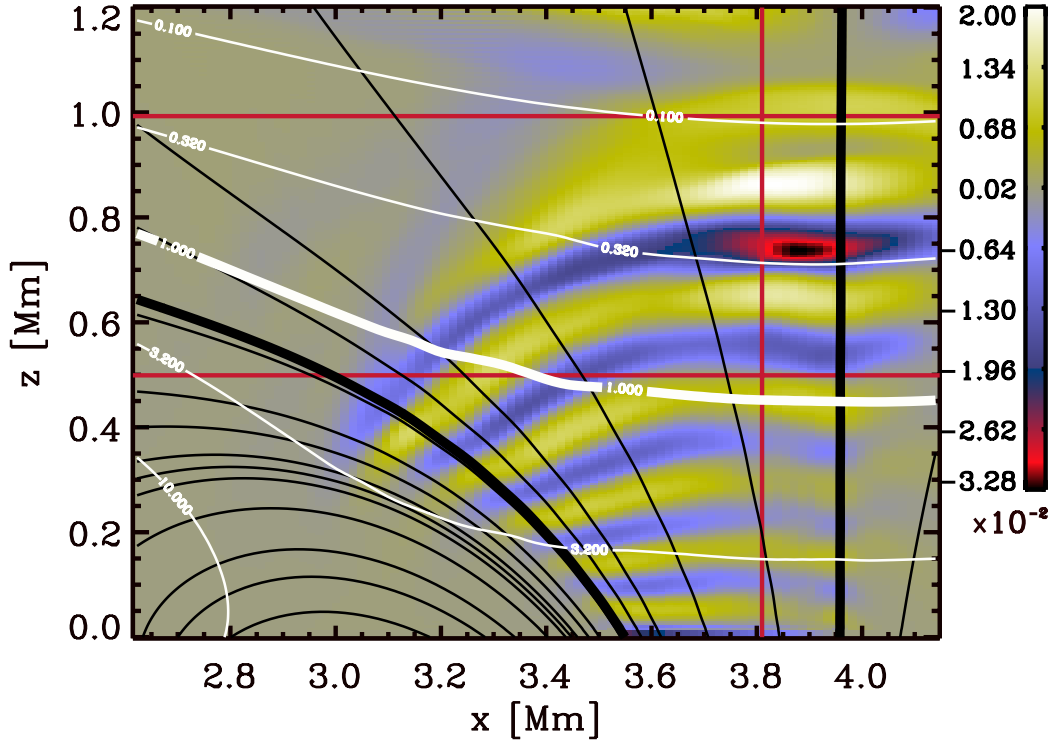


FIG. 20.—Identical to Fig. 19 in every respect *except* presenting  $u_{\parallel}(x, z)/c(x, z)$  instead of  $u_{\perp}(x, z)/c(x, z)$ . Below the canopy the high- $\beta$  slow waves are again visible. But this image shows that they also convert smoothly to low- $\beta$  slow waves as they pass through the canopy. The motions parallel to the magnetic field are comparable in magnitude to those that are perpendicular to the field (see Fig. 19).

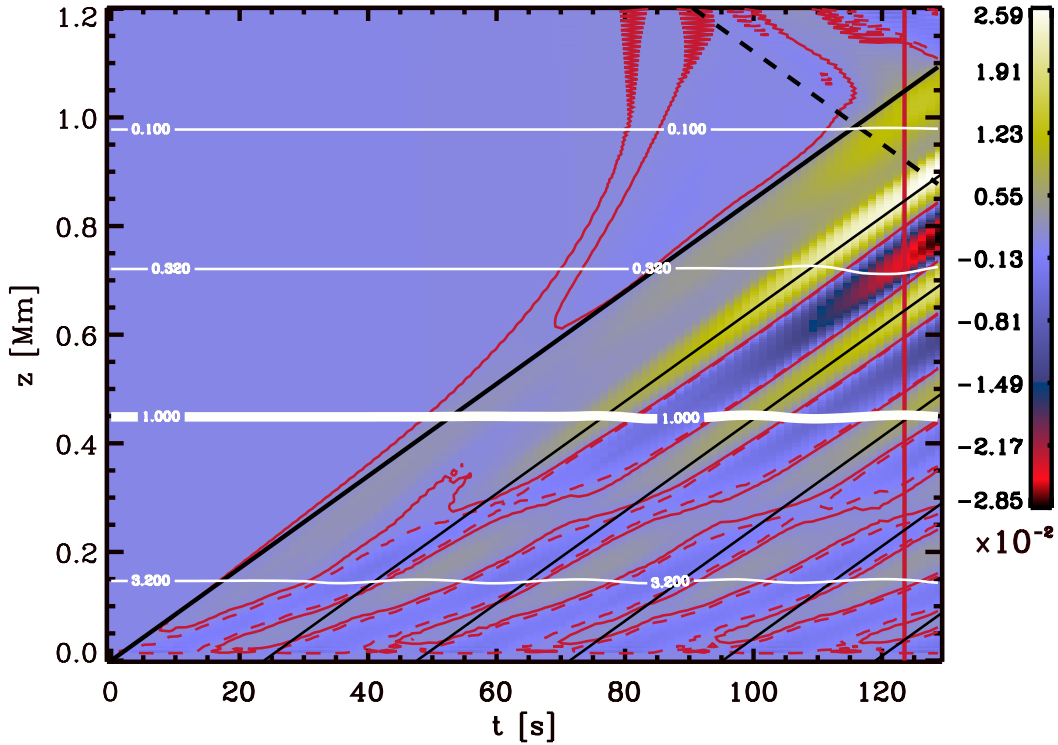


FIG. 21.—Altitude vs. time rendering of  $\Delta\rho(z, t)/\rho_0(z)$  at  $x = 3.81$  Mm, for *transverse* driving in a *weak* magnetic field (§ 3.3). The format is the same as that used in Figs. 4 and 14. The additional red contour levels are at  $\pm 0.005$ . The thick black lines are sonic trajectories (using  $c_0 = 8.49$  km s $^{-1}$ ) for direct (*solid lines*) and reflected (*dashed line*) waves. The additional thin black lines are simply displaced in time by one wave period (i.e., 23.8 s). Above the canopy we mainly observe the low- $\beta$  slow waves propagating at the sound speed; the added red contours are necessary to bring out the fast wave. Below the canopy there is a fairly balanced mixture of fast and slow waves when viewed *in density fluctuations*. The slow waves curve upward slightly as they propagate away from the photosphere and into layers of increasing Alfvén velocity, but above the  $\beta = 3.2$  contour, interference between fast and slow waves leads to a peculiar pattern. It is interesting to note that the largest density (or intensity) fluctuations appear *above* the canopy.

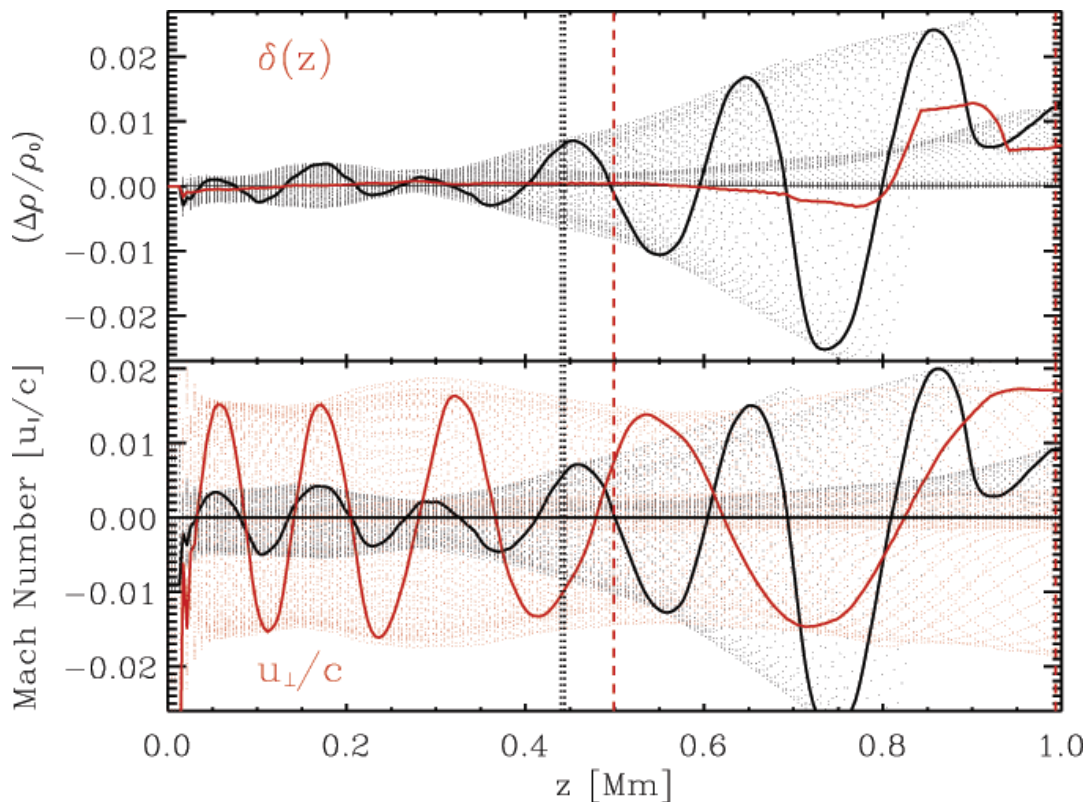


FIG. 22.—Fluctuations at the  $x = 3.81$  Mm location for transverse driving in a weakly magnetized atmosphere (§ 3.3), presented in the same format as Figs. 5 and 15. The excursions of the canopy, as illustrated by the two black dotted lines nearly on top of each other, are minimal. The exponential growth of density fluctuations and field-aligned motions above the magnetic canopy, through the auspices of the low- $\beta$  slow wave, is the most obvious feature. There is negligible lifting of the atmosphere since  $\delta(z) \approx 0$ .

trajectories of uniform vertical motion at  $c_0 = 8.49 \text{ km s}^{-1}$ . They allow one to deduce that the transverse piston is a parsimonious source of high- $\beta$  fast waves. This corroborates our interpretation of the faint yellow and blue structures ahead of the slow-wave train in Figure 18 as fast waves. Thanks to the two red contours, the density fluctuations associated with the high- $\beta$  slow wave are easy to pick out in the first 300 km of the atmosphere. These structures begin with an upward curvature consistent with the increase of the Alfvén velocity with altitude, but then they appear to flatten (i.e., slow dramatically) around  $z \approx 300$  km before they accelerate back up to the sound speed as they cross the canopy. The slanting black lines permit one to identify this apparent deceleration and subsequent acceleration as an illusion created by the interference of the fast and slow waves. The superposition of the two waves gives the impression that the upward-propagating slow-wave density enhancement stalls around 300 km to proceed onward with a later fast wave emitted from the piston. What is really taking place is the coalescence of an early slow wave with a later fast wave just below the canopy and the transmission of a strong low- $\beta$  slow wave on the upper side of the canopy! Finally, the thin isthmus of positive density enhancement that breaks off from the first sonic trajectory at  $t \approx 65$  s and  $z \approx 600$  km and accelerates toward the upper boundary of the simulation is a very weak low- $\beta$  fast wave.

Figure 22 shows the density fluctuations and the fluid motions in a format identical to that of Figures 5 and 15. At each altitude fewer points are plotted than in the other two figures, reflecting the shorter duration of the transverse driv-

ing simulation. The instantaneous snapshot is at the same elapsed time of  $t = 123.5$  s (Fig. 21, vertical red line). It documents the general dominance of the transverse motions relative to the field-aligned motions in the high- $\beta$  plasma (a ratio of approximately 3 : 1) and also the gradual increase of the wavelength with increasing altitude and Alfvén velocity. As the wave train passes through the magnetic canopy, the field-aligned and transverse motions change their character. The transverse Mach number decreases slightly in amplitude and rapidly increases its wavelength with height above the canopy, following the fast speed. The parallel Mach number exhibits an exponential increase in amplitude while maintaining a constant wavelength. These properties derive naturally from the behavior of a field-aligned acoustic wave in an isothermal atmosphere. The steepening of the wave profile toward an N-wave is also evident, although the process has not had sufficient time to achieve its limiting form. As expected, sensible density fluctuations accompany the birth and upward progression of the low- $\beta$  slow wave.

Perhaps the final point to appreciate in comparing Figures 14 and 21 (or equivalently Figs. 15 and 22) is the difference in the vertical excursions of the magnetic canopy. The impinging slow wave is ineffective in raising and lowering the altitude of this layer either directly (by imparting momentum in the vertical direction) or indirectly (by compressing and rarefying the fluid). This is reflected in the order-of-magnitude disparity in the zero offset of the density fluctuations,  $\delta(z)$ , obtained for the two driving polarizations. In fact, the  $\delta(z)$  presented in Figure 22 is not significantly different from zero.

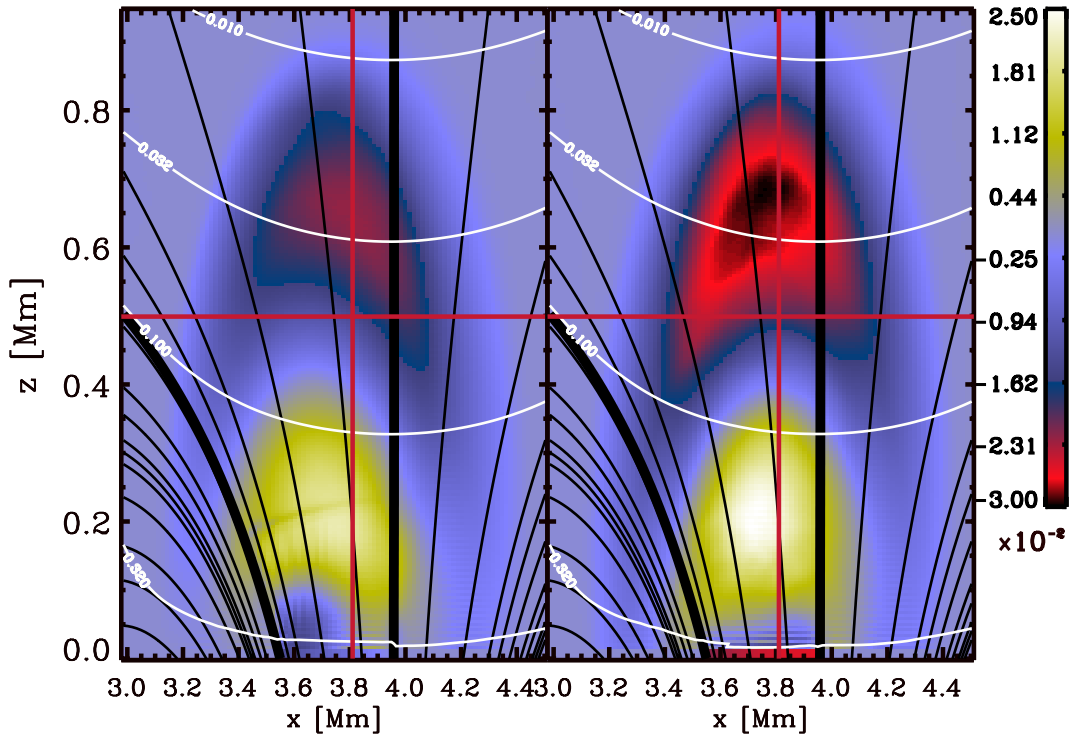


FIG. 23.—Side-by-side snapshots of  $u_{\perp}(x, z)/c_0$  at an elapsed time of  $t = 26$  s. *Left*, Simulation of radial driving in a strong magnetic field (§ 3.1); *right*, the transverse driving in a strong magnetic field (§ 3.4). Each panel shows the same region of the computational domain, but with the instantaneous  $\beta$ -contours (white lines) and selected magnetic field lines (solid black lines) appropriate for that simulation. The color table is the same for both panels but is optimal only for the left panel. This comparison shows that low- $\beta$  fast waves are effectively generated independently of the polarization of the driving piston.

### 3.4. Strong-Field and Transverse Driving

To complete our suite of numerical simulations, we retain the transverse piston motion of the previous section (§ 3.3) but increase the magnetic field strength by a factor of 4 to return to the initial magneto-atmosphere employed in § 3.1. The piston is once again located entirely within the low- $\beta$  plasma, which dips downward to the photosphere within the dominant magnetic flux concentration.

The lateral undulations of the piston generate a mixture of fast and slow waves, with the former more prevalent than in the vertical driving discussed in § 3.1. The numerical “clutch” is again only partially engaged. The result is smaller amplitudes for the emitted fast and slow waves than would be expected from the prescribed piston amplitude. This problem can again be rectified by a suitable renormalization when we compare the different simulations in the next sections.

After the rather lengthy and detailed discussions of the first three numerical simulations, it is fortunate that there is relatively little new in this numerical experiment that was not treated in the other three. Outside of a different balance between the ratio of fast to slow waves produced by the two piston polarizations, the wave evolution and transformations are essentially the same as in § 3.1. Figures 23 and 24 provide side-by-side views of the strong-field magneto-atmosphere with radial and transverse driving. From these comparison plots, one finds the emitted fast waves are very nearly indistinguishable in morphology. The slow waves, which are guided along the magnetic field lines, show rather different spatial variations. These can be attributed to nuances of the driving piston orientations. For example, in Figure 24 (*right*) the slow waves extend beyond the magnetic

flux directly connected to the piston. The explanation is the alternating compression and rarefaction zones that are necessarily present on the edges (and neighboring environs) of the transverse piston but are absent from the piston with vertical motion.

### 4. ENERGY TRANSPORT VERSUS CIRCULATION

In the previous section we provided an extended discussion of the morphological development and behavior of MAG waves in the four sample numerical simulations. Particular emphasis was placed on the transformation and mode mixing that occurs if and when the piston-generated waves encounter the  $\beta \approx 1$  magnetic canopy. From a practical perspective, one would like to assign definite energy fluxes to the individual wave varieties and to describe how these fluxes transform and are deposited in the magneto-atmosphere. A potential resolution of the chromospheric and coronal heating problem in terms of wave damping and dissipation naturally hinges on such an exercise.

We would be remiss if we did not address this issue. But it must be stated at the outset that the definitive treatment would require that the *simulation* determines the wave heating of the background atmosphere in a manner consistent with the governing primitive equations (Carlsson & Stein 1992, 1995, 1997, 2002). Any effort that circumvents this approach, such as our strict conservation of specific entropy, is necessarily subject to valid criticisms, and it also relies on certain assumptions that may be of dubious merit. In the present circumstances, we shall see that one may readily determine the energy flux at any desired point in the magneto-atmosphere (see, e.g., Figs. 25–27). Knowledge of this



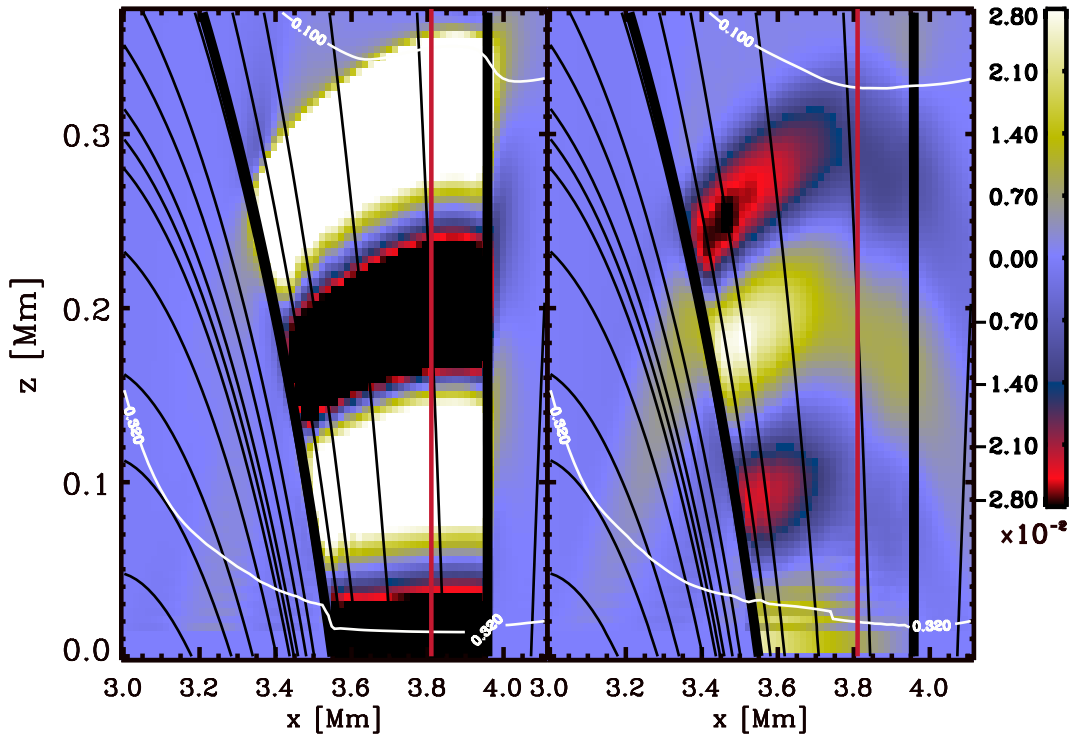


FIG. 24.—Analogous to Fig. 23 except displaying  $u_{\parallel}(x, z)/c_0$  at a later elapsed time,  $t = 40.3$  s. *Right*, Transverse driving simulation; *left*, radial driving. Both panels again make use of the same color table, but the disparity in the amplitude of the field-aligned motions saturates the image in the left. The radial piston functions efficiently as a monopole slow-wave source, whereas the transverse piston yields only a very weak admixture of of monopole and dipole. In both panels, however, the magnetic field is important for structuring and guiding the waves.

quantity in and of itself is not, however, sufficient to gauge the effectiveness of atmospheric heating by MAG waves.

The four calculations, when viewed as a whole rather than individually as in § 3, provide additional critical insights on MAG waves propagating within a nontrivial potential magnetic field. The driving pistons all have a common size (a width of 400 km), location, ( $3.55 \text{ Mm} \geq x \geq 3.95 \text{ Mm}$ ), oscillation frequency (42.9 mHz), and velocity amplitude ( $400 \text{ m s}^{-1}$ ). The distinctions between the four examples are whether the piston motion is along the  $z$ -direction (radial driving) or  $x$ -direction (transverse driving) and whether the piston resides in a high- or low- $\beta$  plasma. The relative efficiency of the four simulations can be properly assessed since all four magneto-atmospheres contain a low- $\beta$  top layer. The extent and degree of magnetic domination in this top layer are of course different between the strong- and weak-field cases, but one at the very least enjoys the advantage of comparing the *same* low- $\beta$  fast and slow waves in each of the simulations. In view of the mode mixing across the canopy, this is a critical prerequisite for any sensible intercomparison.

Throughout the many figures used to illustrate the discussion in § 3, we have employed red or orange lines to mark the locations of two reference altitudes at  $z = 499$  and  $993$  km, and one reference spatial location within the dominant magnetic flux concentration and the driving piston at  $x = 3.81 \text{ Mm}$ . In Figures 25–27 we provide computed energy fluxes measured along these three cuts through our four  $x$ - $z$ - $t$  data cubes. We determine the energy flux from two different prescriptions: the “wave” energy flux  $F_{\text{wave}}$  (Bray & Loughhead 1974), based on equation (10), and the exact energy flux derived from the nonlinear MHD equations,  $F$ . In ideal MHD, the exact *nonlinear* specifications for the

energy density and energy flux are

$$E = \frac{1}{2} \rho |u|^2 + \frac{p}{\gamma - 1} + \rho g z + \frac{1}{8\pi} |B|^2, \quad (13)$$

$$F = u \left( \frac{1}{2} \rho |u|^2 + \frac{\gamma p}{\gamma - 1} + \rho g z + \frac{1}{4\pi} |B|^2 \right) - B \left( \frac{1}{4\pi} u \cdot B \right), \quad (14)$$

with the requisite condition

$$\frac{\partial E}{\partial t} + \nabla \cdot F = 0. \quad (15)$$

The perfect gas equation of state is employed, but otherwise these results generally apply to any magneto-atmosphere.

While there is no controversy over the validity of the exact representations stated above, they convey certain interpretive liabilities that shall soon become evident. To appreciate this point we begin by plotting in *black* the measured distribution of  $F_z$  at the reference location  $x = 3.81 \text{ Mm}$  in Figure 25, that is, at a position over the driving piston and near the right edge of the magnetic flux connected directly to the piston. Each panel corresponds to one of the four simulations, and the arrangement of the numerical calculations follows the layout of Table 3. The energy flux is measured in multiples of  $10^{10} \text{ ergs cm}^{-2} \text{ s}^{-1}$ . In keeping with the precedent adopted in Figures 5, 15, and 22, we display the instantaneous distributions of  $F_z$  versus altitude at the elapsed time of 123.5 s by using the continuous thick black curves. These snapshots are useful not only for relating to the earlier figures but also for illustrating how the distribution of recorded values of  $F_z$  are built up with the passage of time and the upward progress of the wave train.

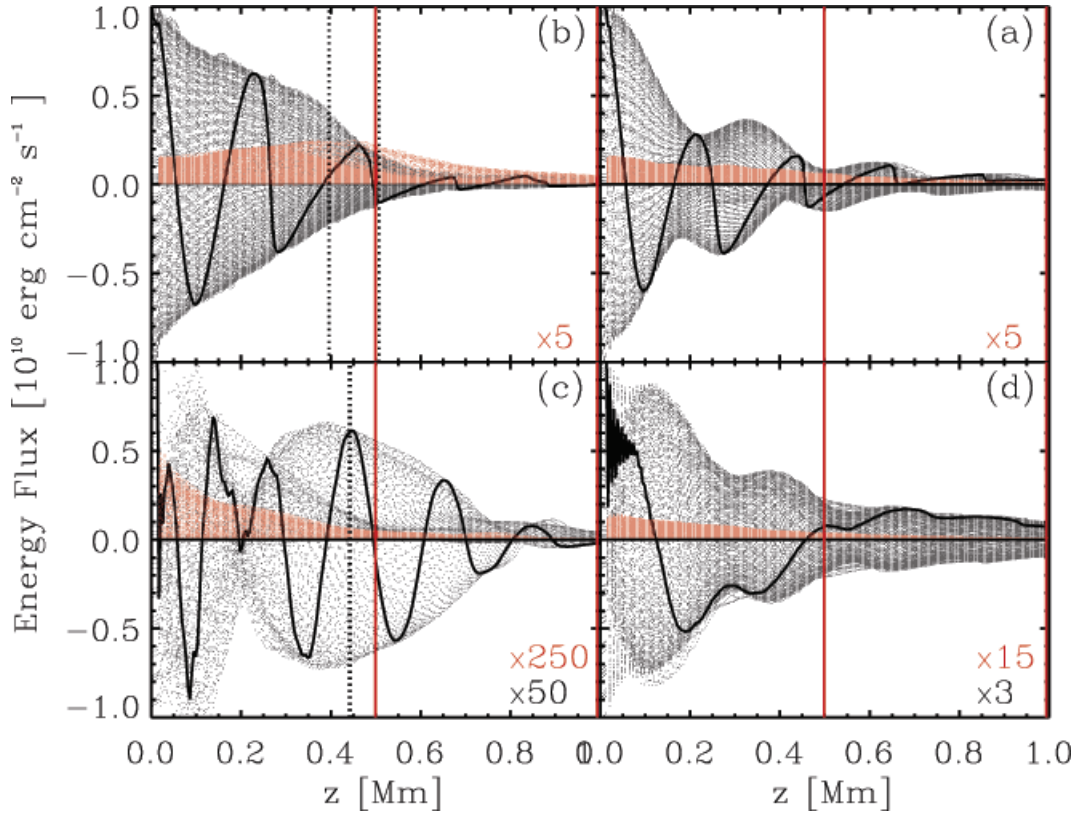


FIG. 25.—Component in the  $z$ -direction of the exact energy flux  $F$  (eq. [14]; black) and the “wave” energy flux  $F_{\text{wave}}$  (eq. [10]; red), as recorded at  $x = 3.81$  Mm. Each panel represents one of the four numerical simulations: (a) radial driving and strong field (§ 3.1), (b) radial driving and weak field (§ 3.2), (c) transverse driving and weak field (§ 3.3), and (d) transverse driving and strong field (§ 3.4). For these data to share the same ordinate scale, different enhancement factors are necessary for each quantity. For example, in (c) the plotted  $F_z$  values are 50 times larger than their actual values, while in (b) the actual  $F_z$  values are plotted, but the plotted  $z$ -components of the wave energy flux are a factor of 5 larger than the measured values. The vertical dotted black lines show the maximal altitude excursions of the  $\beta = 1$  magnetic canopy. The heavy black curves show the instantaneous profiles of  $F_z$  at an elapsed time of  $t = 123.5$  s. The wave energy flux is positive almost everywhere and declines only modestly with altitude. The exact energy flux is much larger, fairly uniformly distributed over positive and negative values, and declines rapidly with height. The former may represent the net transport of energy by the MAG waves, whereas the latter derives from a stationary energy circulation pattern.

Figure 25 (bottom) emphasizes the weak numerical coupling of the transverse piston to the MAG waves. On average, the energy flux drops by 2 orders of magnitude between the bottom and top of the computational domain. It is of course highly oscillatory in time, taking on both positive and negative values. However, as the the distribution of black dots attests, there is a very slight tendency to favor positive (upward directed) over negative (downward directed) fluxes.

To place this up-down flux asymmetry on a quantitative footing, it would be necessary to average these data over many oscillation periods. A cursory visual inspection of Figure 25 suggests that the average positive tendency of  $F_z$  is on the order of perhaps 5%–10% of the peak fluctuations at each altitude. For the radial-driving simulations (Fig. 25, top), this would translate into a sustained positive energy flux above  $z = 1$  Mm of a few times  $10^8$  ergs  $\text{cm}^{-2} \text{s}^{-1}$ . To substantiate this estimate by direct averaging would therefore require the analysis of a continuous time series comfortably in excess of 20–30 wave periods (i.e., 400–600 s of elapsed time). There is no principal difficulty in extending our simulations in time (see Table 2); however, the spurious wave reflection off the upper boundary would render the exercise entirely pointless.

The liability of the exact flux  $F$  is that it is dominated by a stationary but still oscillatory flow of energy that is essen-

tially local or circulatory in character and does not contribute to the net (long distance) transport of energy from the piston to the initially quiescent plasma far from the wave source. The wave flux,  $F_{\text{wave}}$ , on the other hand, is designed to capture the transfer of energy by wavelike disturbances, but it suffers from the drawback that it enjoys no unique nor widely agreed-on derivation (Bray & Loughhead 1974; Leroy & Schwartz 1982; Leroy 1985). The expression given by equation (10) is just one of (infinitely) many possible choices for the pair  $(E_{\text{wave}}, F_{\text{wave}})$  that satisfy the conservation law equation (9). Setting this issue aside for the moment, if we simply plot the distribution of  $\hat{z} \cdot F_{\text{wave}}$  recorded at  $x = 3.81$  Mm by using red dots in Figure 25, we find that the wave energy flux (1) is smaller by a factor of 5–20 than the exact energy flux, (2) is strongly skewed toward positive (upward directed) values,<sup>22</sup> and (3) declines rather modestly with increasing altitude.<sup>23</sup> These three properties are consistent with the intuitive visual average of the numerous black dots on each panel. One is tempted to think that

<sup>22</sup> This tendency can be physically rationalized for the low- $\beta$  slow wave, e.g., by noting that the plasma is compressed ( $\Delta p \geq 0$ ) in upflows ( $u_z \geq 0$ ) and rarefacted ( $\Delta p \leq 0$ ) in downflows ( $u_z \leq 0$ ); see Fig. 5. Thus,  $u_z \Delta p$  is positive-definite throughout the slow-wave train.

<sup>23</sup> The modest decrease of  $u_z \Delta p$  with altitude is also “consistent” with the linear wave scalings  $u \sim \rho_0^{-1/2}$  and  $\Delta p \sim \rho_0^{+1/2}$ .



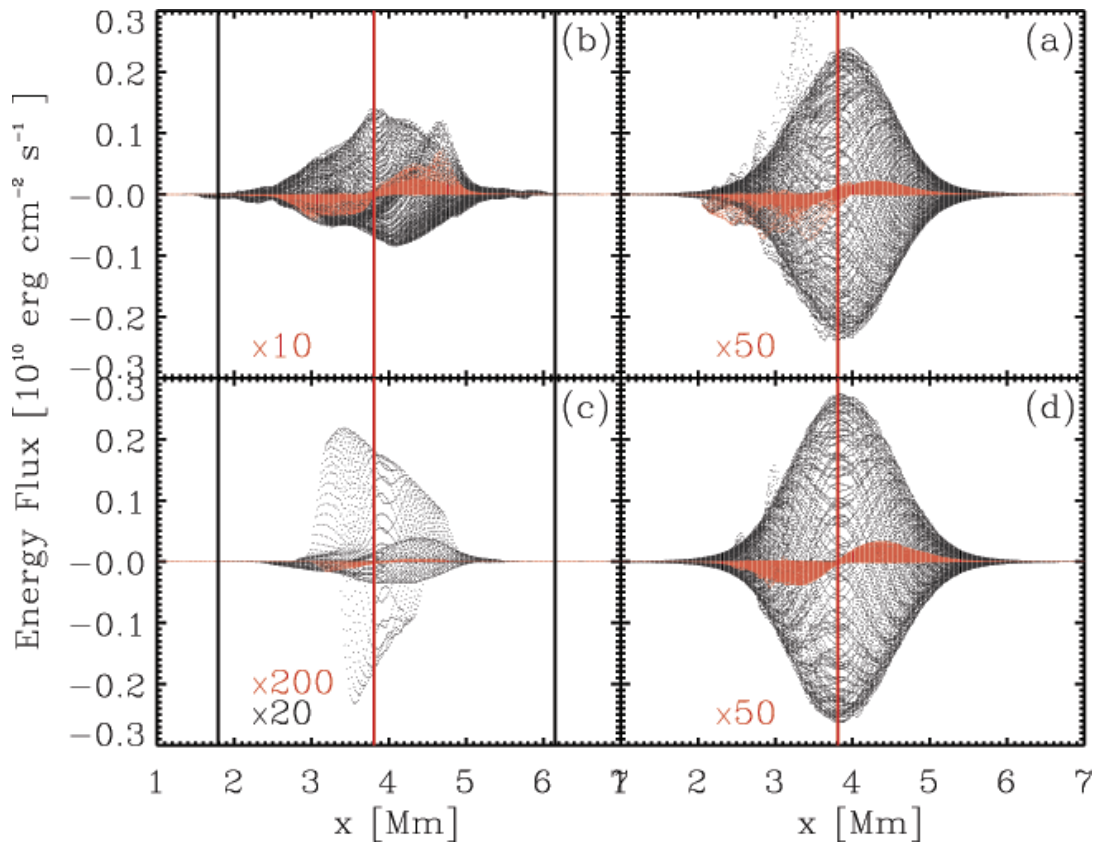


FIG. 26.—Component in the  $x$ -direction of the exact energy flux  $F$  (eq. [14]; black) and the “wave” energy flux  $F_{\text{wave}}$  (eq. [10]; red), as recorded at the reference altitude  $z = 993$  km. Each panel represents one of the four numerical simulations: (a) radial driving and strong field (§ 3.1), (b) radial driving and weak field (§ 3.2), (c) transverse driving and weak field (§ 3.3), and (d) transverse driving and strong field (§ 3.4). For these data to share the same ordinate scale, different enhancement factors are necessary for each plotted quantity. For example, in (c) the plotted  $F_x$  values are 20 times larger than their actual values, while in (b) the actual  $F_x$  values are plotted, but the plotted  $x$ -components of the wave energy flux are a factor of 10 larger than the actual values. The vertical black lines show the maximal lateral excursions of the  $\beta = 1$  magnetic canopy. In (b) and (c) these lateral excursions are not particularly large, so the four lines appear as two thick lines. Consistent with the interpretation advanced for Fig. 25, the exact wave flux is dominated by a stationary energy circulation pattern. The wave flux describes the net transport of energy away from the atmosphere that overlies the driving piston.

the expression for the wave energy flux has successfully separated the net energy transport from the larger local circulation, but it might well be inadvisable to read anything further into this (serendipitous?) result.

Figures 26 and 27 provide a complementary view of the energy flux in the two reference atmospheric layers, but with  $F_x$  and  $\hat{x} \cdot F_{\text{wave}}$  displayed in lieu of the vertical fluxes. The data plotted in black ( $F_x$ ) are again dominated by local energy circulation through these atmospheric layers; the data shown in red ( $\hat{x} \cdot F_{\text{wave}}$ ) are much reduced in magnitude and show a pronounced left-right asymmetry consistent with one’s expectation of energy flowing laterally away from the plasma located over the piston. There is considerably more structure in these horizontal slices, especially at the lower altitude, than in the vertical slices presented in Figure 25. The interference between the fast- and slow-wave trains is ultimately the cause of this added complication.

The relative contributions of the fast and slow waves to the energy flux are determined from additional detailed information that is not available in Figure 25–27. Since the fast wave always arrives at a fixed altitude before the slow wave, it is possible to associate separate energy fluxes with each wave variety. For the slow wave, this necessarily requires the subtraction of a background fast-wave flux level, which is invariably present. To permit intercompari-

sons between the four calculations, we restrict our attention to the upper reference layer at  $z = 993$  km (Fig. 26), which resides in the low- $\beta$  top layer. Table 5 records the outcome of these estimates. Although only the  $x$ -components of the energy fluxes are displayed in Figure 26, the numbers in Table 5 use *both* the  $x$ - and  $z$ -components added in quadrature. It is worth adding that the information provided in this table is derived from fairly rough estimates, which probably have an overall precision no better than 20%–40%. Their accuracy may well be a factor of 2–4 worse.

A number of interesting conclusions may be drawn from Table 5. The circulatory energy flux, as determined by  $F$ , resides for the most part in the fast wave. This makes physical sense since the magnetic energy density is the dominant contribution to  $E$  in the low- $\beta$  plasma, and the slow wave does not perturb the magnetic field. With the exception of transverse driving in the weak field, all simulations circulate comparable amounts of energy flux ( $\approx 2 \times 10^9$  ergs  $\text{cm}^{-2} \text{s}^{-1}$ ) at an altitude of  $z \approx 1$  Mm. Transverse driving in the strong field creates the most energy circulation aloft despite the poor numerical coupling of the magneto-atmosphere to the piston. The transport of mechanical energy, as determined by  $F_{\text{wave}}$ , is preferentially allocated to the slow wave. The slow wave dominates the transport for radial driving in the strong field and for transverse driving in the weak field.

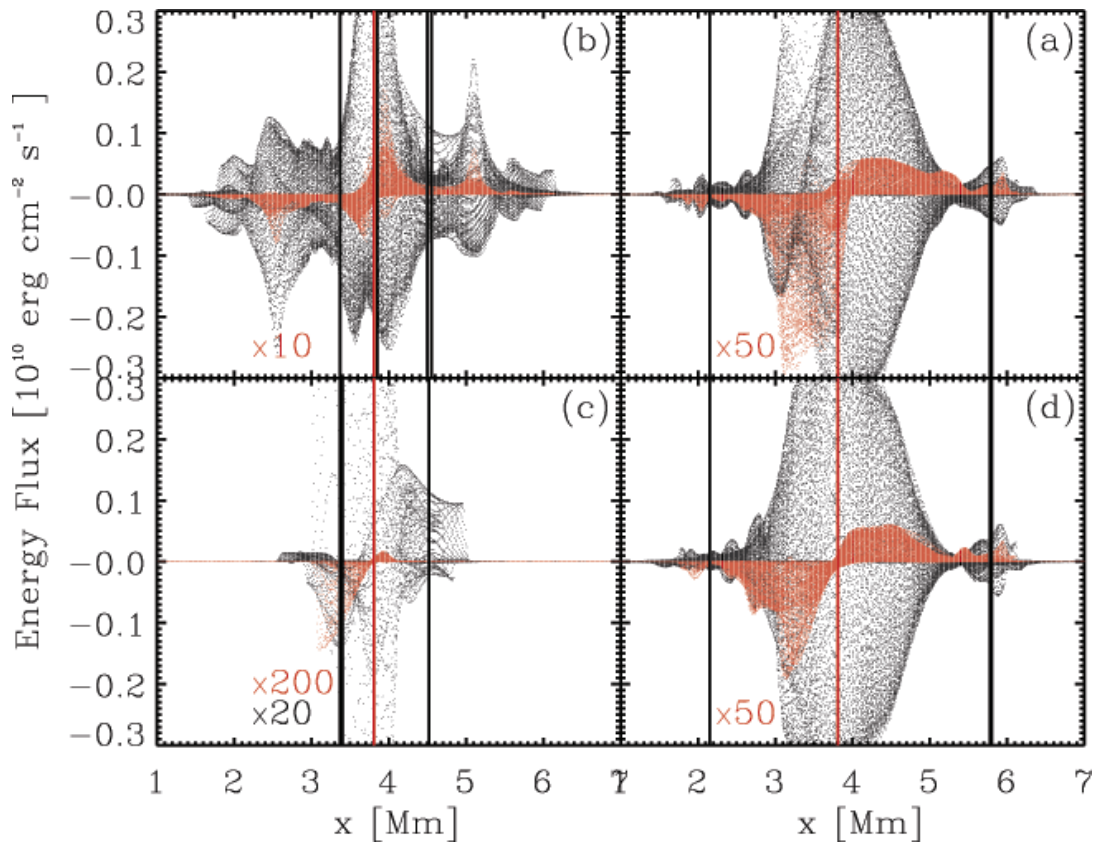


FIG. 27.—Identical to Fig. 26 in every sense except that the data pertain to the reference altitude  $z = 493$  km. Nearly all lateral excursions of the magnetic canopy are again so small that the four black vertical line segments appear as two thick lines, except for the left side of (b). There the greatest positive  $x$ -value reached by the magnetic canopy is in fact just to the right of the reference  $x = 3.81$  Mm line plotted in red. Wave transformations at the canopy are responsible for all the additional structure and variability found at this atmospheric level.

With the other two simulations there is a rough equipartition of energy transport between the fast wave and the slow wave. Finally, radial driving in the weak field transports the most energy at the 1 Mm atmospheric level ( $\approx 4 \times 10^7$  ergs  $\text{cm}^{-2} \text{s}^{-1}$ ), and transverse driving in the weak field generates the least ( $\approx 2 \times 10^4$  ergs  $\text{cm}^{-2} \text{s}^{-1}$ ).

The substructures present in Figures 25–27 can now be accounted for by utilizing the relative strengths of the fast and slow waves from Table 5. The periodic undulations of the  $F_z$  envelope with altitude that are present in Figure 25

(right) result from coherent interference between the upward-propagating fast and slow waves. The strength of the undulations are stronger in Figure 25a than in Figure 25d because the fast and slow waves are more evenly balanced in the former than they are in the latter. In Figure 26c, the dense “pancake” of black points is produced initially by the passage of the fast wave through the layer, and the more diffuse “halo” is created by the subsequent passage of the slow wave. The outlying positive black dots on the left sides of Figure 26a and Figure 26d in this figure are

TABLE 5  
FAST- AND SLOW-WAVE ENERGY FLUXES IN THE LOW- $\beta$  ATMOSPHERE

| Driving                       | Flux                | Weak Field, Fast Wave | Weak Field, Slow Wave | Strong Field, Fast Wave | Strong Field, Slow Wave |
|-------------------------------|---------------------|-----------------------|-----------------------|-------------------------|-------------------------|
| Radial.....                   | $ F $               | $1 \times 10^9$       | $4 \times 10^8$       | $2.4 \times 10^9$       | $2.1 \times 10^9$       |
| Radial.....                   | $ F_{\text{wave}} $ | $3.9 \times 10^7$     | $4.1 \times 10^7$     | $5 \times 10^6$         | $2.5 \times 10^7$       |
| Transverse <sup>a</sup> ..... | $ F $               | $2 \times 10^7$       | $1 \times 10^8$       | $2.7 \times 10^9$       | $8 \times 10^8$         |
| Transverse <sup>a</sup> ..... | $ F_{\text{wave}} $ | $2.2 \times 10^4$     | $7.6 \times 10^5$     | $8 \times 10^6$         | $4 \times 10^6$         |

NOTE.—All energy fluxes are measured in ergs  $\text{cm}^{-2} \text{s}^{-1}$  and record the peak energy flux magnitudes associated with each wave mode at an altitude of  $z = 993$  km over the entire duration of each of the four simulations. The fast waves always arrive first and are then followed by the slow waves. The energy fluxes attributed to the fast wave may therefore be determined without any ambiguity. The slow-wave flux is reckoned by taking the *difference* between the peak energy fluxes recorded during these two distinct epochs in which only fast waves and a combination of both slow and fast waves are present. The (exact) energy flux  $F$  and the “wave” energy flux  $F_{\text{wave}}$  are computed using eqs. (14) and (10), respectively.

<sup>a</sup> No corrections are applied for the poor numerical coupling between the transverse piston motions and the neighboring magneto-atmosphere noted in § 3.3.1. The  $u_x$  values imparted to the waves near the base of the computational domain are about a factor of 3 smaller than the imposed  $\pm 400$  m  $\text{s}^{-1}$  transverse piston velocity. The wave energy flux is quadratic in the fluctuations, while the exact energy flux is linear, at least to leading order. One might therefore try to place the transverse and radial driving simulations on an even footing by relative scalings of 9 and 3 between the two forms of the energy flux.

likewise produced by the steepened slow waves; the remainder of the symmetric distribution of points are therefore provided by the fast waves. Other nuances may be explained in a similar fashion. The difficulty of the exercise increases dramatically at the lower  $z = 493$  km altitude (Fig. 27), where it is necessary to deal with the juxtaposition of high- $\beta$  and low- $\beta$  atmospheric regions.

### 5. SOME SPECULATIONS ON SUNSPOT, INTERNETWORK, AND INTRANETWORK OSCILLATIONS

We may take advantage of these numerical simulations to develop some synthetic “observations” of oscillations in and about magnetic flux concentrations. In Figures 28 and 29 we present space-time plots of surrogate intensity fluctuations (i.e.,  $\Delta\rho/\rho_0 = \Delta T/T$ ) and vertical Doppler velocities (i.e.,  $u_z/c_0$ ) as they might appear in the internetwork because of a wave source within the neighboring network element (§ 3.2). Each figure has three panels; two correspond to our reference altitudes of  $z = 499$  and  $993$  km, and the third is an additional low-lying photospheric layer at  $z = 99$  km. The magnetic canopy passes through the highest atmospheric layer, and the remaining two are in the high- $\beta$  region (see Fig. 10). The magnetic field is fairly uniform in the upper two layers. At  $z = 99$  km the field is horizontal in the left  $\frac{2}{3}$  of the panel, but it rapidly switches to vertical over

the right  $\frac{1}{3}$  (because of the underlying reverse-polarity flux concentration).

In intensity fluctuations we are seeing only the high- $\beta$  fast wave, which cares little for the magnetic field orientation. At 99 km there are two fast-wave trains propagating away from the network. The first to arrive is the direct fast wave emitted from the piston. The overplotted solid black lines are tilted to show rectilinear propagation in the  $x$ -direction at the sound speed  $c_0$ . Since the fast wave is quasi-longitudinal, it is basically absent from the corresponding Doppler signal ( $|u_x| \gg |u_z|$ ; see Fig. 29, *left*). The second wave train, outlined by the curving broken lines, is composed of downward-propagating fast waves arriving from the overlying magnetic canopy. They are generated by mode mixing from the impinging low- $\beta$  fast waves. They appear in *both* intensity and Doppler signals since they propagate at an oblique angle with respect to the vertical line of sight (i.e.,  $|u_x| \sim |u_z|$ ). Consequently, their apparent phase velocity is in excess of  $c_0$ . This excess is merely a projection effect, since we know that the high- $\beta$  fast wave propagates at  $c_0$ . The curvature of the second fast-wave train might also be incorrectly interpreted as a gradual slowing of the waves, perhaps due to the decrease of the magnetic field away from the neighboring network. However, from our analysis we know that this is attributed to the curvature of the overlying magnetic canopy imparting slightly different propagation directions to the transmitted fast waves along its length. Finally, the interference between these two wave trains

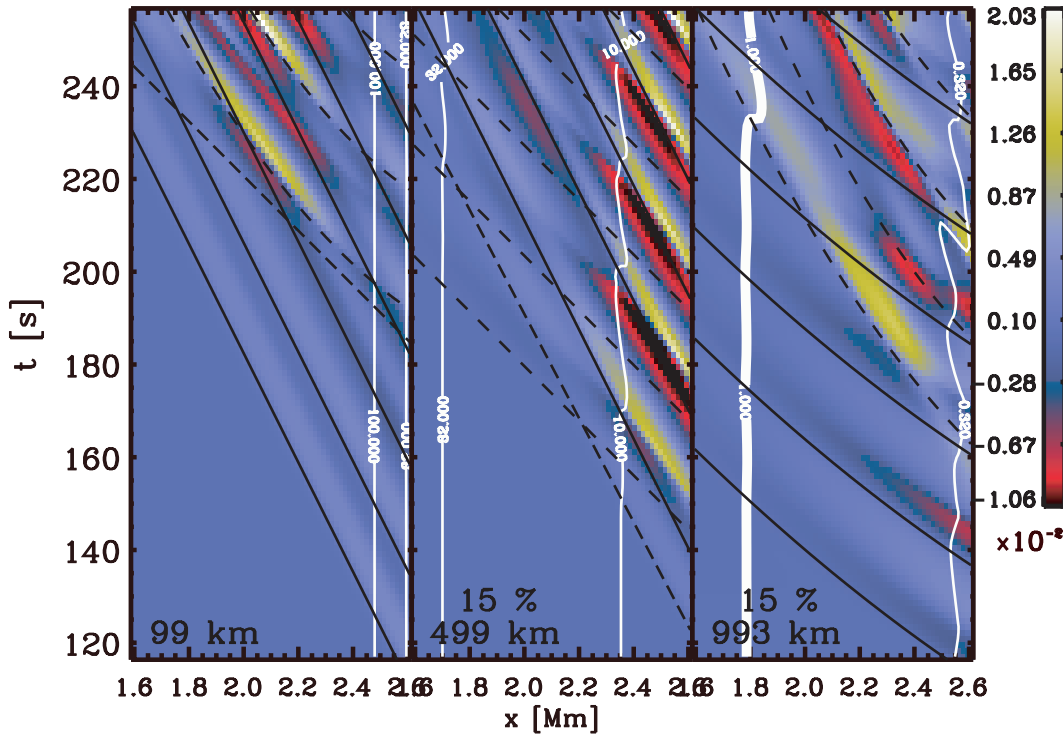


FIG. 28.—Distance vs. time plots of the relative density fluctuations,  $\Delta\rho(x, t)/\rho_0$  recorded at three different atmospheric altitudes  $z = 99$  km (*left*),  $499$  km (*middle*), and  $993$  km (*right*), for *radial* driving in the *weak* magnetic field (§ 3.2). The actual data are imaged in the left, but to employ the same color table it is necessary to multiply the actual fluctuations recorded at the two higher altitudes by 0.15 before the images are formed. The motion of various iso- $\beta$  contours are indicated by the overplotted white lines. Various systems of black lines are employed in the panels to emphasize the different wave trains that coexist within each of the fields of view. Below the canopy (*left and middle*) the straight black lines outline the horizontally propagating fast waves, which come directly from the piston and travel across these images at  $c_0 = 8.49$  km s<sup>-1</sup>. The curving dashed lines delineate the fast waves, which propagate down from the overlying magnetic canopy. As expected they arrive later at 99 km than at 499 km, and their supersonic and variable horizontal phase speeds indicate that they travel at an angle to the vertical. There is no wave activity at these atmospheric locations for times earlier than 115 s.

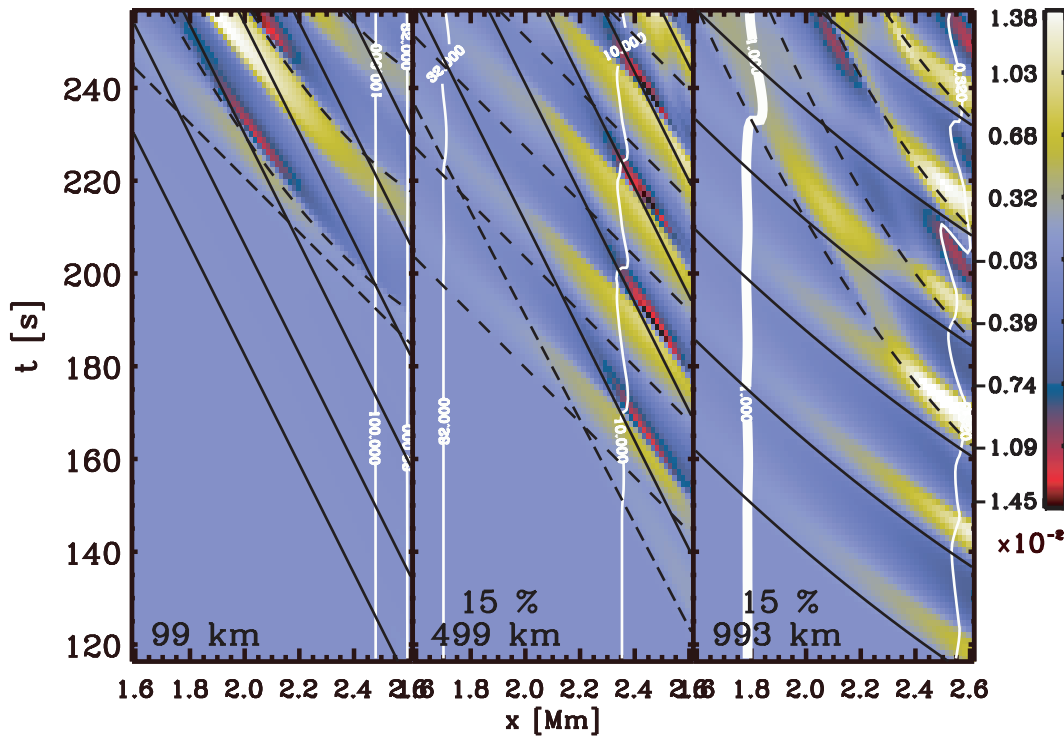


FIG. 29.—Analogous to Fig. 28 in every respect *except* displaying the vertical Mach number,  $u_z(x, t)/c_0$ . The iso- $\beta$  contours and the systems of black guidelines are precisely the same as those employed in Fig. 28, so one may use them to compare and contrast features between these two figures. As noted on the middle and right panels, slightly different scalings are necessary to optimize the single color table. The distinctions between these images and those presented in Fig. 28 are numerous and hardly subtle. Note, for example, how the horizontally propagating direct fast wave is entirely absent in the left panel.

creates additional structures in intensity (but clearly *not* in Doppler!) with their own bewildering array of phase speeds and accelerations. In addition, they have a tendency to begin and end rather abruptly. It is easy to imagine how this could bedevil the unprepared data interpreter.

In the middle atmospheric layer (499 km) the same two wave trains are present, but because this layer is much closer to the magnetic canopy, both appear at roughly the same time. Since we have access to information at all intermediate levels and times, there is no difficulty in drawing a set of guidelines to associate with each of our fast waves. One may well imagine that on the basis of knowledge of *only* Figure 28 (*middle*), several other plausible but ultimately erroneous interpretations could be developed.

Finally, at an altitude of 993 km we are mostly looking above the canopy in the low- $\beta$  atmospheric top layer. The first wave train to arrive is composed of fast waves, which have previously crossed through the magnetic canopy far to the right within the neighboring network element (see Fig. 12). Their apparent horizontal phase speed reflects a combination of their oblique propagation and an intrinsic phase speed in excess of  $c_0$ . The second wave train is identified with low- $\beta$  slow waves, which are also created by mode mixing in which the canopy dips into the neighboring network. These are longitudinal acoustic waves, and they travel along the magnetic field at  $c_0$ ; therefore, their large apparent horizontal phase speed and its variation with  $x$  are both a projection effect. The slow wave is strongest in intensity, but it also registers in the Doppler signal because the magnetic field is nearly vertical at  $z = 993$  km. We can check this by looking at  $u_x$  instead of  $u_z$ , but this is a luxury the observer does not often enjoy.

It is instructive to ask how this picture would change if one's observations were similarly placed with respect to a sunspot or a very intense segment of the network where the magnetic canopy touches the nearby photosphere. We address this question with Figure 30, where we have simply increased the magnetic field strength everywhere by a factor of 4 relative to Figure 29. In other words, we employ our simulation of radial driving in a *strong* magnetic field, while holding all other parameters fixed (§ 3.1). The first obvious difference made by the larger field is that there is no early high- $\beta$  fast wave proceeding directly from the driving piston. The driver is in a low- $\beta$  plasma, and it simply does not generate such an object. The fast wave is created through mode conversion at the intervening magnetic canopy.

The first waves to arrive come from the overlying canopy and propagate down toward the photosphere from above. The high- $\beta$  regions around a very strong flux concentration first experience a “rain” of fast waves descending from the canopy aloft. Disturbances may travel very rapidly in the low- $\beta$  top layer as compared with the low-lying high- $\beta$  region between the piston and the distant observation point. Indeed the farther one moves away from the wave source, the greater is the time delay between the commencement of the “rain” of fast waves from above and the eventual arrival of lateral “ground” or “surface” high- $\beta$  fast waves.

Beginning at 993 km, which is well within the low- $\beta$  plasma, we may readily identify the early arrival of the direct fast waves, and the first steepened slow N-wave front prominent in Figure 30 (*top right*). The teardrop-shaped fast-wave fronts break through the 993 km layer and propagate nearly aligned with the vertical and thus give a very large projected horizontal phase speed. The direct slow



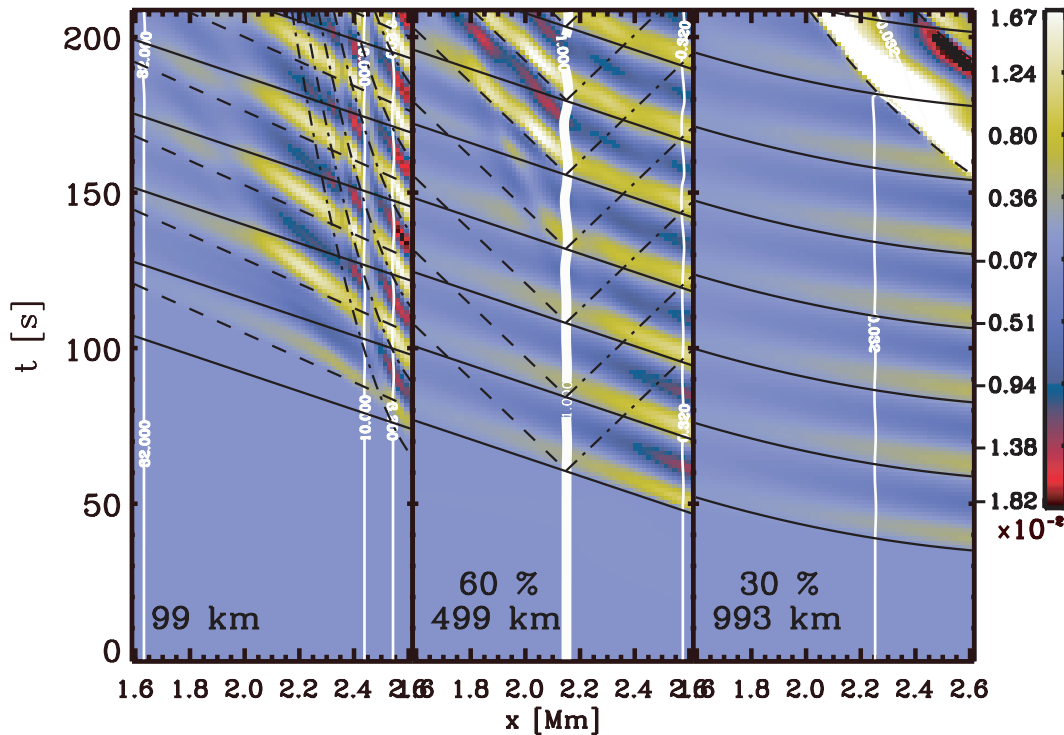


FIG. 30.—Distance vs. time plot of  $u_z(x, t)/c_0$  analogous to Fig. 29 *except* obtained for the numerical simulation of radial driving in the *strong* magnetic field (§ 3.1). The magnetic canopy bisects the central panel. The other two images come from above (*right*) and below (*left*) the canopy. The system of solid black guidelines highlights the low- $\beta$  fast wave to the right of the heavy white line and its high- $\beta$  fast-wave continuation below the canopy. The slight tilt of the wavevector away from the vertical is responsible for the large apparent horizontal phase speed. The system of curved dot-dashed guidelines at the 99 km level draws attention to the high- $\beta$  slow waves. They creep very slowly from right to left as they emerge from the canopy. Additional high- $\beta$  fast waves emitted from the more vertically oriented portion of the canopy are indicated by the system of dashed lines. These fast waves eventually extend up to the 499 km layer and interfere with the other fast waves to produce the modulation for  $t \geq 120$  s in the middle panel.

wave appears because much of the magnetic field passing through this region connects back to the distant piston at the photosphere.

The magnetic canopy passes through the middle of the  $z = 499$  km layer panel. The low- $\beta$  fast waves propagate from right to left through the canopy, with an  $x$ -projected phase speed of approximately  $4c_0$ . The apparently seamless march of the wave train is misleading because it emerges as a high- $\beta$  fast wave with some different physical characteristics. The change is not particularly evident in  $u_z$  except for a modest decrease in amplitude. The dashed black lines emanating from the canopy show trajectories for transmitted and reflected disturbances with a  $1.4c_0$  projected phase speed. Structures with a phase speed of this order eventually emerge from the high- $\beta$  side of the canopy. There is little evidence for an associated reflected wave, however. The explanation for this feature is tied to events at lower altitudes (see below).

At the 99 km photospheric level, the Doppler oscillations are rife with structure and complication. In effect, *three* distinct wave trains are passing through this region simultaneously. The associated interference pattern presents an entirely new level of shifting forms and structures. It is disentangled only by a sustained analysis of much of the extant simulation data. The result of such a painstaking exercise is recorded by the three sets of guidelines overplotted on this panel. The solid lines represent the downward continuation of the (high  $\beta$ ) fast-wave “rain” from the overlying canopy (*middle*). The dashed lines mark the direct “surface” or

“ground” wave that is a (mostly) horizontally traveling high- $\beta$  fast wave. This wave has been emitted from the more vertical portions of the magnetic canopy near  $x = 2.8$  Mm via mode conversion from the legs of the low- $\beta$  fast wave teardrops. The gradual horizontal bending of the canopy with altitude adds some dispersion in wave orientation and phasing, which tends to further confuse the picture. Finally, the highly curved broken lines are the high- $\beta$  slow waves featured in Figures 8–9, generated preferentially where the magnetic field runs parallel to  $\nabla\beta$  along the canopy.<sup>24</sup> They make a large contribution to the Doppler signal because  $u_\perp$  and  $u_z$  are well aligned at this location. The cause of the delayed appearance of the structure on the high- $\beta$  side of the canopy in the middle panel ( $z = 499$  km) is thus related to the upward extensions of the high- $\beta$  slow waves and the fast “ground” waves visible at 99 km.

As a final example we display the intranetwork oscillations directly over the driving piston in Figure 31. By the previous standards, the analysis of this situation is relatively straightforward. The two panels show our proxies for the intensity fluctuations and the line-of-sight Doppler velocity at the 993 km altitude. Recall that the driving piston spans 400 km of the photosphere between  $x = 3.55$  and  $3.95$  Mm. Since the oscillation data derive from the low- $\beta$  top layer, there are two interfering wave trains: fast waves highlighted

<sup>24</sup> In an intensity (or density) display these waves are very much weaker than they appear in Fig. 30.

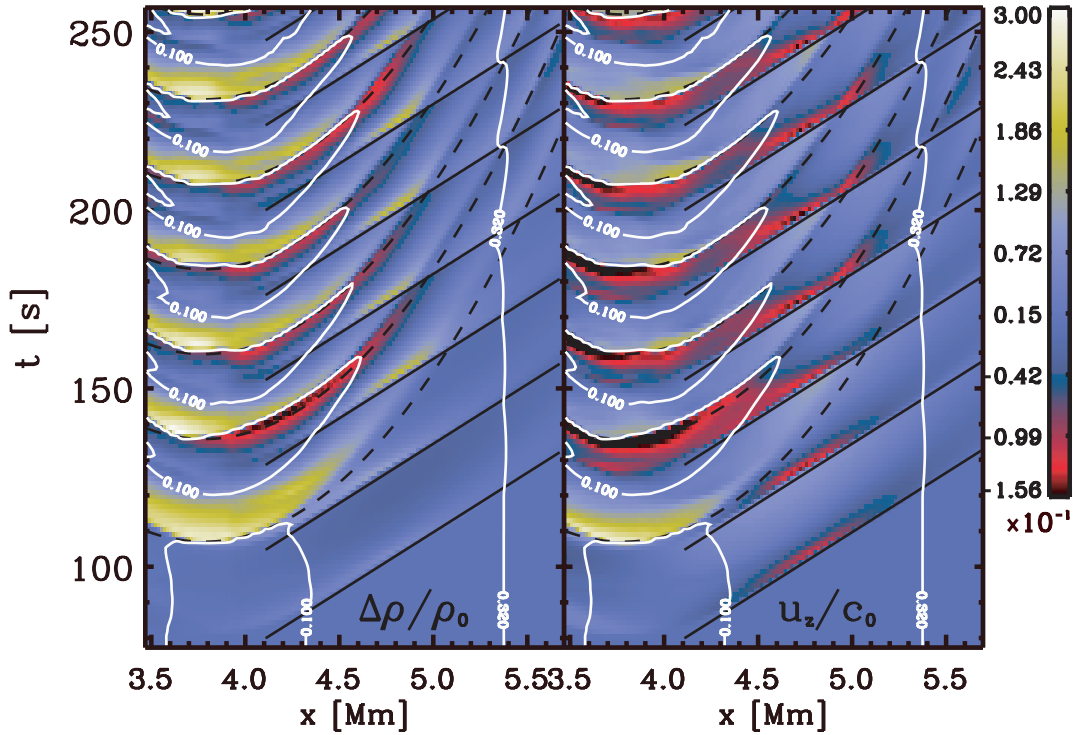


FIG. 31.—Distance vs. time plot of  $\Delta\rho(x, t)/\rho_0$  (left) and  $u_z(x, t)/c_0$  (right) at an altitude of  $z = 993$  km, for radial driving in a weak magnetic field (§ 3.2). The interference of the transmitted fast and slow waves emitted from the underlying canopy (see Figs. 12 and 13) produce distinct kaleidoscopic patterns in intensity (left) and Doppler (right) time series. The fast waves are highlighted by the system of straight solid lines, and the slow waves by the curved broken lines. The curvature is consistent with the apex of the slow-wave front first breaking through the 993 km layer near  $x = 3.8$  Mm, followed by the flanks of the wave front at larger  $x$  and later  $t$ . The guideline systems, like the iso- $\beta$  contours, are identical in each panel.

by the solid black lines and slow waves marked with the broken black curves. They are *both* generated some 400 km below this observation point where the piston-generated high- $\beta$  fast waves interact with the magnetic canopy (see Fig. 12). Because both transmitted wave trains have a common source, they bear fixed phase relationships, which in turn causes them to interfere constructively and destructively as they pass through each other. There are no *physical* interactions between them at these altitudes because the plasma  $\beta$  is small, and their amplitudes are not sufficient to bring nonlinearities into play (Kaburaki & Uchida 1971; Axelsson 2000).

The fast and slow waves contribute differently to  $\Delta\rho$  and  $u_z$ . The “observations” therefore look substantially different in intensity than in Doppler velocity. The gross time-distance behaviors are common to both panels of Figure 31, but a point-by-point comparison of the two time series reveals widespread incongruities in both amplitude and phase. Full knowledge of the simulation permits one to ascribe both the similarities and the differences to the interference of the two wave trains. However, with the limited information present in Figure 31 the puzzle is not as easy to decipher. One might reason that since the observations are taken within the network, where the magnetic field is assumed to be fairly uniform and vertically oriented, there ought to be a good magnetic connection between the photospheric wave source and these higher (chromospheric) layers. A fairly regular sequence of field-guided steepened acoustic disturbances—something similar to that described by Carlsson & Stein (1997) for the  $K_{2V}$  grains—might be anticipated here. Given this premise, the analysis would

then probably turn to explaining why the amplitudes remain small and what gives rise to the abundance of disparate Doppler and intensity small-scale structures.

No doubt some fascinating scenarios would be devised. But we know the basic premise is off the mark. The chromosphere is *not* well connected to the driving piston at the photosphere because the magnetic field lines must all pass through a  $\beta = 1$  magnetic canopy.<sup>25</sup> Below the canopy, the plasma  $\beta$  is large, so the orientation of the magnetic field is largely irrelevant for the fast waves created by the piston. They propagate away from the wave source in all directions and are in no sense collimated by the network field.<sup>26</sup> When these fast waves impinge on the bottom of the magnetic canopy, they are mode-converted into *both* fast and slow waves, which subsequently progress farther into the overlying low- $\beta$  atmosphere. The low- $\beta$  fast waves are also not much influenced by the magnetic field orientation: they accelerate upward through the atmosphere and leave their teardrop legs to move laterally toward the upper segments of the canopy. The low- $\beta$  slow waves *are* guided along the magnetic field, but they are also created over a rather large segment of the canopy, not simply that portion that resides directly above the driving piston. The reason for this widespread

<sup>25</sup> The good magnetic connection between the photospheric driver and the overlying chromosphere would be realized within the strong magnetic field simulations. For these calculations the good connection is effected by the intervening low- $\beta$  plasma *and* the magnetic lines of force. Both are necessary.

<sup>26</sup> The story would be quite different of course if the piston generated *only* the high- $\beta$  slow waves!



slow-wave conversion is the uninhibited lateral expansion of the high- $\beta$  fast wave from the piston location.

## 6. SUMMARY AND OUTLOOK

### 6.1. Theoretical Summary

Through the previous five sections we have pursued a long but we hope enlightening journey through the subject of MAG wave propagation in two nontrivial magneto-atmospheres. The key to understanding lies in identifying the circuitous path of the  $\beta \approx 1$  magnetic canopy layer through the region of interest. The necessary input ingredients are knowledge of the magnetic field, through extrapolation or by direct measurement, and the distribution of pressure and density.

The magnetic canopy partitions the magneto-atmosphere into contiguous volumes of high- $\beta$  and low- $\beta$  plasma. Within these simply connected domains information and energy may be propagated by any one of the MAG waves listed in Table 4. For the two-dimensional simulations studied here the fast and slow waves are effectively *decoupled* from each other within the separate high- and low- $\beta$  domains. All couplings and transformations are restricted to the environs of the magnetic canopy, which also functions as the domain wall. In two dimensions, therefore, one enjoys this very elegant and extremely powerful conceptual advantage of treating each wave variety separately within a contiguous high- or low- $\beta$  area and then working out the couplings and transformations across quasi-one-dimensional magnetic canopy boundaries. It may be remarked that all the analysis presented in §§ 3 and 5 is based on the repeated application of this technique.

Although we have reasonable theoretical facility in propagating the two waves through the domains, what we lack for the present is a robust set of rules that permit us to connect the waves across the magnetic canopy (Carlsson & Stein 1999). In the examples presented here, the numerical simulation has done this for us as a by-product of its direct solution of the primitive equations. We should almost be able to dispense with the numerics, at least in a qualitative context, if we could develop connection formulae to tell us how much transmitted high- $\beta$  slow and fast waves are created when a low- $\beta$  fast wave is incident on the canopy, for example. The mode conversion studied here and in Paper I have provided some hints as to what might be important control parameters, viz., the relative alignment (or lack thereof) between  $\mathbf{B}$ ,  $\nabla\beta$ , and the local wavevector  $\mathbf{k}$ . But we are still far from assembling these pieces into a coherent and predictive picture.

In three spatial dimensions, the (intermediate) Alfvén wave mixes with the fast and slow waves. The prevailing evidence suggests that this coupling is not simply restricted to the  $\beta \approx 1$  domain boundaries. Rather there are numerous calculations of ULF waves in the magneto-atmosphere, for example, which indicate that the fast and the (shear) Alfvén waves remain coupled throughout the entire volume of low- $\beta$  plasma (Singer et al. 1981; Southwood & Hughes 1983; Kivelson & Southwood 1985, 1986; Murata 1986; Inhester 1987; Lee & Lysak 1990; Wright 1992; Cheng et al. 1993; Walker 1998). A comprehensive study of this larger set of MAG wave couplings in the solar and stellar atmospheric context must await a future contribution in this series.

### 6.2. Observational Advice

The examination of the synthetic observations carried out in § 5 leaves the overwhelming impression that a little knowledge is indeed a dangerous thing in the realm of data interpretation. The best advice one can give is to be aware of the regions surrounding the place where the observations are obtained (Gary 2001; McIntosh et al. 2001; McIntosh & Judge 2001). It is imperative to determine whether the spectral line or continuum is formed in a low- or high- $\beta$  plasma. But this alone is not sufficient. One must also be able to infer the close approaches of the magnetic canopy and to know whether the canopy resides above or below the site where the data are from. It is also essential to determine where the magnetic flux passing through the observing layer connects at the photosphere or perhaps even above in the corona.

Next, the location of the wave sources and their dominant state of polarization (radial vs. transverse driving motions) must be ascertained (Musielak & Rosner 1987; Collins 1989a, 1989b, 1992; McKenzie 1991; Lee 1993). The *lateral* proximity of the wave source to the observation point need not be the overriding factor. The magnetic field may divert waves from nearby sources away from the observed region or connect it to distant sites of profuse wave activity. Reliable information on the wanderings of the magnetic canopy is particularly helpful in determining how much or little attention may be required in tracking down distant sources.

Finally, it is paramount to be aware that as many as three waves are moving information and energy through the magneto-atmosphere and that each wave contributes in different ways to the integrated intensity and Doppler signals. The differences are not only related to the structure of the atmosphere and the orientation of the wave trains but also to the perspective of the observer. The different wave varieties often follow distinct routes between their source and a common observation point. This opens the way for a rich magneto-acoustic tomography of the solar atmosphere. The parallels are indeed somewhat closer with the terrestrial seismic discipline (where one employs both  $P$  and  $S$  waves) than for the better developed program of local helioseismology within the solar envelope and interior (where only  $p$ -modes are currently considered).

In the weak-field regions surrounding magnetic flux concentrations we found two wave trains: a coronal “rain” of downward-propagating fast waves and the direct horizontally traveling “surface” or “ground” fast wave. The former arrives before the latter because it takes advantage of the high wave speed in the overlying low- $\beta$  top layer. Within the magnetic flux concentration the fast-wave train arrives before the slow-wave train. There are better opportunities here for separating their contributions to observations because they have rather different phase speeds and wavelengths and they emphasize distinct combinations of dependent variables. The ratio of fast-to-slow wave amplitude depends both on the nature of the source and whether the magnetic field lines that connect back to the source region pass through the magnetic canopy.

We also identified some regions with very complex oscillations. Along the two-dimensional  $\beta = 1$  magnetic canopy one can at each point determine a radius of curvature and thereby construct a circle tangent to the canopy that employs this radius of curvature. Our simulations suggest that the most complex wave fields are found within this tangent circle when (1) it resides within the high- $\beta$  plasma and

(2) it corresponds to a local minimum in the radius of curvature along the magnetic canopy. Under these circumstances, high- $\beta$  fast waves with a wide range of propagation directions are expected in the tangent circle. If the magnetic field is also well aligned with  $\nabla\beta$ , then high- $\beta$  slow waves are also prevalent. The essential point is that a diverse variety of waves pass through these regions.

This observational counsel comes with two caveats. First, it is based on the assumption that the wave source is coherent for many wave periods. This is a critical prerequisite for the complex but stable interference patterns present in our simulations. The fundamental reason is that these interferences are often between slower disturbances created during the initial cycles of the piston, with the faster disturbances generated later in time. Without the phase locking between early and late times, the interference patterns become transitory in space and in time. The coherence time of the source therefore limits the distance to which the stable interference patterns can exist. Second, the interference patterns are also predicated on the various waves being able to survive their circuitous journeys from the source. We know that radiative

transfer is likely to have a profound effect on MHD waves with a strong compressive character (Bogdan et al. 1996). Likewise, there is increasing attention to the role of Hall and Pedersen conductivities in damping Alfvénic disturbances in the upper chromosphere and solar corona (Campos 1998; Campos & Mendes 2000; DePontieu, Martens, & Hudson 2001; Vogt 2002). Many other dissipation mechanisms abound, but none of them are included in our four numerical experiments.

This work was supported by Norwegian Research Council grant 146467/420, Solar and Heliospheric Plasmas, by grant ATM-0139977 from the National Science Foundation (NSF), and by a grant from the National Aeronautics and Space Administration. T. J. B. expresses his sincere thanks for the kind hospitality of Spiro Antiochos and his colleagues at the Naval Research Laboratory and for the strong support and encouragement of Richard Behnke and the Upper Atmospheric Research Section of the NSF. The thoughtful suggestions and counsel of the referee, Zdzisław Musielak, are gratefully acknowledged.

## REFERENCES

- Anile, A. M., Hunter, J. K., Patano, P., & Russo, G. 1993, *Ray Methods for Nonlinear Waves in Fluids and Plasmas* (New York: Wiley)
- Anile, A. M., Mulone, G., & Pluchino, S. 1980, *Wave Motion*, 2, 267
- Axelsson, P. 2000, *Nonlinearity*, 13, 19
- Barnes, A. 1992, *J. Geophys. Res.*, 97, 12,105
- Beliën, A. J. C., Martens, P. C. H., & Keppens, R. 1999, *ApJ*, 526, 478
- Beliën, A. J. C., Poedts, S., & Goedbloed, J. P. 1997, *A&A*, 322, 995
- Blackstock, D. T. 1962, *J. Acoustic Soc. Am.*, 34, 9
- . 1965, *J. Acoustic Soc. Am.*, 39, 1019
- Bo, L., & Wang, S. 2001, *Chinese Astron. Astrophys.*, 25, 194
- Bodo, G., Kalkofen, W., Massaglia, S., & Rossi, P. 2000, *A&A*, 354, 296
- Bogdan, T. J., Knölker, M., MacGregor, K. B., & Kim, E.-J. 1996, *ApJ*, 456, 879
- Bogdan, T. J., et al. 2002, *Astron. Nachr.*, 323, 196
- Bois, P. A. 1976, *J. Mec.*, 15, 781
- Borovikov, V. A. 1996, *J. Appl. Math. Mech.*, 60, 521
- Bray, R. J., & Loughhead, R. E. 1974, *The Solar Chromosphere* (London: Chapman and Hall), 252
- Čadež, V. M., & Ballester, J. M. 1994, *A&A*, 292, 669
- Čadež, V. M., Oliver, R., & Ballester, J. M. 1996, *A&A*, 307, 947
- Campos, L. M. B. C. 1998, *Theoret. Comput. Fluid Dyn.*, 10, 37
- Campos, L. M. B. C., & Mendes, P. M. V. M. 2000, *J. Plasma Phys.*, 63, 221
- Cannon, C. J. 1974, *J. Quant. Spectrosc. Radiat. Transfer*, 14, 761
- Cargill, P. J., Spicer, D. S., & Zalesak, S. T. 1997, *ApJ*, 488, 854
- Carlsson, M., & Stein, R. F. 1992, *ApJ*, 397, L59
- . 1995, *ApJ*, 440, L29
- . 1997, *ApJ*, 481, 500
- . 1999, in *ASP Conf. Ser. 184, Third Advances in Solar Europyphysics Conference: Magnetic Fields and Oscillations*, ed. B. Schmieder, A. Hofmann, & J. Staude (San Francisco: ASP), 206
- . 2002, *ApJ*, 572, 626
- Cheng, C. Z., Chang, T. C., Lin, C. A., & Tsai, W. H. 1993, *J. Geophys. Res.*, 98, 11,339
- Cole, J. D., & Greifinger, C. 1969, *J. Geophys. Res.*, 75, 193
- Collins, W. 1989a, *ApJ*, 337, 548
- . 1989b, *ApJ*, 343, 499
- . 1992, *ApJ*, 384, 319
- Courant, R., & Friedrichs, K. O. 1948, *Supersonic Flow and Shock Waves* (New York: Wiley)
- Crighton, D. G., & Lee-Bapty, I. P. 1992, *Wave Motion*, 15, 315
- DePontieu, B., Martens, P. C. H., & Hudson, H. S. 2001, *ApJ*, 558, 859
- Earnshaw, S. 1860, *Philos. Trans. R. Soc. London*, 150, 133
- Einaudi, F. 1969, *Phys. Fluids*, 12, 752
- . 1970, *J. Geophys. Res.*, 75, 193
- Fay, R. D. 1931, *J. Acoustic Soc. Am.*, 3, 222
- Ferraro, V. C. A., & Plumpton, C. 1958, *ApJ*, 129, 459
- Flå, T., Habbal, S. R., Holzer, T. E., & Leer, E. 1984, *ApJ*, 280, 382
- Gail, H.-P., Cuntz, M., & Ulmschneider, P. 1990, *A&A*, 234, 359
- Gary, G. A. 2001, *Sol. Phys.*, 203, 71
- Hammerton, P. W., & Crighton, D. G. 1989, *Proc. R. Soc. London A*, 426, 125
- Inhester, B. 1987, *J. Geophys. Res.*, 92, 4751
- Kaburaki, O., & Uchida, Y. 1971, *PASJ*, 23, 405
- Kato, S. 1966, *ApJ*, 144, 326
- Kivelson, M. G., & Southwood, D. J. 1985, *Geophys. Res. Lett.*, 12, 49
- . 1986, *J. Geophys. Res.*, 91, 4345
- Klein, R. I., Stein, R. F., & Kalkofen, W. 1978, *ApJ*, 220, 1024
- Kudoh, T., & Shibata, K. 1999, *ApJ*, 514, 493
- Lamb, H. 1908, *Proc. London Math. Soc.*, 7, 122
- . 1910, *Proc. R. Soc. London A*, 84, 551
- Lee, D.-H., & Lysak, R. L. 1990, *Geophys. Res. Lett.*, 17, 53
- Lee, J. W. 1993, *ApJ*, 404, 372
- Leibacher, J., Gouttebroze, P., & Stein, R. F. 1982, *ApJ*, 258, 393
- Leroy, B. 1985, *Geophys. Appl. Fluid Dyn.*, 32, 123
- Leroy, B., & Schwartz, S. J. 1982, *A&A*, 112, 84
- Litwin, C., & Rosner, R. 1998, *ApJ*, 506, L143
- Mariska, J. T., & Hollweg, J. V. 1985, *ApJ*, 296, 746
- McIntosh, S. W., & Judge, P. G. 2001, *ApJ*, 561, 420
- McIntosh, S. W., et al. 2001, *ApJ*, 548, L237
- McKenzie, J. F. 1991, *J. Geophys. Res.*, 96, 9491
- Murata, H. 1986, *J. Plasma Phys.*, 36, 243
- Musielak, Z. E., & Rosner, R. 1987, *ApJ*, 315, 371
- Nakariakov, V. M., Verwichte, E., Berghmans, D., & Robbrecht, E. 2000, *A&A*, 362, 1151
- Naugol'nykh, K. A. 1971, in *High-Intensity Ultrasonic Fields*, ed. L. D. Rozenberg (New York: Plenum), 5
- Odstrčil, D., & Karlický, M. 2000, *A&A*, 359, 766
- Ofman, L., & Davila, J. M. 1998, *J. Geophys. Res.*, 103, 23,677
- Ofman, L., Nakariakov, V. M., & DeForest, C. E. 1999, *ApJ*, 514, 441
- Ofman, L., Nakariakov, V. M., & Sehgal, N. 2000, *ApJ*, 533, 1071
- Ofman, L., & Thompson, B. J. 2002, *ApJ*, 574, 440
- Oliver, R., & Ballester, J. L. 1995, *ApJ*, 448, 444
- . 2002, *Sol. Phys.*, 206, 45
- Pelinovskii, E. N., & Petrukhin, N. S. 1988, *Soviet Astron.*, 32, 457
- . 1994, *Geophys. Astrophys. Fluid Dyn.*, 75, 77
- Rankine, W. J. M. 1870, *Philos. Trans. R. Soc. London*, 160, 277
- Rayleigh, L. 1910, *Proc. R. Soc. London A*, 84, 247
- Rosenthal, C. S., et al. 2002, *ApJ*, 564, 508 (Paper I)
- Ruderman, M. S., Nakariakov, V. M., & Roberts, B. 1998, *A&A*, 338, 1118
- Saito, T., Kudoh, T., & Shibata, K. 2001, *ApJ*, 554, 1151
- Sakai, J.-I., Igarashi, J., & Kawata, T. 1998, *Sol. Phys.*, 181, 13
- Sakai, J. I., Mizuhata, Y., Kawata, T., & Cramer, N. F. 2000, *ApJ*, 544, 1108
- . 2001, *ApJ*, 550, 1075
- Schmitz, F., & Fleck, B. 1995, *A&A*, 301, 483
- Schwartz, R. A., & Stein, R. F. 1975, *ApJ*, 200, 499
- Shibata, K. 1983, *PASJ*, 35, 263
- Singer, H. J., Southwood, D. J., Walker, R. J., & Kivelson, M. G. 1981, *J. Geophys. Res.*, 86, 4589
- Southwood, D. J., & Hughes, W. J. 1983, *Space Sci. Rev.*, 35, 301
- Stein, R. F. 1968, *ApJ*, 154, 297
- Stein, R. F., & Schwartz, R. A. 1972, *ApJ*, 177, 807
- . 1973, *ApJ*, 186, 1083
- Sterling, A. C., & Hollweg, J. V. 1988, *ApJ*, 327, 950
- Sutmann, G., Musielak, Z. E., & Ulmschneider, P. 1998, *A&A*, 340, 556
- Terradas, J., Oliver, R., & Ballester, J. L. 1999, *ApJ*, 517, 488
- Theurer, J., Ulmschneider, P., & Cuntz, M. 1997, *A&A*, 324, 587
- Tsiklauri, D., & Nakariakov, V. M. 2001, *A&A*, 379, 1106
- Vogt, J. 2002, *Surv. Geophys.*, 23, 335

- Wait, J. R. 1974, *J. Geophys. Res.*, 79, 5055
- Walker, A. D. M. 1998, *J. Atmos. Sol.-Terr. Phys.*, 60, 1279
- Webb, G. M., Woodward, T. I., Brio, M., & Zank, G. P. 1993, *J. Plasma Phys.*, 49, 465
- Westervelt, P. J. 1950, *J. Acoustic Soc. Am.*, 22, 319
- Whitham, G. B. 1974, *Linear and Nonlinear Waves* (New York: Wiley)
- Wright, A. N. 1992, *J. Geophys. Res.*, 97, 6429
- Wu, S. T., Zheng, H., Wang, S., Thompson, B. J., Plunkett, S. P., Zhao, X. P., & Dryer, M. 2001, *J. Geophys. Res.*, 106, 25,089
- Yih, C.-S. 1974, *Phys. Fluids*, 17, 1489